Sensing metal ions-peptide and protein interfacial interactions

Inauguraldissertation

zur
Erlangung der Würde eines Doktors der Philosophie
vorgelegt der
Philosophisch-Naturwissenschaftlichen Fakultät
der Universität Basel

von

Olena Synhaivska

Basel, 2022

Genehmigt von der Philosophisch-Naturwissenschaftlichen Fakultät
auf Antrag von
Prof. Dr. Michel Calame
Prof. Dr. Christian Schönenberger
Prof. Dr. Jan Linnros

Basel, den 19. Oktober 2021

Prof. Dr. Marcel Mayor
Dekan

Contents

1 Introduction

Misfolded protein aggregates have been associated with several major neurodegenerative diseases such as Alzheimer's and Parkinson's[1]. For example, alpha-synuclein (αSyn) is a protein that plays a key role in the parthenogenesis of Parkinson's disease[2]; aggregation of amyloid beta causes Alzheimer's disease[3]; aggregation of tau proteins causes another entire group of disorders, called tauopathies[4]. At certain conditions these proteins tend to aggregate, forming toxic oligomers or amyloid filaments. Studies show that some metal ions facilitate protein aggregation[5].These processes are intensively investigated, but not yet well understood.

Although the presence of metal ions in the human brain is crucial for maintaining normal physiological functions, the imbalance of metal ions such as copper, manganese, iron, zinc, and calcium facilitates the aggregation processes[6,7]. Such imbalance of metal ions can be caused by environmental conditions, such as high industrial metal release. It has been confirmed that prolonged exposure to copper, lead, and manganese leads to higher Parkinson's disease incidence for miners, who were constantly working with these metals[8]. In addition, recent high-resolution scanning transmission x-ray microscopy data showed the presence of copper and iron in human amyloid plaques, confirming the importance of further studying the impact of metal ions on the aggregation processes at the molecular level[9]. Studying the effects of metal ions can help understand the aggregation processes better and facilitate the development of a treatment for Parkinson's disease.

In small quantities, copper (1 mg/kg), manganese (0.17 mg/kg), and zinc (28.6–42.8 mg/kg), are important for our health[10]. However, at certain concentrations they are harmful to humans due to their ability to form complexes with peptides containing nitrogen, sulfur, and oxygen, that can lead to modification of the molecular structure of proteins and therefore cause toxicological and carcinogenic effects, affecting the central nervous system, kidneys and liver, skin, bones, and teeth[11,12]. Based on scientific research, World Health Organization (WHO) and Environmental Protection Agency (EPA) defined guidelines for the acceptable amount of transition metals in drinking water (such as 1.3 mg/l for copper, 5 mg/l for zinc, 0.3 mg/l for manganese). Unfortunately, their levels often exceed the allowed limit[12,13].

Therefore, it is important to monitor the concentration of heavy metals to prevent their negative impact on health, and monitoring systems, as well as rapid, cheap, and easy-to-use tests to quantify heavy metals, are in high demand[14,15].

In this PhD thesis, I focused on the detection of copper and zinc ions using potentiometric methods. Copper is an essential element for human health and is necessary for normal iron metabolism and formation of red blood cells[16,17]. However, elevated concentrations, as well copper deficiency[18], can lead to various diseases like Alzheimer's, Parkinson's, Menkes syndrome, myeloid leucosis, liver cirrhosis, and many others[19,20]. Zinc is also an essential element for the human body[21]. It participates in all major biochemical pathways, and more than 100 enzymes require zinc for their catalytic function[22]. In addition, a lower serum concentration of Zn^{2+} and a higher ratio of Cu^{2+} to Zn^{2+} in patients with multiple sclerosis (MS) suggest the relationship between MS and the concentration of these ions[23].

Therefore, a precise technique for monitoring the transition metal concentration is required. Studying peptides as receptor molecules for sensing can also provide a better understanding of the peptide-ion interaction, helping to shed light on the more complex protein-ion interaction in the human brain.

The classical methods, widely used in clinical laboratories, are atomic absorption spectroscopy[24,25], inductively coupled plasma mass-spectrometry[26], atomic emission spectroscopy (AES) and photometric kinetic methods. Analytical methods, like a flame or electrothermal atomic absorption spectrophotometry, have been adopted as a standard by the International Federation of Clinical Chemistry and Laboratory Medicine (IFCC), the Institute of Clinical and Laboratory Standards (CLSI), and the International Committee for Standardization and Hematology (ICSH)[19]. These methods are accurate, but they are also expensive, not portable, require complicated sample pre-treatment, and are time-consuming.

We propose a sensing approach to detect metal ions in solution, based on detection of their charge upon reacting with the surface of the sensor device, functionalized with an assembled monolayer of the receptor molecules. We use two types of devices: silicon nanoribbon (SiNR) based ion-sensitive field-effect transistor device and extended gate-like device, with thermally evpaorated gold (20 nm thick) sensing surfaces in both cases. Having gold as a sensing surface allows direct one-step assembly of receptor molecules that have a thiol group[27]. Our potentiometric devices have a great potential for sensing purposes compared to state of the art: besides their sensitivity to various targets, achieved with receptor molecules, they can be fabricated at a small size in a CMOS compatible process. This will set a low production cost since hundreds of devices can be produced simultaneously on one substrate.

We studied specific target detection with a focus on understanding reactions at the surface-analyte interface. Ideally, we need a sensor that can detect multiple species, as water or blood samples normally contain more than one

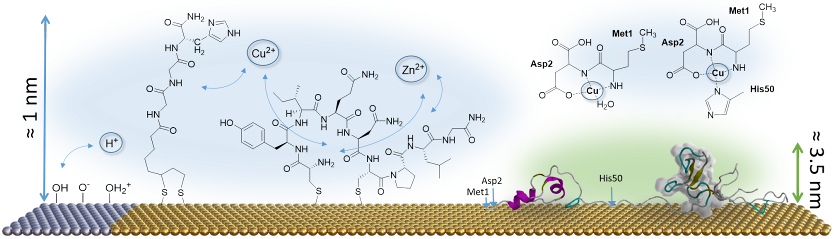

Figure 1.1 Schematic of the surface with (from left to right) hydroxyl groups on Al_2O_3/HfO_2 oxide surface (**Chapter 2**); GGH peptide for Cu^{2+} ion detection (**Chapter 4**); OT for detection of Cu^{2+} and Zn^{2+} (**Chapter 5**); αSyn (monomer) adsorbed on the gold surface (**Chapter 6**).

target which needs to be detected. A device, which combines multiple ISFETs (or even arrays of ISFETs) on one platform, has a high potential for multiplexed sensing. Functionalization of the gate surface with different receptor molecules for various analytes would allow detecting several target species within the same volume simultaneously. The important reason, which prevents the development of such a device, is a combination of complex receptor-target chelation mechanisms and non-specific interactions, affected by measurement conditions. Optimization of measurement parameters is required to obtain meaningful results. Moreover, different receptor molecules may require different measurement conditions, which makes combining them on one platform more challenging.

Currently, the implementation of ISFET devices even for one target has not been commercialized, except for the detection of protons (pH sensing) [28,29]. In this case, a receptor is not needed, and the sensing layer is a gate oxide itself, due to the presence of hydroxyl groups on its surface, as schematically shown in figure 1.1. As I will discuss later in this thesis, measurement conditions are very important and can significantly affect the measured signal. Receptors are often large molecules and they show a complex chelation mechanism with the target.

We discuss in detail, how even in the case of short peptide Glycyl-Glycyl-Histidine (GGH), which we use for detection of copper ions, multiple effects, such as competing reactions, take place. We believe that understanding processes that are happening at the surface, such as specific receptor-target interaction as well as possible non-specific interactions between target species and the surface, is essential for successful determining of device's response and creating a reliable sensor. Then we extend this potentiometric measurement approach to a more complex receptor, neuropeptide Oxytocin (OT), which is selective to both, Cu^{2+} and Zn^{2+} ions. To evaluate the impact of Cu^{2+} ions on the αSyn aggregation pathway, we performed a complex study, combining Raman spectroscopy, atomic force microscopy, and molecular dynamic (MD) simulations.

Chapter 2 provides an overview of basic concepts behind the potentiometric sensing, the description of the devices used in this work, and describes how these basic concepts can be extended to specific ion detection and the application of peptides GGH and OT as receptors discussed. We also introduce the site-binding model, which was established for the quantification of the sensor's response to the pH of the measured electrolyte. In **Chapter 3** we extend this approach to modeling the response of a surface, functionalized with a receptor, to the ionic analyte. We consider multiple cases, for the receptor that is selective to one ion only and the receptor that can bind two ions.

In **Chapter 4** we present the experimental data on the response of GGH peptide to Cu^{2+} ions. We systematically study the impact of pH and composition of the electrolyte, and the concentration range of Cu^{2+}, on the obtained response, and we determine the optimal conditions.

Next, in **Chapter 5**, we study the binding of two ions, Cu^{2+} and Zn^{2+}, to the peptide OT. We systematically design the experiments to evaluate the response to one ion first. Then we measure the response to the mixture of both ions at different concentration ratios, as well as response to one ion in the presence of a high concentration of the other one. At the end of the chapter, we assess the possibility to suppress high background response by passivating the surface.

In addition, in both, **Chapter 4** and **5**, we compare the models described in **Chapter 3** with the experimental data.

Chapter 6 provides the background on the aggregation of αSyn and the effect of metal ions. Then we provide AFM, Raman data and MD simulations on monitoring the aggregation pathway of αSyn.

2 Potentiometric measurement techniques

Potentiometric sensors have a great potential to become new widely used detection devices. They offer sensitivity to different kinds of analytes, design flexibility, the opportunity to use various materials for the fabrication that results in large-scale integration of small-scale devices, enabling lab-on-chip systems that can be used for various purposes. This chapter gives an overview of potentiometric sensing, its basic concepts, and its limitations. We also discuss devices which we use for our measurements, measurement procedures, and the receptor molecules.

2.1 Theoretical background

2.1.1 Detection of ionic analytes

Detection of transition metal ions in various media such as drinking water and blood is very important due to their impact on the human body. Besides established ion detection methods, such as atomic absorption spectroscopy, inductively coupled plasma mass-spectrometry and atomic emission spectroscopy, many different alternative techniques are in development. Most common ones rely on electrochemical and optical methods, combined with various nanomaterials, nanoparticles[30], carbon nanotubes (CNT)[31], novel materials like metal-organic frameworks (MOF)[32], mesoporous organosilicas[33], biomolecules (ligands, proteins, DNA)[34], cells[35] etc. Electrochemical detection includes anodic[36,37] and cathodic[38] stripping voltammetry, cyclic voltammetry[39]. Novel optical methods are based on fluorescence[33], colorimetric detection[40], surface plasmon resonance (SPR)[41]. Photonic biosensors, based on subwavelength waveguides, are also used for label-free molecule detection[42].

Conversely, some unconventional methods such as multiwall CNTs with screen-printed electrodes[31] include modification of electrodes with mercury, which is harmful to human health and the environment. Most of the methods with nanobiomodified electrodes and substrates are promising, but they have problems with the reproducibility of results. Those which use chemical reactions are irreversible[43], and still require complicated equipment – for example, Cu^{2+} ion detection realized with DNAzyme (complicated preparation of sensor material, including expensive equipment for high-performance liquid chromatography (HPLC)[44]. The challenge in sensor development is the reliable conversion of biochemical reactions into a measurable signal that can give quantitative information about the analyte of interest. Optical methods require labeling of the target analyte. These methods[45] can be used for the detection of molecules, but are not helpful for ion detection, as ions cannot be labeled. Therefore there is a need to develop a label-free, selective and reliable sensing technique. For practical use, the device should be portable and easy to operate. When selecting a detection method, another important advantage is the possibility of fabrication up-scaling, which will speed up manufacturing and lower the production cost.

In our project, we focus on the electrical detection methods, which are based on electrodes and therefore can be miniaturized as well as integrated into lab-on-chip devices. They also offer the advantage of label-free sensing. In addition, when combined with selective receptors such sensors can be used for the detection of ionic or biological analytes. In this case, the charge of the receptor-analyte complex should differ from the charge of a receptor.

Schematically, the sensing surface is shown in the figure 2.1. The analyte of interest is dissolved in electrolyte medium solution, a layer of receptor molecules is immobilized on the surface of the sensing device. The receptor should selectively bind the analyte of interest, ideally with high specificity. The immobilization step is also very important in sensor development. The receptor layer is an interface between the transducer and analyte of interest, therefore it can significantly impact the performance of the device. Correct immobilization techniques can significantly improve the outcome.

Immobilization of receptors can be done in different ways. One option is direct adsorption of receptors on the surface. This is a simple method, but not reliable because desorption can take place, as bonding is weak and susceptible to changes of pH, as well as ionic strength and temperature. Another method is encapsulation when biomaterial is placed behind the membrane, which permeable only to some materials. In the case of entrapment technique, molecules are not directly attached to the sensor surface but trapped in polymer film[46]. The obtained layer is stable, however, the activity of the molecule can be limited, as well as diffusion of the analyte to the biodetector. Covalent attachment or chemisorption methods provide a strong and stable binding of the molecule to the surface. The main advantage of this method is that no reverse reaction takes place due to changes in pH, ionic strength and substrate[47]. In our sensors, we use the covalent attachment method, in particular $Au-S$ bond. We discuss it in more detail in Section 2.4.

Another important component of the sensor is a transducer. Biochemical reactions, which take place at the surface, can be converted into a measurable signal using different fundamental transduction principles: mechanical (change in the surface stress), electrical (change in conductivity, current or potential), piezoelectric (change in vibration frequency due to additional mass

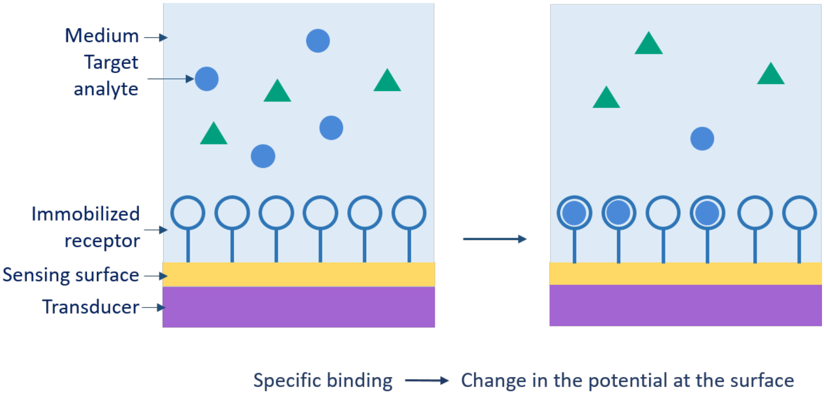

Figure 2.1 Sensing principle: schematic of specific binding of a target analyte to the receptor molecule leads to the change in the potential at the surface, which can be converted into an electric signal.

adsorbed on the surface of the device), calorimetric (measuring heat, produced or absorbed during the reaction), optical (change in absorption, fluorescence, luminescence, internal reflection spectroscopy). Further, we will focus on electrical transduction.

Electrical sensing techniques can be divided into three categories: conductometric, amperometric, and potentiometric[48]. In the case of conductometric transduction, a current is measured through the molecule or the device upon binding of the analyte. Amperometry involves the measurement of a current while applying constant reducing or oxidating potential. Amperometric measurements can be used for various purposes: amperometric titrations are used for the analysis of different substances, ranging from water to radioactive materials; dissolved oxygen probe and amperometric biosensors are used for clinical, environmental, and industrial monitoring; also in high-performance liquid chromatography and inflow injection analysis[49]. Potentiometry is based on the measurement of charge at the sensor surface, which is correlated with analyte concentration. This method has an advantage, as it does not require a generation of oxidation or reduction current, compared to amperometric detection[50]. Examples of potentiometric sensing include pH sensors, which can also be realized with ISFETs based devices.

2.1.2 Ion-sensitive field-effect transistor

The concept of ion-sensitive field-effect transistor (ISFET) was proposed in 1970 by Dutch scientist Piet Bergveld. He suggested replacing metal gate, like in metal-oxide-semiconductor field-effect transistor (MOSFET), widely used at that time, by electrolyte solution with immersed external reference electrode[51]. He adapted Nernst's theory to his device, to be able to predict the response value and showed pH detection. The idea of such a device was criticized at the beginning, due to the direct contact of a liquid and electronic component. However, eventually it gained the attention of researchers from different fields, such as physics, chemistry, biology, and medicine. Since then, ISFETs have been intensively investigated, due to their high potential for specific ion detection, detection of various biomolecules, and other biochemical applications.

Different designs of ISFET-based sensors exist, in combination with various materials for insulating layer (Al_2O_3, HfO_2, SiO_2, TaO_5, TiO_2 etc.) and a sensing surface (surface of insulating oxides, gold, graphene, carbon nanotubes etc.)[52–54]. In terms of geometry, down-scaling to one-dimensional FET was achieved[55], used for gas sensing.

Besides pH sensing, ion detection with ISFETs has been successfully demonstrated, using ion-selective molecules, such as crown ethers[56], detection of FimH protein[57] etc. ISFET-based devices are also promising for variety of applications, including DNA sequencing[58], detection of novel SARS-Cov-2[59] as well as other viruses, bacteria, proteins[60] and biomarkers of various diseases[52,61–63]. However, up to now, only the application of ISFET as a pH sensor was commercialized. Despite excellent reported research results, the sensors are still not robust enough to be widely used. The devices lack reproducibility, as measurement results strongly depend on the conditions such as pH and composition of the measured solution and these processes are not well understood. In addition, the receptors need to be reliably recovered to the pre-complexation state to have a reusable sensor, which is rarely investigated and remains challenging.

Extended gate

ISFETs offer the advantage of having sensing surfaces directly in contact with the transducer. This makes the device compact and free of additional connections, which can lead to higher noise. However, having the sensing surface separated can also be useful for certain applications. So-called extended-gate ion-sensitive field-effect transistor (EGFET) after being introduced by J.van der Spiegel[64], has been widely investigated[65,65,66]. Such device normally consists of a MOSFET as a transducer, with an external sensing surface, connected to the gate. In our project, we modified this concept by using an operational

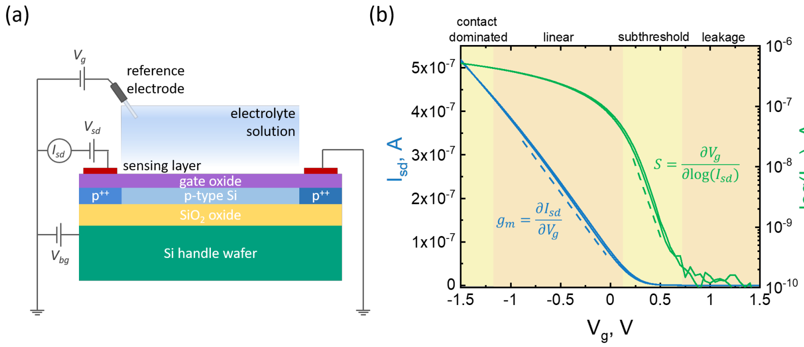

Figure 2.2 (a) Schematic of an ISFET; (b) transfer curves of p-type ISFET: source-drain current (I_{sd}, blue and $log(I_{sd})$, green) versus gate voltage (V_g), applied with the reference electrode. Four operation regimes, contact dominated, linear, subthreshold, and leakage, are shown with different backgrounds.

amplifier-based circuit instead of a single MOSFET and a built-in reference electrode system. We discuss this concept in detail in the section 2.3.2

2.1.3 Working principle of ISFET

ISFET has three terminals: source, drain, and gate. Constant voltage is applied between source and drain (V_{sd}). Source-drain current (I_{sd}) is controlled by the gate voltage (V_g), applied with the reference electrode. Schematic of the ISFET is shown on the figure 2.2a. Using silicon-on-insulator (SOI) wafers is very common in manufacturing. SOI wafer consists of three layers: top Si layer, insulating SiO_2 oxide, and thick handle Si layer. Such wafers can be made with required parameters, such as crystal orientation, conductivity type, thickness, and resistivity for each layer. It is also compatible with the CMOS process. The top layer of silicon will be the main part of the transistor, separated with thick oxide (SiO_2) from the Si handle wafer and with deposited gate oxide on top, as an insulating layer from a liquid gate. Source and drain are highly p-doped, to ensure ohmic contact with the Si channel (the NR itself) and therefore low contact resistance. Additionally, high doping suppresses the inversion regime of the transistor. ISFETs used in this work are operated in an accumulation regime when charge carriers are the holes in Si channel.

Current starts to flow through the channel below a certain gate voltage, called threshold voltage (V_{th}). As we discuss later in the measurement section, we approximate V_{th} at 20 nS conductance value. Source-drain current, normalized by source-drain voltage, yields a conductance value: $G = I_{sd}/V_{sd}$. In this work, if not stated differently, we used $V_{sd} = 100mV$. Transfer curves, I_{sd} and $log(I_{sd})$ versus V_g are shown on the figure 2.2b. With the decrease of gate voltage, holes accumulate in the channel, and current increases, until saturation occurs. Part of the transfer curve, when I_{sd} changes linearly with a change of V_g, is called the linear regime of the transistor. In this region, a transconductance, defined as $g_m = \partial I_{sd}/\partial V_g$ is constant. Below the V_{th}, a small source-drain current exists due to thermal activation of charge carriers. It depends exponentially on V_g. Subthreshold swing S, the inverse of the subthreshold slope, shows how much gate voltage needs to be changed to increase I_sd by order of magnitude. Is it an important parameter of an ISFET, as the steeper the slope is, the faster transistor can be switched, but it is theoretically limited to 59.2 mV/dec at room temperature[67].

For sensing purposes, ISFET can be used in the following way: when source-drain voltage and gate voltage are constant, the change in the measured current will be induced due to the change of the surface state - for example, a different number of surface hydroxyl groups will be protonated or deprotonated, leading to the more positive or more negative surface net charge, as in the case of pH sensing.

2.1.4 pH sensing

pH is an important characteristic of aqueous solutions. It shows how acidic or basic the solution is, by measuring the relative amount of free hydrogen and hydroxyl ions[68].

By design, insulating oxide layer between the silicon channel (in our case, silicon nanoribbon) and the liquid gate is essential for ISFET. In addition, the presence of hydroxyl groups on the oxide surface allows direct application of ISFET as a pH sensor.

Figure 2.3 shows an example of measured data. Transfer curves of an ISFET are recorded when buffer solutions of pH 3, 7, and 10 are at the gate. With an increase of pH value, curves shift to the right, due to additional contribution to the gate voltage from differently charged surface groups. From transfer curves threshold voltage is extracted at constant current value and plotted against pH.

The slope of a linear fit gives the response value. Theoretically, maximum pH response is 59.2 mV/dec[67]. The theoretical basis for such application is given by the site-binding model. To give background for the model, we first describe the surface-electrolyte interface.

Surface-electrolyte interface

In aqueous solutions ions are surrounded by water molecules. Water is a polar solvent and can break up strong ionic bonds, leading to dissolved compounds

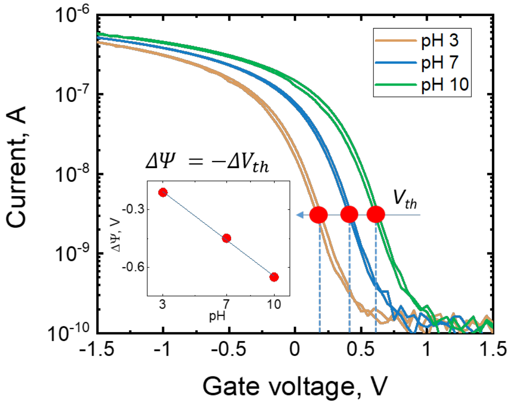

Figure 2.3 Measured transfer curves of the ISFET at pH 3, 7, and 10. Inset shows the extracted values of threshold voltage, converted to the surface potential, versus pH value.

being more chemically active. Aggregated water molecules around an ion locally change the dielectric constant and make it less affected by electric fields from other ions. Therefore, ions can freely move in the solution[69].

When the electrode surface is in contact with the electrolyte, an electrical double layer is formed at the interface, as charges accumulate at the surface. This occurs due to the differences in the chemical potentials between the electrode and electrolyte. Since charges that accumulate from the electrolyte are large-radius ionic charges, one layer of them will not be enough to compensate for the excess charges on the electrode. Therefore a diffuse layer of ionic charges is formed. This layer is called the Guoy-Chapman layer or electrical double layer and the potential drop can be described with Poisson-Boltzmann equation[70].

This model, however, does not include the fact that ions cannot approach the surface closer than their ionic radius. This modification to the model was added by Stern. The region that is close to the electrode surface is depleted from ionic charges, which leads to higher capacitance. This capacitance is known as Stern capacitance. The minimum distance, at which ions can come close to the surface, is called the outer Helmholz plane (OHP)[71]. The diffuse layer starts after OHP.

Double layer capacitance consists of Stern and diffuse layer capacitance in

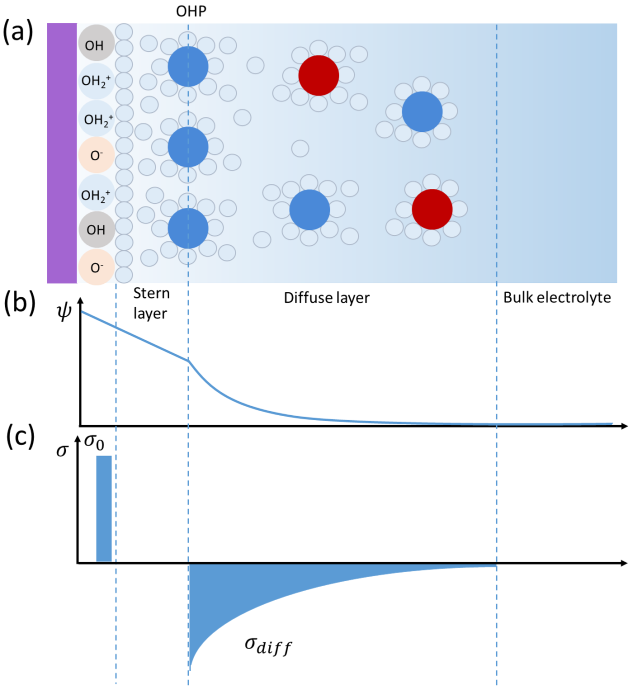

Figure 2.4 (a) Schematic of the double layer according to the Gouy-Chapman-Stern model at slightly positively charged oxide-electrolyte interface. Anions surrounded by water molecules are attracted to the surface, creating a Stern layer. The diffuse layer starts at the outer Helmholz plane (OHP) and extends into the bulk to the Debye length; (b) schematic of potential and (c) charge distribution at the oxide-electrolyte interface.

series.

$$C_{dl} = \frac{C_{Stern} C_{diff}}{C_{Stern} + C_{diff}} \tag{2.1}$$

Stern capacitance is typically $0.2F/m^2$ [72]. Diffuse layer capacitance is determined by the ionic strength of the electrolyte, and the characteristic length of the diffuse layer is given by the Debye length:

$$\lambda_D = \sqrt{\frac{\epsilon \epsilon_0 k_b T}{2 N_a e^2 I_c}} \tag{2.2}$$

where N_a is Avogadro constant and I_c is ionic strength:

$$I_c = \frac{1}{2} \sum c_i {z_i}^2 \tag{2.3}$$

where c_i is ion concentration, z_i is the change in the number of the ion. Diffuse layer capacitance is calculated assuming a simple parallel plate capacitor [70]. Therefore for the monovalent electrolyte of 50 mM concentration, the double layer capacitance can be estimated as $C_{dl} = 0.14\ F/m^2$.

Site-binding model

The site-binding model, developed by Bousse, de Rooij and Bergveld describes the ISFET's response to pH by charging double layer capacitance [70]. It assumes that the oxide surface is covered with hydroxyl groups (OH), which can accept or donate protons. Therefore, depending on the pH of the bulk solution, a different number of hydroxyl groups will be protonated (OH^+) or deprotonated (O^-). This results in surface sites (M) to be neutral (MOH), positively (MOH_2^+) or negatively (MO^-) charged.

$$MOH \leftrightarrows MO^- + H_s^+, K_a = \frac{\nu_{MO^-} a_{H_s^+}}{\nu_{MOH}} \tag{2.4}$$

$$MOH_2^+ \leftrightarrows MOH + H_s^+, K_b = \frac{\nu_{MOH} a_{H_s^+}}{\nu_{MOH_2^+}} \tag{2.5}$$

where $a_{H_s^+}$ is the activity of surface protons, ν - number of surface sites, K_a and K_b are deprotonation and protonation equilibrium constants, respectively. The total number of surface groups per unit area will be the following:

$$N_s = \nu_{MOH} + \nu_{MOH_2^+} + \nu_{MO^-} \tag{2.6}$$

Surface charge, generated by protonated and deprotonated surface sites:

$$\sigma_0 = e(\nu_{MOH_2^+} - \nu_{MO^-}) \tag{2.7}$$

Surface is neutral ($\sigma_0 = 0$) at the point of zero charge (PZC). It happens when $pH = (pK_a + pK_b)/2$. From equations 2.4-2.7:

$$\sigma_0 = eN_s \left(\frac{a_{H_s^+} - K_a K_b}{a^2_{H_s^+} + a_{H_s^+} K_b + K_a K_b} \right) \tag{2.8}$$

The effect of small change in pH on the surface charge density, can be found from the equation 2.7:

$$\frac{\partial \sigma_0}{\partial pH_s} = -q\beta_{int} \tag{2.9}$$

where β_{int} is the intrinsic buffer capacity of the oxide surface. It is called intrinsic because it can buffer small changes in the surface pH, but not in the bulk. Surface buffer capacitance can be defined as follows:

$$C_s = \frac{e^2 \beta_{int}}{2.3 k_b T} \tag{2.10}$$

Due to the charge neutrality, the surface charge σ_0 is compensated by an equal but opposite charge σ_{dl}.

$$\sigma_{dl} = -\sigma_0 = -C_{dl,i}\Psi_0 \tag{2.11}$$

These two charge values form the so-called integral double layer capacitance[71].

The ability of double layer to store charge, when a small change in the surface potential occurs, defined as differential double layer capacitance C_{dl}:

$$\frac{\partial \sigma_0}{\partial \Psi_0} = -\frac{\partial \sigma_{dl}}{\partial \Psi_0} = C_{dl} \tag{2.12}$$

Now combining equations 2.9 and 2.12 we can express the effect of a small change in the surface pH on the surface potential in the following way:

$$\frac{\partial \Psi_0}{\partial pH_s} = \frac{\partial \Psi_0}{\partial \sigma_0} \frac{\partial \sigma_0}{\partial pH_s} = -\frac{q\beta_{int}}{C_{dl}} \tag{2.13}$$

Surface proton activity differs from the bulk proton activity and can be described by the Boltzmann distribution:

$$a_{H_s^+} = a_{H_b^+} exp\left(-\frac{e\Psi_0}{k_b T}\right) \tag{2.14}$$

Since $pH = -log_{10}(a_{H^+})$, we can rewrite equation 2.14 as follows:

$$\Psi_0 = 2.3\frac{k_b T}{e}(pH_s - pH_b) \tag{2.15}$$

Combining equation 2.13 with 2.15, we can derive an equation for the pH sensitivity of an ISFET:

$$\frac{\partial \Psi_0}{\partial pH_b} = -2.3\frac{kT}{q}\alpha \tag{2.16}$$

where α is

$$\alpha = \left(\frac{2.3kTC_{dl}}{q^2\beta_{int}} + 1\right)^{-1} \tag{2.17}$$

Dimensionless parameter α varies between 0 to 1, depending on C_{dl} and β_{int} values. The maximum value of pH sensitivity can be achieved when $\alpha = 1$. In this case, the response will be -59.2 mV/pH at 298 K, the so-called Nernstian response. To be as close as possible to this value, one has to choose gate oxide with a high value of surface buffer capacitance and a low value of double layer capacitance. For instance, β_{int} of SiO_2 is not high enough, resulting in pH sensitivity for ISFETs with such gate oxide of 30 mV/pH. Therefore more studies have been done to find out better options. ISFETs with gate oxides materials such as TiO_2, Al_2O_3, Ta_2O_5, HfO_2 and some more have shown Nernstian response[73].

2.2 Implementation

As an insulating layer in ISFET devices we use Al_2O_3 and HfO_2, as these oxides have high density of surface hydroxyl groups and a high dielectric constant (9 and 25, respectively)[74]. ALD deposition, followed by annealing, ensures the quality of the oxide. It makes them more efficient in use, compared to SiO_2 and perfect candidates for pH sensing[75]. Therefore, pH sensing can be a first straightforward application of an ISFET.

Figures 2.5a, c show transfer curves of the ISFET with different pH of the buffer (liquid gate) and extracted potential, respectively. Almost Nernstian response, 54±3 mV/dec, is observed.

When measuring pH, the gate voltage sweep is done twice, resulting in hysteresis. The V_{th} value is calculated as an average at the same current value. In addition, we record transfer curves first when increasing the pH, and then backwards, from pH 10 to 3. The final response value is an average of V_{th}, extracted from "forward" and "backward" measurement. Plots in figure 2.5a, c show only the measured transfer curves from pH 3 to 10, for clarity.

Gold as a gate material

Having oxide as a gate surface is suitable for pH sensing. However, for other sensing applications, when receptor molecules are attached to the surface, it may not be the best option. Due to its small size, protons from the solution can diffuse between the receptor molecules and interact with the surface hydroxyl groups, leading to an additional change in signal, that can be higher than

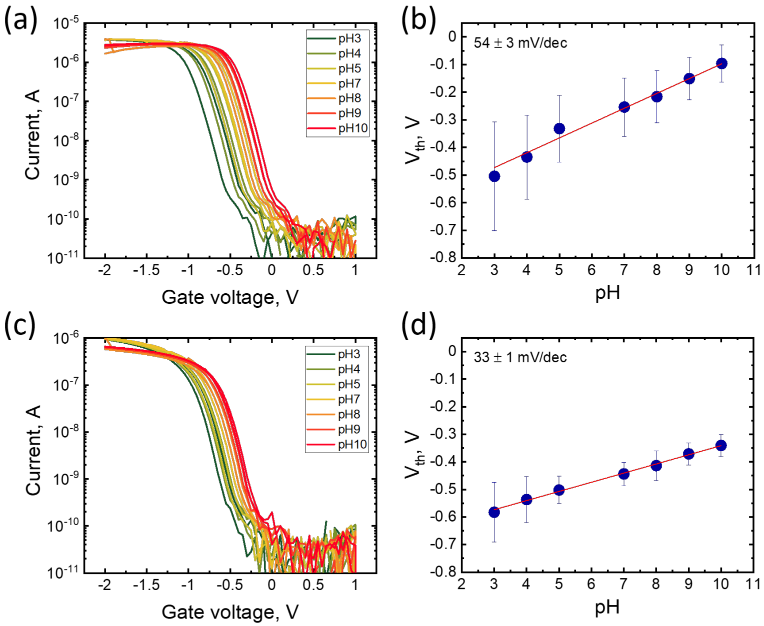

Figure 2.5 (a), (c) Transfer curves, measured in Titrisol pH buffer solutions (pH 3 - 10) with HfO_2 and Au as a gate material, respectively; (b), (d) Extracted values of threshold voltage are plotted versus pH. The slope of the linear fit gives a response value of 54±3 mV/dec and 33±1 mV/pH, respectively.

the specific one. Such simultaneous interactions, surface-proton, and receptor-target are called competing surface reactions. ISFETs detect the overall change in the potential at the surface, which makes it not possible to distinguish contributions from such two reactions.

Several solutions to this issue are possible. One opportunity is to experiment with different gate materials. For example, gate oxide can be additionally coated with gold. This allows functionalizing surface with various receptor molecules with thiol chemistry. As initially expected, gold should not have a response to pH. However, as it is shown in the figure 2.5d, gold-coated surfaces also show response to the pH, although it is lower compared to the oxide surfaces. The reason for this is that approximately 1% of gold atoms are oxidized, and they respond to pH changes[76]. Another option to suppress the pH response pH is surface passivation - functionalizing surface with a dense monolayer of molecules, not selective to any target[76]. This approach is also useful for preventing target species from interacting with a sensing surface. We describe this in more detail in Chapter 4, when discussing competing non-specific adsorption of Cu^{2+} on gold surface.

Potentiometric sensing opens up plenty of possibilities to use already known materials and molecules differently for sensing purposes. On the other hand, comparing the potential of the molecule before and after its complexation with a target allows gaining a deeper insight into their interaction.

2.3 Measurement devices

Two types of devices were used throughout the present thesis: silicon nanoribbon (Si-NR) ISFET device and extended gate-like device with patterned gold electrodes on a glass substrate (figure 2.6a, b respectively).

2.3.1 ISFET based sensor

The working principle of an ISFET is described above. Fabrication process of an ISFET device is described in details in the thesis of Dr. Kristine Bender[77] and in our previous work[56,57,78]. We also provide a summary below. Our measuring setup consists of an ISFET device, electrical interface to the measurement units using a printed circuit board (PCB), and a microfluidic interface to a reference electrode; reference electrode, Keithley source-measure unit, voltmeter, peristaltic pump, valve, switch, holder with the solutions to measure.

Device fabrication

The ISFET devices were fabricated from a p-doped silicon-on-insulator (SOI) wafer (Soitec, France) with a buried oxide 145 nm thick, by a top-down approach.

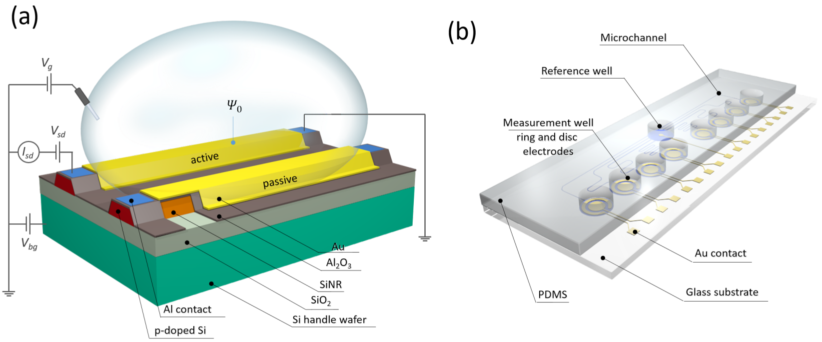

Figure 2.6 Schematics of (a) ISFET and (b) extended gate-like gold electrode device.

The structure of the device is shown in figure 2.7. The top Si(100) layer of the SOI wafer (p-type, 85 nm thick, resistivity 8.5–11.5 Ω) was thermally oxidized to grow a 15 nm thick SiO_2 layer. A device pattern with 48 SiNRs was defined by electron beam lithography (EBL) and etched using a combination of reactive ion etching (SiO_2 layer) and wet etching (Si device layer) with a mixture of tetramethylammonium hydroxide (TMAH) and isopropyl alcohol (IPA) 9:1 at 45°C. The etched NRs were typically 10 µm long, 80 nm high, and 1–25 µm wide. The source and drain of each transistor were doped with boron, and then thermally annealed in a forming gas to activate the dopants (6 min, 950°C). As an insulation layer, a 20 nm thick Al_2O_3 layer was deposited using atomic layer deposition (ALD) at 225°C. Contact pads were opened by wet etching with buffered hydrofluoric acid (BHF), and 300 nm thick Al–Si (1%) pads were deposited by electron beam evaporation and annealed at 450°C. To extend the range of application and enable their functionalization with various receptors, SiNRs were covered with 20 nm thick gold film (with a 5 nm chromium adhesion layer) by electron beam evaporation. This coating partially suppresses the response to H^+ and permits the use of thiol chemistry for surface functionalization. For additional protection and to create microfluidic channels, the devices were covered with a 2 µm thick layer of SU-8. Finally, the wafer was diced, and devices were wire-bonded to the chip carriers. The bonds were sealed with epoxy (Epotek 353ND).

Microfluidic Channels for ISFET device

Microfluidic channels were fabricated to reduce the required amount of analyte solutions for the measurements and to automatize solutions exchange.

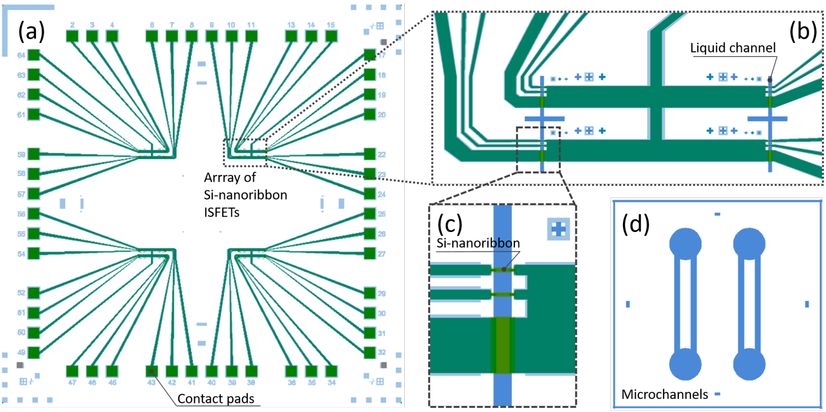

Figure 2.7 (a) Layout of the ISFET based device: 48 ISFETs, arranged in 4 arrays. Each ISFET has an individual source; the drain is common for the ISFETs in the array. Close-up to the array (b) and the pixel (c) of three ISFETs, of 1 µm and 25 µm thickness. (d) Layout of the SU-8 mold for the PDMS channel fabrication.

Polydimethylsiloxane (PDMS) was poured onto a 100 µm thick SU-8 layer on Si, acting as a master, and patterned by EBL with the desired channel structure (two channels in our case). PDMS was cured for 2 h at 60°C and peeled off from the wafer. Two holes at the beginning and at the end of each microchannel were punched to connect polytetrafluoroethylene (PTEE) tubes for solution exchange. The whole system was then placed in a larger mold, and more PDMS was added to stabilize the microfluidic chamber.

Reference electrode

A reference electrode is an essential component of the potentiometric measurement device. It is used to set the stable potential of the electrolyte. In this work, we used standard and leakless Ag/AgCl reference electrodes for our ISFET-based sensor. In the case of the extended gate gold electrode device, we integrated the reference electrode in the sensor. This approach will be described later.

Measurement procedure

Two measurement procedures were used: steady-state and real-time (figure 2.8). In the first case, the samples were stabilized for 1 min after solution exchange.

A potential of 100 mV was applied between source and drain. The source-drain current was measured while sweeping the gate voltage, applied with the reference electrode. From the measured transfer curves, we extracted a threshold voltage (V_{th}) at a given conductance value of 20 nS. Performing such measurement while increasing $Cu(NO_3)_2$ concentration resulted in a relative shift of the transfer curves. We quantified the change in the surface potential of the devices by extracting V_{th} and plotting it versus concentration. A linear fit to this data gave us the response of the device in mV/decade. As we operated the p-type semiconductor in the accumulation regime, the change in surface potential was given by $\Delta\Psi=-\Delta V_{th}$[79].

We measured the response of gold-coated SiNRs, functionalized with the GGH peptide (active surface). To exclude possible contributions from nonspecific interactions, as well as superimposed signals, we also measured the response of the reference, bare gold as control (passive surface). The differential response, characterizing the response due to the active molecular layer, was obtained by subtracting the control SiNRs signal from the active SiNRs signal.

In real-time measurements, a constant source-drain voltage (100 mV) and constant gate voltage (defined by the linear response regime of the device) were applied, and the source-drain current (I_{sd}) was monitored versus time. Changes in surface potential while flushing different solutions could be quantified by normalizing the source-drain current by the transconductance (g_m) of each individual NR as follows: $\Delta\Psi=-\Delta I_{sd}/g_m$. Possible drifts during the measurement were corrected by subtracting the baseline. It was defined as a linear fit of the measured data of electrolyte solution only, prior addition of copper ions (at least the first five minutes of the measurement). For plotting experimental results, the measured curves were shifted to 0 for clarity, as we measured the change in the surface potential, not the absolute value. At each “step” in concentration, the surface potential shift value for each $Cu(NO_3)_2$ concentration was extracted by averaging the data points after a 1 minute stabilization time.

2.3.2 Extended gate-like gold electrode sensor

The second setup, used in this work, consists of a gold electrode sensor with an integrated Ag/AgCl reference electrode, a buffer amplifier board, a power source, a data acquisition (DAQ) card, and a PCB, to which the sample is connected via spring-loaded contacts. For the data acquisition, we use LabView in-house developed software with both setups. Gold electrode device consists of a glass substrate with patterned gold electrodes and a PDMS with microfluidic channels and wells for solutions (figure 2.9).

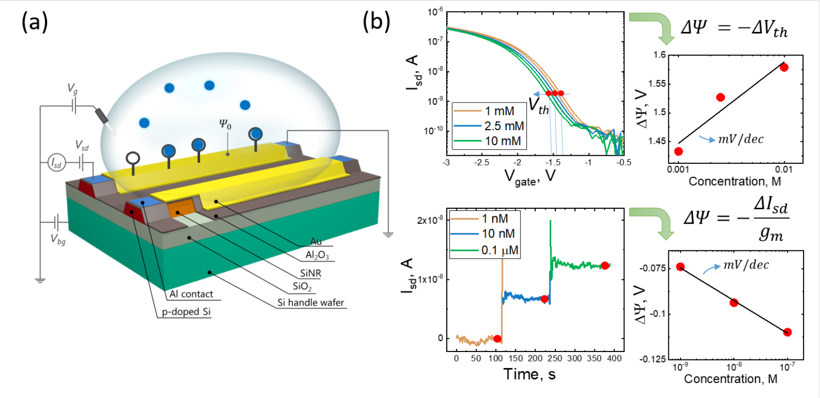

Figure 2.8 (a) Schematics of the device structure with two Si-NR based ISFETs. The potential of 100 mV is applied between the source and drain of each ISFET. The back gate is at 0 V. The gate potential is applied with the reference electrode, and the source-drain current is measured for active (Au-GGH) and passive (Au) surfaces; (b) Schematics of the device's response: steady-state and time-dependent measurements.

Device fabrication

Gold electrodes were fabricated on a previously cleaned (for 5 min in Acetone, Isopropanol, and DI water in an ultrasonic bath at 50°C) glass substrate with a resist layer (AZ 5214E), patterned using UV photolithography. 50 nm of gold with 5 nm of titanium as adhesion layer was thermally evaporated on the pre-patterned glass substrate, followed by the lift-off process. Two types of electrodes were used: disk and ring electrodes of the same surface area (figure 2.9b, c). The fabrication process is described in detail in Appendix A.

Microfluidic Channels for gold electrode device

Microfluidic channels were fabricated to ensure the same potential in all wells of the device. PDMS was prepared in the same way as for the ISFET device, using SU-8 mold of a different design (figure). After PDMS was cured, holes of 5 mm diameter were punched, to create wells to access the gold electrodes. PDMS with patterned microchannels was bonded to a glass substrate. Gold electrode devices and PDMS were cleaned in Isopropanol for 10 mins, dried with a nitrogen gun, and placed in UVO plasma cleaner for 10 mins. Then PDMS was placed on the glass, aligned ensuring no overlap with gold electrodes, and pressed to avoid air bubbles. Afterwards, devices were placed on a hot

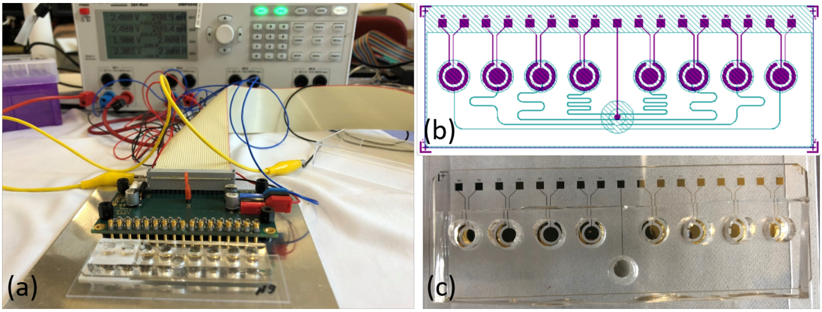

Figure 2.9 (a) Measurement setup: extended gate device, PCB board with spring-loaded pins, DAQ card, power source; (b) Layout of the gold electrode device (purple); patterned microchannels on PDMS part (blue); (c) fabricated device.

plate at 80°C for 10 mins.

Microfluidic reference electrode

The reference electrode was prepared using Ag/AgCl (DuPont 5876) paste and KCl-agarose gel. The gold electrode in the reference well was covered with Ag/AgCl paste and heated on a hot plate, increasing temperature from 80°C to 140°C degrees and then letting it cool down to 60°C. KCl-agarose gel was prepared using the following components: 50 mL of Milli-Q water, 0.5 g agarose (add exact name), and 3.7 g of KCl. This creates a solution of 1 M KCL and 1% of agarose. Mixing was done with a magnet on a hot plate at 80°C for at least 3 hours. KCl-agarose solution was added to the reference well and pushed through the microchannels, ensuring it reaches each well. Such mixture jellifies at room temperature after 10-15 mins. Then reference well was filled more with KCl-agarose solution. After it jellified, 1M KCl was added to all the wells for storage, to prevent drying of reference gel.

Measurement procedure for gold electrode device

For extended gate-like gold electrode devices, a real-time measurement procedure was used. We monitor the change in surface potential with time upon changing conditions in the wells. PCB board contains circuits with an operational amplifier (OpAmp) for each electrode, to enable the readout of high-impedance electrodes by the data acquisition card (DAQ). Each OpAmp is switched in a signal repeater mode, followed by RC low-pass filter, to create a low impedance signal, which comes to the input of DAQ (add figure). Solutions were exchanged or modified to increase metal ion concentration by adding the required solution with a pipette. Typically 5 μl of metal salt solution was added to 50 μl of solution in the well; after mixing 5 μl of the solution was extracted, to keep the same volume.

Functionalization of the sensor surface

For both, ISFET and gold electrode devices, the gold surfaces of our measurement devices were functionalized with peptides. Partial functionalization of ISFET devices, to have half of SiNRs as control surfaces, was achieved using a pump and microfluidic system. ISFET devices were cleaned with UV–ozone, rinsed with Milli-Q water and covered with PDMS microchannels. The devices' surfaces were functionalized by flushing a LpaGGH solution (83 µM) in Milli-Q water through one of the microfluidic channels for 12 hours in total, in sequences alternating between 10 s of flushing (solution refresh) and 1000 s of functionalization time. This procedure was used for steady-state measurements.

For the real-time measurements, an assembly process was performed. The peptide solution was applied to the device surface for typically 12 hours. This method has the advantage of sparing material, as only about 50 µl of the peptide solution is necessary. The same procedure was used for the functionalization of the extended gate-like gold electrode device with OT. 50 µl of OT solution (0.25 g/l) in Milli-Q water was placed in the wells and kept overnight for at least 12 hours.

Electrolyte, Cu^{2+} and Zn^{2+} ion solutions

For the experimental data, presented in this thesis, the ammonium acetate solution (5 M), pH buffers Titrisol, copper (II) nitrate trihydrate, and zinc (II) nitrate were purchased from Sigma Aldrich and diluted with Milli-Q water to the required concentration. The pH was adjusted using KOH and HCl. As previously shown, K^+ and Cl^- ions do not affect the $GGH - Cu^{2+}$ binding[80].

2.4 Peptides as receptor molecules

Selecting a receptor molecule is essential for the performance of a potentiometric sensor. The main selection criteria are selectivity, specificity, and high affinity to the target species. The receptor molecule must also be close to the surface and small (due to the Debye screening). Additionally, from a practical point of view, a simple assembly process on the ISFET gate surface is beneficial. For example, prior conjugation of a receptor with a molecule that contains sulfur group at the end allows direct assembly on the gold surface.

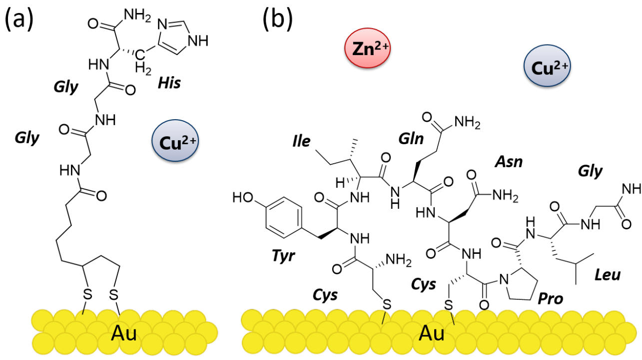

Figure 2.10 Schematic of the peptide (a) LpaGGH and (b) Oxytocin (OT) with amino acids specified in bold, assembled on the gold surface. GGH peptide is known to selectively bind copper ions with high affinity, and OT shows selective binding of Cu^{2+} and Zn^{2+} ions.

Peptides are well suited for this purpose. They are also very interesting objects to investigate as they are present in the human body and participate in many important biochemical processes, many of which involve the binding of metal ions. Therefore peptides that are naturally selective to metal ions can also be used in sensors as receptor molecules.

Two peptides were used in this work for detection of metal ions: Glycyl-Glycyl-Histidine (GGH) and Oxytocin (OT) (figure 2.10a).

2.4.1 GGH peptide

For the detection of Cu^{2+} ions, we used a monolayer of GGH peptide (2.10a), assembled on the surface of our device. The peptide was conjugated with lipoic acid before grafting it onto the surface. Cu^{2+} binding to GGH peptide starts from nitrogen atom of pyridine in the imidazole ring, followed by the deprotonation of consecutive secondary amides in planar geometry (ATCUN motif)[81]. The selectivity of the GGH peptide towards Cu^{2+} ions has been shown in literature[82,83]. The GGH peptide, conjugated with a lipoic acid was synthesized by a standard HATU-based solid-phase peptide synthesis protocol, and its assembly on the surface was characterized with X-ray photoelectron spectroscopy (XPS) as described in previous work[80] by the group of Prof. Shlomo Yitzchaik at the Hebrew University of Jerusalem.

A large range of binding constants ($10^6 - 10^{12} M^{-1}$) of GGH peptide to Cu^{2+} ions can be found, as shown in the table below[84–87].

Cu-GGH binding constants, M^{-1}		
$(15.1 \pm 2.03) \times 10^6$	in solution (50 mM HEPES buffer, pH 7.4)	[84]
1.6×10^{12}	in solution (100 mM KCL) (100 mM KOH for pH adjustment)	[85]
$(4.4 \pm 0.3) \times 10^8$	poly(3-thiopheneacetic acid) (PTAA) modified gold electrode (50mM ammonium acetate & NaCl, pH 7)	[86]
$(8.1 \pm 0.4) \times 10^{10}$	3-mercaptopropionic acid (MPA) modified gold electrode (50 mM ammonium acetate, pH 7)	[87]

Such a broad range of the reported values is caused by the complexity of their determination. The obtained values depend on the environmental conditions (pH, the composition of the solution) and the deprotonation state of the peptide. GGH can have different deprotonation states, depending on the pH of the media, which will therefore influence the binding affinity as previously reported, for instance, for peptides with histidine residue[88].

Sensitivity of GGH peptide as a part of a sensing device has been reported in the concentration range from femto- to micromolar[80,89,90].

2.4.2 Oxytocin

For the detection of both, Cu^{2+} and Zn^{2+} ions, we used neuropeptide Oxytocin (figure 2.10b). This peptide consists of nine amino acids: cysteine, tyrosine, isoleucine, glutamine, asparagine, cysteine, proline, leucine, glycine-amide ($Cys - Tyr - Ile - Gln - Asn - Cys - Pro - Leu - Gly - NH_2$), forming a "ring" and a "tail". Oxytocin is known to bind both, Cu^{2+} and Zn^{2+} ions[91,92].

An additional property of this peptide, attractive for our application, is its direct assembly on a gold surface. This is possible due to the presence of a double sulfur bond between two cysteine amino acids that form part of the "ring". Direct surface functionalization is possible due to the breaking of double Sulfur $S - S$ bond and consecutive sulfur binding to gold atom. It has been shown that double Sulfur bond does not participate in the OT complexation process with Cu^{2+} and Zn^{2+} ions and also that complexation with Cu^{2+} and Zn^{2+} ions takes place when OT is assembled on the surface[93].

Different binding mechanisms of Cu^{2+} and Zn^{2+} ions to OT were reported[91,93–97]. Studies suggest that Cu^{2+} ion binds to the OT via deprotonated amide groups, and Zn^{2+} via carbonyl groups. Multiple complex configurations are possible, as different amino acids can be involved in the binding of an ion, as shown in figure 2.11. However, independently of amino acids that form binding sites, the type of groups involved remains the same. The final complex charge

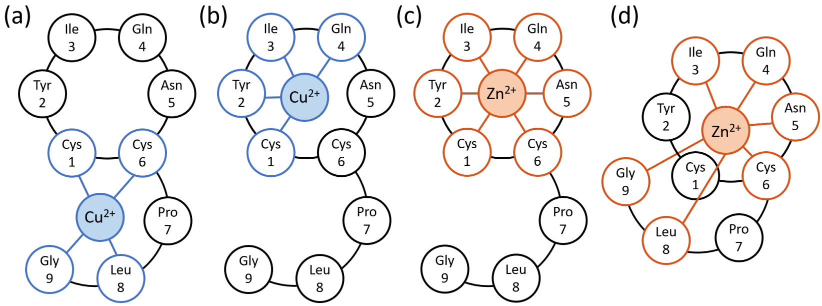

Figure 2.11 Schematic of OT, shown as "ring" and "tail" with amino acids, specified in rings. (a), (b) OT-Cu and (c), (d) OT-Zn complexes. Amino acids highlighted in blue are involved in Cu^{2+} binding, highlighted in orange - in Zn^{2+} binding.

is 1− for OT-Cu and 2+ for OT-Zn, which is important for our application, as we measure the change in the potential at the surface, and having complexes of different charges can help to differentiate between the two ions.

The binding of both ions to the same OT is unlikely. After binding one ion, a conformational change of the peptide is required to bind the second one. OT is, however, is a relatively small peptide with low flexibility that makes complexation with the second ion unlikely. In addition, in our experiments, OT is attached to the surface, which further restricts the flexibility of the peptide.

Binding affinities of Cu^{2+} and Zn^{2+} ions to OT were not extensively studied. In one study they are estimated to be $9\times10^{4}\ M^{-1}$ and $5\times10^{3}\ M^{-1}$, respectively[98]. These values were determined with OT being in the solution, not assembled on the surface as in our case. Such high values suggest the detection in micromolar range of concentrations. However, the more recent study demonstrates Cu^{2+} and Zn^{2+} ion detection with OT assembled on the surface in the concentration range from femto- to millimolar[93], which we also use in our experiments.

2.5 Conclusion to the overview of our methods

In this chapter, we introduced a concept of potentiometric sensing and the devices that are used in this work: Si-NR ISFET-based device and extended gate-like gold electrode device, discussed their structure and working principle. The first straightforward application of such potentiometric sensors is pH detection. The theoretical basis is given by the site-binding model. Experimental data show the sensitivity of our ISFET-based device close to the Nernstian limit, which defines the highest possible response.

This approach can be developed further for the detection of other analytes. In this case, the surface of the device has to be functionalized with a receptor, selective to the target of interest. The fundamental ability of peptides to interact with ions and form complexes can be utilized for sensing purposes. When a change in the charge of the complex differs from the charge of the peptide before complexation, such peptide can be a very promising candidate for application in potentiometric sensing devices, such as ISFET-based or extended gate-like devices for specific ion detection.

3 Modeling ion binding

Contributions: The model described in Section 3.2 was co-developed by Dr. Mathias Wipf.

Experimental methods give a great opportunity to study systems of interest. Solid theoretical support, however, is equally important and makes the scientific method complete. In the following chapter, we model the change in the surface potential that occurs due to various competing reactions at the surface, specific and non-specific ones.

Since we measure the change in the surface potential with our devices, developing a model that includes the reactions that take place at the surface can help to determine the system-specific parameters, such as receptor-target binding constant and the number of surface sites.

The site-binding model, previously introduced for pH sensing, can potentially be extended to more complex systems. We apply this modeling approach to the receptor-target interaction-induced response.

In this chapter, we develop theoretical models to predict the change in the surface potential upon ion binding to the receptor. We consider three cases: receptor with one binding site and defined only one possible complex charge; receptor that depending on the environment can form complexes of different charge; and the receptor that is selective to two different ions.

3.1 One binding site

First, we consider a receptor molecule that is neutral before binding a divalent ion, and the final complex is negatively charged (1-) due to the release of protons from the ligand. We start with a simple case, considering only a specific binding reaction.

3.1.1 Modeling simple ligand-ion binding

With this simple approach, we consider one reaction that is taking place at the surface: specific metal ion-ligand binding 3.1.

$$Ligand() + Cu^{2+} \leftrightarrows Ligand(Cu^{2+})^{1-} + 3H^{+} \tag{3.1}$$

The dissociation constant of the complex $Ligand(Cu^{2+})^{1-}$ is defined as follows:

$$K_L = \frac{\nu_{Ligand} a^s_{Cu^{2+}}}{\nu_{Ligand(Cu^{2+})^{1-}}} \tag{3.2}$$

$a^s_{Cu^{2+}}$ is the activity at the surface of Cu^{2+} ions. It is related to the bulk activity via Boltzmann distribution:

$$a^s_{Cu^{2+}} = a_{Cu^{2+}} e^{-\frac{2e\Psi_0}{kT}} \tag{3.3}$$

As a next step, we define the total number of surface groups. In the simplified case, we consider two contributions to the total number: the number of ligand molecules that did not bind metal ion, and the number of formed ligand-metal ion complexes:

$$N_{sum} = \nu_{Ligand} + \nu_{Ligand(Cu^{2+})^{1-}} \tag{3.4}$$

Only the $\nu_{Ligand(Cu^{2+})^{1-}}$ will affect the potential at the surface, as ν_{Ligand} is neutral. We can therefore define the charge and then obtain the expression for the surface potential:

$$\sigma = e(-\nu_{Ligand(Cu^{2+})^{1-}}) = -\frac{eN_{sum} a^s_{Cu^{2+}}}{a^s_{Cu^{2+}} + K_L} \tag{3.5}$$

$$\Psi_0 = \frac{\sigma}{C_{dl}} = -\frac{eN_{sum}}{C_{dl}} \frac{a^s_{Cu^{2+}}}{a^s_{Cu^{2+}} + K_L} \tag{3.6}$$

In the final equation, N_{sum} and K_L are the parameters specific to the studied ligand-ion system. Double layer capacitance C_{dl} is assumed to be constant, as ionic strength is dominated by the concentration of electrolyte and is almost not affected by the target ion concentration. We can solve this equation with an in-house developed script in MATLAB.

To evaluate how N_{sum} and K_L affect the final response, we plot Ψ_0 when K_L is fixed (figure 3.1a) and when N_{sum} is fixed (figure 3.1b). Double-layer capacitance value is $C_{dl} = 0.14\ F/m^2$, estimated for an electrolyte solution of 50 mM concentration. In our models, we assume an ideal solution, for which the chemical activity of ionic species (describing the effective concentration) can be approximated as concentration, as $a = c/c_0$, and the standard state is given by $c_0 = 1M$ for ideal solutions.

With an increase of N_{sum} the total change in the surface potential over the selected range of concentrations increases, with a plateau at lower concentrations ($10^{-14} - 10^{-12}$ M) and higher concentrations ($10^{-8} - 10^{-7}$ M) for all the N_{sum} values. Binding constant K_L does not affect the total change in the surface potential. An increase of K_L shifts the curve along the x-axis to the right, indicating that ligand's sensitivity to the target decreases.

So far, we have considered only a simple ion-receptor binding reaction.

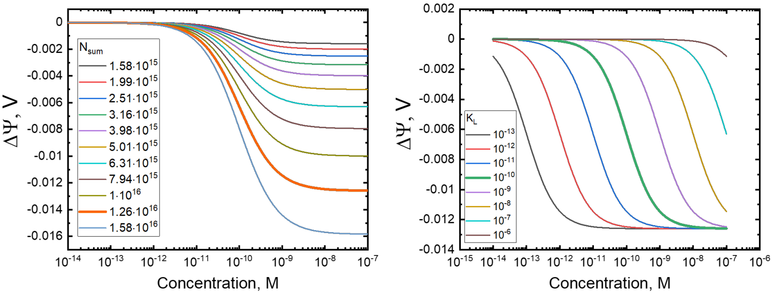

Figure 3.1 Modeled change in the surface potential with increase of metal ion concentration: (a) for different N_{sum} and (b) for different K_L. The thick line in the plot (a) highlights the value, used for the calculations for the different K_L ($N_{sum} = 1.26 \times 10^{16}\ m^{-2}$), and a thick line in the plot (b) highlights the value used for the different N_{sum} ($K_L = 10^{-10}$ M).

However, since initially the ligand is neutral and the final charge of the complex is 1−, the ligand has to release three protons.

For developing the model further, it is important to include these three deprotonation reactions, that are taking place before metal ion binding, as we discuss in the following section.

3.1.2 Modeling ligand-ion binding including deprotonation

To make the model closer to the real case, we add the deprotonation reactions to the model described in previous section. As in the previous case, we start with the specific reaction (3.7).

$$()Ligand()^{3-} + Cu^{2+} \leftrightarrows ()Ligand(Cu^{2+})^{1-} \tag{3.7}$$

The deprotonation of the peptide can be included considering the following reactions:

$$\begin{aligned}
(3H^{+})Ligand() &\leftrightarrows (2H^{+})Ligand()^{1-} + H^{+} && (3.8)\\
(2H^{+})Ligand() &\leftrightarrows (H^{+})Ligand()^{2-} + H^{+} && (3.9)\\
(H^{+})Ligand() &\leftrightarrows ()Ligand()^{3-} + H^{+} && (3.10)\\
& && (3.11)
\end{aligned}$$

Dissociation constants are defined as follows, for the deprotonation reactions and the specific reaction, respectively:

$$K_1 = \frac{\nu_{(2H+)Ligand()-} a^s_{H+}}{\nu_{(3H+)Ligand()}} \tag{3.12}$$

$$K_2 = \frac{\nu_{(H+)Ligand()^{2-}} a^s_{H+}}{\nu_{(2H+)Ligand()^{-}}} \tag{3.13}$$

$$K_3 = \frac{\nu_{()Ligand()^{3-}} a^s_{H+}}{\nu_{(H+)Ligand()^{2-}}} \tag{3.14}$$

$$K_L = \frac{\nu_{()Ligand()^{3-}} a^s_{Cu^{2+}}}{\nu_{Ligand(Cu^{2+})^{1-}}} \tag{3.15}$$

In the expression of total number of surface sites, considered in the previous model (3.4), we include also number of ligands that are deprotonated, but have not bound the ion yet.

$$N_{sum} = \nu_{(3H+)Ligand()} + \nu_{()Ligand()^{3-}} + \nu_{()Ligand(Cu^{2+})^{1-}} \tag{3.16}$$

Deprotonated form of the ligand contributes to the net charge:

$$\sigma = e(-3\nu_{()Ligand()^{3-}} - \nu_{()Ligand(Cu^{2+})^{1-}}) \tag{3.17}$$

The final equation for the surface potential:

$$\Psi_0 = -\frac{eN_{sum}}{C_{dl}} \frac{3 + a^s_{Cu^{2+}}/K_L}{(a^s_{H+})^3/(K_1 K_2 K_3) + a^s_{Cu^{2+}}/K_L + 1} \tag{3.18}$$

Figure 3.2 shows the 3D plot, surface potential versus pH and ion concentration. At pH 5 and 6, the potential is not changing with the increase of ion concentration. At pH7, Ψ_0 decreases, and from pH 8 to 10 increases. Along the pH axis, surface potential is decreasing towards more basic pH, as the ligand releases more protons from its structure. As in the previous case, modeled potential has two plateaus, for the lowest and highest concentrations. The response region is from 10^{-12} to 10^{-8} M concentration with $K_L = 10^{-10}$ M.

In this modeling approach, we took into account specific ligand-ion interaction and the deprotonation of the ligand. In real systems, however, non-specific competing reactions between the target ions and a surface occur. In the following section, we integrate such non-specific interactions into the model.

3.1.3 Impact of non-specific interaction of metal ions with surafce

We modify the equation for N_{sum} (3.16) from the model that includes deprotonation of the ligand by adding a term for the number of surface sites, occupied

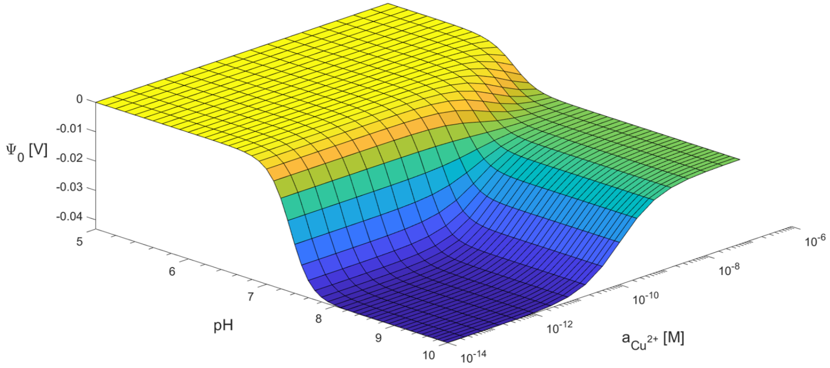

Figure 3.2 Surface potential versus pH and Cu^{2+} ion concentration described by equation 3.18. Parameters used in this model are the following: $N_{sum} = 1.26 \times 10^{16}\ m^{-2}$, $K_L = 10^{-10}\ M$, $K_1K_2K_3 = 10^{-22}\ M^3$.

by a metal ion.

$$N_{sum} = \nu_{(3H^+)Ligand()} + \nu_{()Ligand()^{3-}} + \nu_{()Ligand(Cu^{2+})^{1-}} + \nu_{AuCu} \tag{3.19}$$

Assuming charge +1 for every ν_{AuCu} site, the total charge can be expressed as follows:

$$\sigma = e(-3\nu_{()Ligand()^{3-}} - \nu_{()Ligand(Cu^{2+})^{1-}} + \nu_{AuCu}) \tag{3.20}$$

K_1, K_2, K_3 and K_L remain the same as in the previous model (equations 3.12-3.15). In order to integrate the number of non-specific binding sites but to keep the number of parameters in the model as low as possible, we introduce a parameter r, that is a ratio of the number of sites occupied by Cu^{2+} ion to the number of formed complexes:

$$r = \frac{\nu_{AuCu}}{\nu_{()Ligand(Cu^{2+})^{1-}}} \tag{3.21}$$

Finally we obtain the following expression for the surface potential:

$$\Psi_0 = -\frac{eN_{sum}}{C_{dl}} \frac{3 + a^s_{Cu^{2+}}(1-r)/K_L}{{a^s_{H^+}}^3/(K_1K_2K_3) + a^s_{Cu^{2+}}(r+1)/K_L + 1} \tag{3.22}$$

In this equation we set constant pH ($aH^+ = 10^{-7}$) and we plot Ψ_0 versus ion concentration and the ratio r (figure 3.3). Parameter r is in the range from 0 to 2. Values $r < 1$ indicate less non-specific adsorption, and on the plot, we can see that potential in decreasing with an increase of ion concentration.

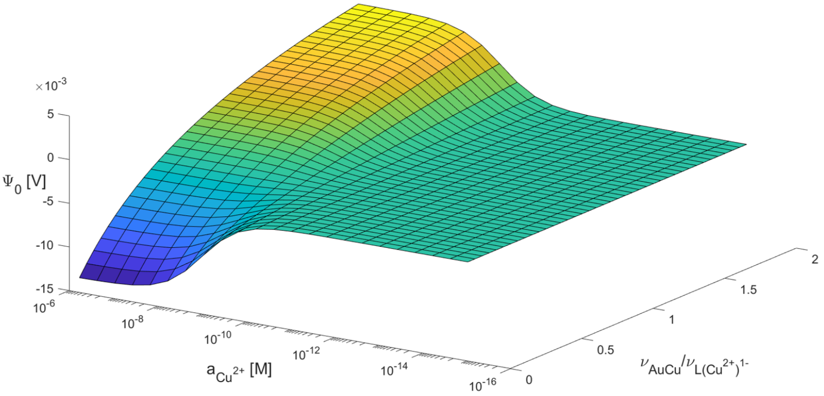

Figure 3.3 Surface potential versus Cu^{2+} ion concentration and the ratio of number of non-specific binding sites to the number of Ligand-Cu complexes described by equation 3.22. Parameters used in this model are the following:$N_{sum} = 1.26 \times 10^{16} m^{-2}$, $K_L = 10^{-10} M$, $K_1 K_2 K_3 = 10^{-22} M^3$.

This is expected, as the complex is negatively charged. For the $r > 1$, when non-specific interaction is dominating, Ψ_0 increases with the increase of ion concentration, which also corresponds to the expected trend.

This model is more accurate than the previous ones, although it is still a simplification of a real system. We don't know how exactly non-specific adsorption impacts the potential and multiple reactions that we consider in the model are happening simultaneously. Nevertheless, modeling the surface charge can provide an insight into the system, and depending on its complexity, the modeled surface potential can be correlated with the experimental data in order to obtain parameters N_{sum} and K_L.

3.2 Formation of multiple complexes upon ion binding

Until now we modeled the ligand-ion interaction, assuming that only one type of complex can be formed. In this section we look into the system, when four ligand-ion complexes are possible.

Such system is illustrated in the figure 3.4. Schematically ligand is shown in the top left corner on the figure 3.4. Ends on the blue lines creating "+" represent four groups that are involved in ion binding. Initially, these four groups are protonated. Figure 3.4 shows possible pathways for the complexation reaction, depending on the number of protons released from the ligand. Depending on the receptor-target interaction, different amount of protons needs to be released in order to bind the target. Number of ligands, assembled on the surface, is NL_0. K_1, K_2, K_3, K_4 are the deprotonation constants, K_{d1}, K_{d2}, K_{d3}, K_{d4} are the dissociation constants. N_{s1}, N_{s2}, N_{s3}, N_{s4} are the numbers of ligand in deprotonated states, NL_1, NL_2, NL_3, NL_4 – amount of ligand-Cu^{2+} complexes. We will use short form for the ligand in different deprotonation states, for instance L^{-1} – ligand, which has released one proton and is negatively charged. We consider two major pathways of $ligand{-}Cu^{2+}$ complexation reaction, indicated on the figure with green arrows. Since we have 2^+ charged target, the respective complexes will be 1^+ and 2^- charged (L^{+1}, L^{-2}). Therefore, selecting these two pathways allows us to describe the system in both cases, when a final surface charge is positive or negative, depending on the conditions in the system and ligand-target interaction. The first important step is to define reactions that take place in the system. To describe different states of the ligand, we use the following template: $(number\_of\_protons)Ligand(target)^{(complex\_charge)}$.

In our case, four deprotonation reactions and two complexation reactions take place:

$$(4H^+)Ligand() \leftrightharpoons (3H^+)Ligand()^{(1-)} + H^+, K_1 \tag{3.23}$$

$$(3H^+)Ligand()^{1-} \leftrightharpoons (2H^+)Ligand()^{(2-)} + H^+, K_2 \tag{3.24}$$

$$(2H^+)Ligand()^{2-} \leftrightharpoons (H^+)Ligand()^{(3-)} + H^+, K_3 \tag{3.25}$$

$$(H^+)Ligand()^{3-} \leftrightharpoons ()Ligand()^{(4-)} + H^+, K_4 \tag{3.26}$$

$$(3H^+)Ligand(Cu^{2+})^{1+} \leftrightharpoons (3H^+)Ligand()^{(1-)} + Cu^{2+}, K_{d1} \tag{3.27}$$

$$()Ligand(Cu^{2+})^{2-} \leftrightharpoons ()Ligand()^{(4-)} + Cu^{2+}, K_{d4} \tag{3.28}$$

K_1, K_2, K_3, and K_4 are the deprotonation constants of the ligand and K_{d1} and K_{d4} are the dissociation constants of the corresponding chelation reaction, as described above and shown in the figure 3.4. Therefore, equilibrium equations for the chemical equations 3.23-3.28 are the following:

$$(4H^+)Ligand() + Cu^{2+} \leftrightharpoons ()Ligand(Cu^{2+})^{2-} + 4H^+,$$
$$K_{total4} = \frac{K_1K_2K_3K_4}{K_{d4}} \tag{3.29}$$

$$(4H^+)Ligand() + Cu^{2+} \leftrightharpoons (3H^+)Ligand(Cu^{2+})^{1+} + H^+,$$
$$K_{total1} = \frac{K_1}{K_{d1}} \tag{3.30}$$

where $K_{d4}, K_{d1}, K_1, K_2, K_3$ and K_4 are defined using activities of Cu^{2+} and

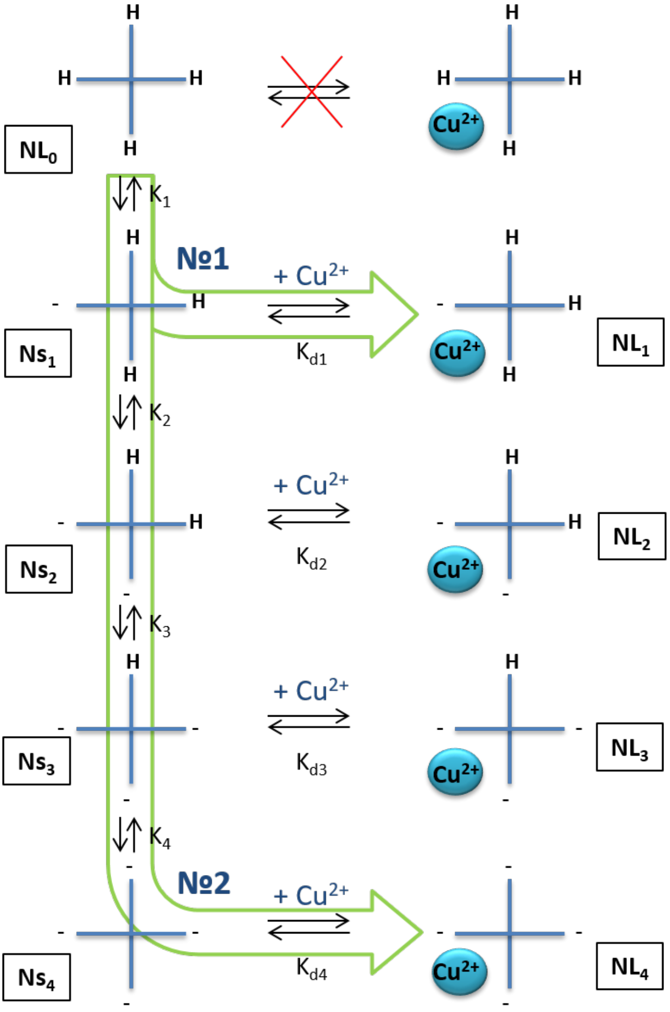

Figure 3.4 Schematic of the different possible reactions of the ligand-target complexation with two assumed major paths.

protons and number of ligands per unit area in different states as:

$$K_{d1} = \frac{a^s_{Cu^{2+}} \nu_{(3H^+)Ligand()^{1-}}}{\nu_{(3H^+)Ligand(Cu^{2+})^{1+}}} \tag{3.31}$$

$$K_{d4} = \frac{a^s_{Cu^{2+}} \nu_{()Ligand()^{4-}}}{\nu_{()Ligand(Cu^{2+})^{2-}}} \tag{3.32}$$

$$K_1 K_2 K_3 K_4 = \frac{(a^s_{H^+})^4 \nu_{()Ligand()^{4-}}}{\nu_{(4H^+)Ligand()}} \tag{3.33}$$

Substituting these expressions into the equations 3.29 and 3.30, we obtain expressions for the dissociation constants:

$$K_{total1} = \frac{a^s_{H^+} \nu_{(3H^+)Ligand(Cu^{2+})^{1+}}}{a^s_{Cu^{2+}} \nu_{(4H^+)Ligand()}} \tag{3.34}$$

$$K_{total4} = \frac{(a^s_{H^+})^4 \nu_{()Ligand(Cu^{2+})^{2-}}}{a^s_{Cu^{2+}} \nu_{(4H^+)Ligand()}} \tag{3.35}$$

With $\nu_{(4H^+)Ligand()}$, $\nu_{()Ligand(Cu^{2+})^{2-}}$, $\nu_{(3H^+)Ligand(Cu^{2+})^{1+}}$ being the numbers of different types of surface sites. Total amount of ligand in the complexed state, following two pathways, can be expressed in the following way:

$$N_{L1} = \nu_{(3H^+)Ligand()^{1-}} + \nu_{(3H^+)Ligand(Cu^{2+})^{1+}} + \nu_{(4H^+)Ligand()} \tag{3.36}$$

$$N_{L4} = \nu_{()Ligand()^{4-}} + \nu_{()Ligand(Cu^{2+})^{2-}} + \nu_{(4H^+)Ligand()} \tag{3.37}$$

We include the number of the respective deprotonated ligands, ion-ligand complexes, and the number of ligand in its initial state, fully protonated.

The total charge (σ) can be obtained by taking into account the numbers of all charged species in the system:

$$\sigma_{1-4} = e(\nu_{(3H^+)Ligand(Cu^{2+})^{1+}} - \nu_{(3H^+)Ligand()^{1-}} - 4\nu_{()Ligand()^{4-}} - 2\nu_{()Ligand(Cu^{2+})^{2-}}) \tag{3.38}$$

Using previously obtained expressions for the dissociation constants, we derive the final equation for the surface potential:

$$\Psi_0 = \frac{\sigma}{C_{dl}} \left[N_{L1} \left(\frac{\frac{a^s_{Cu^{2+}}}{K_{d1}} - 1}{1 + \frac{a^s_{Cu^{2+}}}{K_{d1}} + \frac{a^s_{H^+}}{K_1}} \right) - 2N_{L4} \left(\frac{\frac{a^s_{Cu^{2+}}}{K_{d4}} + 2}{1 + \frac{a^s_{Cu^{2+}}}{K_{d4}} + \frac{(a^s_{H^+})^4}{K_{total4} K_{d4}}} \right) \right] \tag{3.39}$$

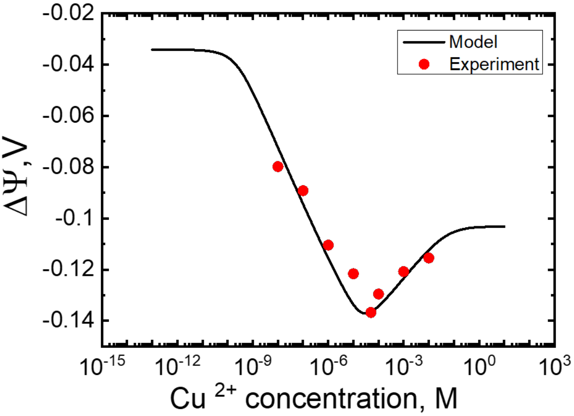

Figure 3.5 Simulated data using our model and experimental data, obtained for the peptide GGH and Cu^{2+} ions at pH 5. We used the following parameters: $NL_4 = 0.75 \times 10^{17} m^{-2}, K_1 = 10^{-7.5} M, K_{d1} = 10^{-0.5} M, K_{d4} = 10^{-9} M, K_{total4} = 2.5 \times 10^{-10} M^3$.

Where N_{L1} and N_{L4} are:

$$N_{L1} = N_{\Sigma} \left(\frac{K_{d1}}{a^s_{Cu^{2+}}} + \frac{K_{total4} K_{d1}}{(a^s_{H^+})^3 K_1} + \frac{K_{total4} K_{d1} K_{d4}}{a^s_{Cu^{2+}} K_1} + \frac{K_{d1}}{a^s_{Cu^{2+}} K_1} + 1 \right)^{-1} \tag{3.40}$$

$$N_{L4} = N_{\Sigma} \left(\frac{K_{d4}}{a^s_{Cu^{2+}}} + \frac{(a^s_{H^+})^3 K_1}{K_{total4} K_{d1}} + \frac{(a^s_{H^+})^3 K_1}{a^s_{Cu^{2+}} K_{total4}} + \frac{(a^s_{H^+})^4}{a^s_{Cu^{2+}} K_{total4}} + 1 \right)^{-1} \tag{3.41}$$

And N_{Σ} is the total number of ligands on the surface, participating in the reactions:

$$N_{\Sigma} = N_{s1} + N_{L1} + N_{s4} + N_{L4} + N_{s0} \tag{3.42}$$

We plot the surface potential versus ion concentration using expression 3.39 for different pH.

Figure 3.5 shows a modeled surface potential and the experimental data obtained for the Cu-GGH system in Titrisol buffer at pH 5.

From 10^{-10} to 10^{-5} M ion concentration potential decreases, indicating the formation of negatively charged complexes. From 10^{-4} to 10 M the change in the surface potential is positive, meaning that more positively charged

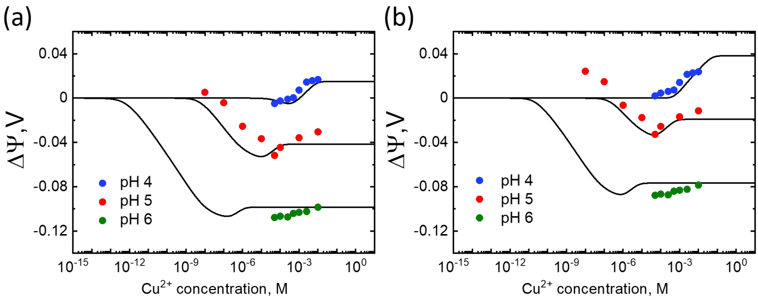

Figure 3.6 Simulated data using our model and experimental data, obtained for the peptide GGH and Cu^{2+} ions at pH 4, 5, 6. We used the following parameters: (a) $Nsum = 2.5 \cdot 10^{17} m^{-2}, K_1 = 10^{-7.5} M, K_{d1} = 10^{-8} M, K_{d2} = 10^{-13} M, Ktotal2 = 2.5 \cdot 10^{-13} M^3$, (b) $Nsum = 3.5 \cdot 10^{17} m^{-2}, K_1 = 10^{-8} M, K_{d1} = 10^{-8} M, K_{d2} = 10^{-20} M, Ktotal2 = 5 \cdot 10^{-15} M^3$.

complexes have been formed. It can be assumed that the prevalence of the first or the second reaction path that we consider in this model is concentration-dependent, with path no.1 dominating in the low range of concentrations (<10^{-5} M) and path no.2 in the high range (>10^{-4} M).

In this model, the parameter $NL_4 = 0.75 \times 10^{17} m^{-2}$ is fixed, however in the real case the number of formed complexes changes with the increase of target ion concentration. Therefore the more correct approach is to keep the total number of surface sites (N_{sum}) constant. Figure 3.6 shows the modeled surface potential change for pH 4, 5, and 6 with N_{sum} being fixed. We use a different set of parameters in figure 3.6 a and b. Focusing on the model for pH 5 and comparing it to the experimental data, we can see that either a similar change in the surface potential or the position of a minimum was obtained. Parameters N_{sum}, K_1, K_{d1}, K_{d2}, K_{tot2} control the total change in the surface potential, the position of a peak minimum, and a slope value. However, the dependence is not always straightforward. Changing one parameter can affect multiple characteristics of the curve.

Although full deprotonation of GGH peptide at low pH (4-6) does not happen and the complex charge is unlikely to depend on the $Cu(NO_3)_2$ concentration range, this model shows an interesting approach for modeling receptor-target systems, when complexes of different charge are formed.

3.3 Selectivity to multiple ions

In this section, we develop a model for a receptor that is selective to two different ions (Cu^{2+} and Zn^{2+}). We consider the case when only one of the ions binds, and the complex charge is 1- and 2+, respectively. We start with a simple case, considering only specific binding reactions, as described in the following section.

3.3.1 Simplified approach

We start building the model with two specific binding reactions:

$$Ligand() + Cu^{2+} \leftrightarrows Ligand(Cu^{2+})^{1-} + 3H^{+} \tag{3.43}$$

$$Ligand() + Zn^{2+} \leftrightarrows Ligand(Zn^{2+})^{2+} \tag{3.44}$$

The dissociation constants are defined, respectively:

$$K_{L1} = \frac{\nu_{Ligand} a^{s}_{Cu^{2+}}}{\nu_{Ligand(Cu^{2+})^{1-}}} \tag{3.45}$$

$$K_{L2} = \frac{\nu_{Ligand} a^{s}_{Zn^{2+}}}{\nu_{Ligand(Zn^{2+})^{2+}}} \tag{3.46}$$

The total number of surface sites (N_{sum}) includes the number of ligand before ion binding ($\nu_{Ligand()}$) and after binding Cu^{2+} or Zn^{2+} ion ($\nu_{Ligand(Cu^{2+})^{1-}}$ or $\nu_{Ligand(Zn^{2+})^{2+}}$, respectively).

$$N_{sum} = \nu_{Ligand()} + \nu_{Ligand(Cu^{2+})^{1-}} + \nu_{Ligand(Zn^{2+})^{2+}} \tag{3.47}$$

Since the ligand is neutral, only complexes will contribute to the net charge at the surface:

$$\sigma = e(-\nu_{Ligand(Cu^{2+})^{1-}} + 2\nu_{Ligand(Zn^{2+})^{2+}}) \tag{3.48}$$

The expression for the surface potential is therefore the following:

$$\Psi_0 = \frac{eN_{sum}}{C_{dl}} \frac{2a^{s}_{Zn^{2+}}/K_{L2} - a^{s}_{Cu^{2+}}/K_{L1}}{1 + a^{s}_{Cu^{2+}}/K_{L1} + a^{s}_{Zn^{2+}}/K_{L2}} \tag{3.49}$$

To assess the impact that dissociation constants have on the surface potential in the case of multiple ion binding, we first evaluate them individually by keeping the concentration and the dissociation constant of the other ion constant. Figure 3.7a shows the change in the surface potential with increase of Cu^{2+} ion concentration for different K_{L1} values, from 10^{-14} to 10^{-5}, and the same approach is used for modeling the response to Cu^{2+} ions (figure 3.7b). For the specific Ligand-Cu binding, the surface potential decreases with an increase of copper concentration as expected, since the Ligand-Cu complex is negatively

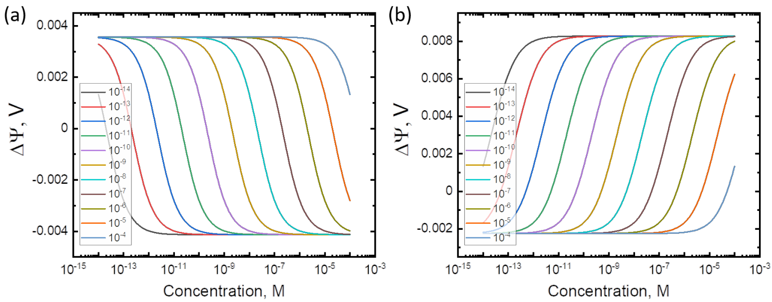

Figure 3.7 Modeled change in the surface potential with increase of metal ion concentration: (a) for different K_{L1} ($K_{L2} = 10^{-8}$ M, $a_{Zn^{2+}} = 10^{-8}$ M) and (b) for different K_{L2} ($K_{L1} = 10^{-8}$ M, $a_{Cu^{2+}} = 10^{-8}$ M).

charged. The sensitivity range is withing three decades of concentration, for example for the $K_{L1} = 10^{-12}$ the potential changed from 10^{-13} to 10^{-10} M (3.7a). An increase of K_{L1} leads to the shift of the curve towards higher concentrations and the total change in surface potential remains the same. For the specific Ligand-Zn binding we observe a positive change in the surface potential, but otherwise, the same trend as for Ligand-Cu: increase of K_{L2} leads to the shift of the curve to the right, and the sensitivity range is also within three decades of concentration.

Figure 3.8 shows the surface potential depending on the concentration of Cu^{2+} and Zn^{2+} ions. As expected, with the increase of metal ion concentration, the surface potential decreases when Ligand-Cu complexes are formed and increases for OT-Zn. The presence of high Zn^{2+} ion concentration, for instance, 10^{-5} M, leads to the shift of the sensitivity region to Cu^{2+} ions, as more OT-Cu complexes need to be formed to overcome high positive net charge due to OT-Zn complexes. The same impact has a high Cu^{2+} ion concentration on the response to Zn^{2+} ions.

So far, we have investigated how the model is affected by the change of only one dissociation constant at a time and when they are equal (figure 3.8). To evaluate the impact of different K_{L1} and K_{L2} combinations on the model output, we plotted four situations, when K_{L1} and K_{L2} are the same or different by four orders of magnitude 3.9.

Interestingly, as shown in figure 3.9a, b the position of slope does not change when both K_{L1} and K_{L2} are increased by for orders of magnitude, meaning that ligand remains sensitive in the same range. When the values are different, 3.9c, d, the curve is shifting to the lower (for lower K_{L1}, K_{L2} values) of the

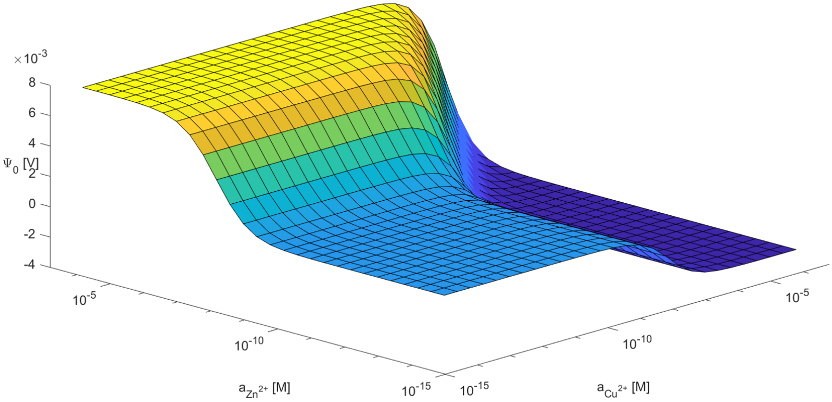

Figure 3.8 Surface potential versus Cu and Zn concentration described by equation 3.49. Parameters used in this model are the following: $N_{sum} = 3.62 \times 10^{15} m^{-2}$, $K_{L1} = K_{L2} = 10^{-8} M$.

higher range of concentrations (for higher K_{L1}, K_{L2} values). Such dependence can make an estimation of binding constants when the model is applied to the real system more challenging, as multiple combinations of K_{L1} and K_{L2} values exist for the sensitivity in the same range of concentrations. In this case, however, the overall change in the surface potential can be used as an indication of the appropriate values of K_{L1} and K_{L2}. As shown in the Figure 3.9a, b, the surface potential change is decreasing from 12 mV (a) to 7.5 mV (b).

3.3.2 Selectivity to multiple ions including deprotonation of the receptor

The negative Ligand-Cu complex charge is due to the release of three protons from the ligand's structure. Similar to the case discussed in Section 3.1.2, we integrate three deprotonation reactions into our model. In this case we consider five reactions:

$$(3H^+)Ligand() \leftrightarrows (2H^+)Ligand()^{1-} + H^+ \tag{3.50}$$

$$(2H^+)Ligand() \leftrightarrows (H^+)Ligand()^{2-} + H^+ \tag{3.51}$$

$$(H^+)Ligand() \leftrightarrows ()Ligand()^{3-} + H^+ \tag{3.52}$$

$$()Ligand()^{3-} + Cu^{2+} \leftrightarrows Ligand(Cu^{2+})^{1-} \tag{3.53}$$

$$Ligand() + Zn^{2+} \leftrightarrows Ligand(Zn^{2+})^{2+} \tag{3.54}$$

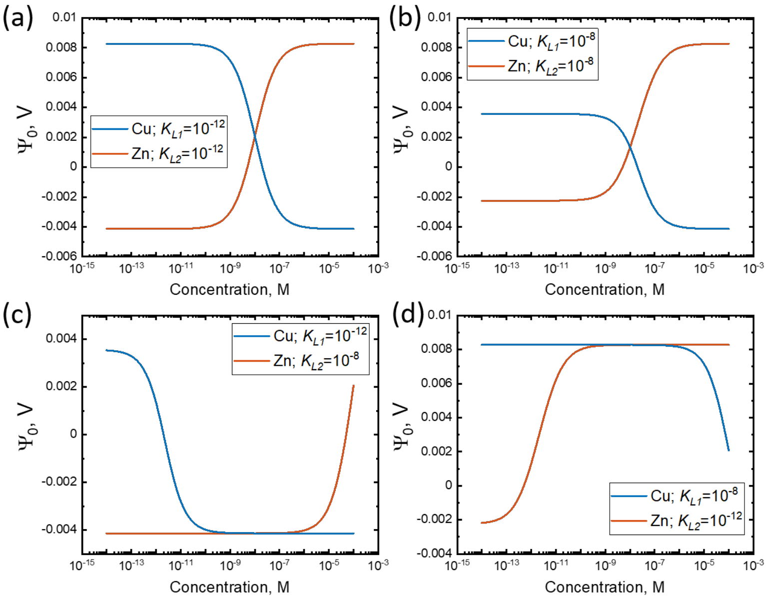

Figure 3.9 Surface potential versus ion concentration for different K_{L1} and K_{L2}, as specified in the legend. Parameters used in this model are the following: $N_{sum} = 3.62 \times 10^{15} m^{-2}$, and binding constants (K_{L1}, K_{L2}) are shown in the legend on each plot.

with the following dissociation constants, respectively:

$$K_1 = \frac{\nu_{(2H^+)Ligand()^-} a^s_{H^+}}{\nu_{(3H^+)Ligand()}} \tag{3.55}$$

$$K_2 = \frac{\nu_{(H^+)Ligand()^{2-}} a^s_{H^+}}{\nu_{(2H^+)Ligand()^-}} \tag{3.56}$$

$$K_3 = \frac{\nu_{()Ligand()^{3-}} a^s_{H^+}}{\nu_{(H^+)Ligand()^{2-}}} \tag{3.57}$$

$$K_{L1} = \frac{\nu_{Ligand} a^s_{Cu^{2+}}}{\nu_{Ligand(Cu^{2+})^{1-}}}, K_{L2} = \frac{\nu_{Ligand} a^s_{Zn^{2+}}}{\nu_{Ligand(Zn^{2+})^{2+}}} \tag{3.58}$$

The total number of surface sites will be given by the sum of the amount of ligand in its neutral state, deprotonated, and the amount of Ligand-Cu and Ligand-Zn complexes.

$$N_{sum} = \nu_{(3H^+)Ligand()} + \nu_{()Ligand()^{3-}} + \nu_{()Ligand(Cu^{2+})^{1-}} + \nu_{()Ligand(Zn^{2+})^{2+}} \tag{3.59}$$

The net charge at the surface can be expressed as follows:

$$\sigma = e(-3\nu_{()Ligand()^{3-}} - \nu_{()Ligand(Cu^{2+})^{1-}} + 2\nu_{()Ligand(Zn^{2+})^{2+}}) \tag{3.60}$$

The final equation for the surface potential:

$$\Psi_0 = -\frac{eN_{sum}}{C_{dl}} \frac{3 + \frac{a^s_{Cu^{2+}}}{K_{L1}} + 2\frac{a^s_{Zn^{2+}}}{K_{L2}} \frac{(a^s_{H^+})^3}{K_1K_2K_3}}{\frac{(a^s_{H^+})^3}{K_1K_2K_3} + \frac{a^s_{Cu^{2+}}}{K_{L1}} + \frac{a^s_{Zn^{2+}}}{K_{L2}} \frac{a^s_{H^+}}{K_1K_2K_3} + 1} \tag{3.61}$$

We fix pH at 7 and plot surface potential versus concentration of Cu^{2+} and Zn^{2+} ions (figure 3.10).

Compared to the previous model, when deprotonation of the ligand was not included, the main difference is a reversed trend in the response to Cu^{2+} ions: the surface potential is increasing, despite the formation of 1− negatively charged Ligand-Cu complexes. This happens due to the low potential in the plateau region that we observe in the low range of concentration, from 10^{-14} to 10^{-10} M, which can be due to the partial ligand deprotonation, causing initially negative net charge at the surface. The binding of Cu^{2+} ion leads to the formation of 1− charged complex, therefore the potential at the surface increases. This is not the case for high Zn concentrations (10^{-8} to 10^{-4} M): the net surface charge is initially positive, and the surface potential decreases upon Cu ion binding, as in the previous model.

Upon the formation of Ligand-Zn complexes, the surface potential increases (in most of the range of Cu concentrations), as expected. Interestingly, we

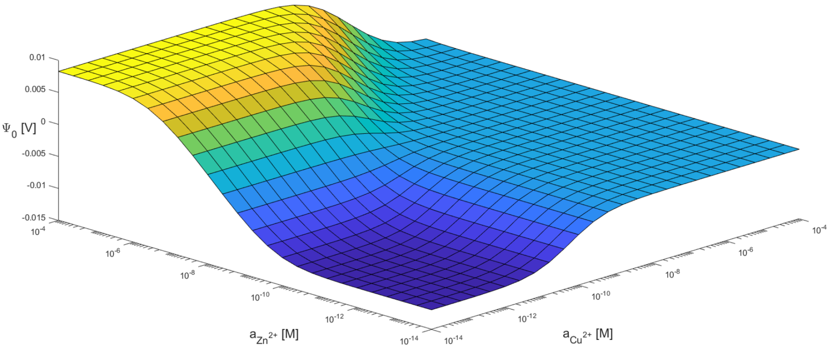

Figure 3.10 Surface potential versus Cu^{2+} and Zn^{2+} ion concentration. Parameters used in this model are the following: $N_{sum} = 3.62 \times 10^{15} m^{-2}$, $K_{L1} = K_{L2} = 10^{-10} M$, $K_1 K_2 K_3 = 10^{-20} M^3$, $a_{H+} = 10^{-7} M$.

observe no change in the surface Ψ_0 upon Zn binding when Cu is at a high concentration ($10^{-5} - 10^{-4}$ M). Such effect could be due to the saturation of the receptors on the surface, if all of them are occupied by metal ions.

3.3.3 Impact of non-specific interaction of Cu^{2+} and Zn^{2+} ions with the surface

To the model that includes deprotonation, developed in the previous section, we add the reactions of non-specific interaction of Cu^{2+} and Zn^{2+} ions with the surface. The total number of surface sites includes, in addition to the ligand states in equation 3.59, includes a number of surface sites occupied by Cu^{2+} and Zn^{2+} ions:

$$N_{sum} = \nu_{(3H^+)Ligand()} + \nu_{()Ligand()^{3-}} + \nu_{()Ligand(Cu^{2+})^{1-}} + \\ + \nu_{()Ligand(Zn^{2+})^{2+}} + \nu_{AuCu} + \nu_{AuZn} \quad (3.62)$$

In the expression for the net charge, we include also contribution from non-specific interaction (ν_{AuCu} and ν_{AuZn}), assuming +1 charge per site.

$$\sigma = e(-3\nu_{()Ligand()^{3-}} - \nu_{()Ligand(Cu^{2+})^{1-}} + 2\nu_{()Ligand(Zn^{2+})^{2+}} + \nu_{AuCu} + \nu_{AuZn}) \quad (3.63)$$

We define parameters r and t as ratios of the number of non-specific interactions with surface sites to the number of formed complexes with Cu^{2+} and Zn^{2+}

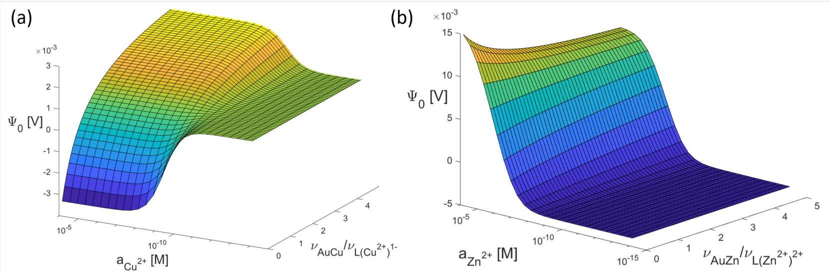

Figure 3.11 Parameters used in these models are the following: $N_{sum} = 3.62 \times 10^{15} m^{-2}$, $K_{L1} = K_{L2} = 10^{-10} M$, $K_1K_2K_3 = 10^{-20} M^3$, $a_{H^+} = 10^{-7} M$ and (a) t=0.0001 while changing r from 0.1 to 5; (b) r=0.0001 while changing t from 0.1 to 5.

ions, respectively:

$$r = \frac{\nu_{AuCu}}{\nu_{()Ligand(Cu^{2+})^{1-}}} \tag{3.64}$$

$$t = \frac{\nu_{AuZn}}{\nu_{()Ligand(Zn^{2+})^{2+}}} \tag{3.65}$$

Defining these parameters allows keeping amount of unknown values at a minimum. The final expression for the surface potential is the following:

$$\Psi_0 = -\frac{eN_{sum}}{C_{dl}} \frac{3 + \frac{a^s_{Cu^{2+}}}{K_{L1}}(1-r) + 2\frac{a^s_{Zn^{2+}}}{K_{L2}} \frac{(a^s_{H^+})^3}{K_1K_2K_3}(2+t)}{\frac{(a^s_{H^+})^3}{K_1K_2K_3} + \frac{a^s_{Cu^{2+}}}{K_{L1}}(1+r) + \frac{a^s_{Zn^{2+}}}{K_{L2}} \frac{a^s_{H^+}}{K_1K_2K_3}(1+t) + 1} \tag{3.66}$$

We plot the surface potential for the two cases: constant concentration of Zn, low non-specific adsorption (t=0.001) (figure 3.11a) to evaluate the effect of non-specific adsorption of Cu on the surface potential; constant concentration of Cu, low non-specific adsorption (r=0.001) (figure 3.11b) to evaluate an impact of non-specific adsorption of Zn ions. In the figure 3.11a we can see that potential is decreasing with an increase of Cu^{2+} ion concentration for low values of r, meaning that the formation of specific Ligand-Cu complexes prevails. For the values $r > 1$, an increase in the surface potential is observed, due to the dominating effect of non-specific interaction of Cu^{2+} ions with the surface.

In the figure 3.11a we observe only increase in the surface potential with an increase of Zn^{2+} ion concentration. For the values of $t < 1$, however, the potential is higher for the concentrations $10^{-6} - 10^{-5}$. This can be explained by the 2+ charge of OT-Zn complexes, whereas Au-Zn interaction is assumed in this model to contribute with a charge +1.

3.4 Conclusions

In this chapter, we modeled the potential at the surface for different types of receptors: the case when only one complex type is formed; the case of the possibility of multiple complexes of ion and receptor; and finally, the case when one receptor is selective to two ions and formation of complexes with one of the other ion leads to the different complex charge. The site-binding model, initially introduced to describe pH sensing, could be also applied to more complex receptor-target systems.

4 GGH peptide for detection of Cu^{2+} ions

Contributions: GGH peptide was obtained from the group of Prof. Shlomo Yitzchaik, Hebrew University of Jerusalem. ISFET devices, used in this work, were fabricated by Dr. Christine Bender. The initial measurement setup was developed by Dr. Mathias Wipf and Dr. Ralph Stoop with subsequent development by Olena Synhaivska and Yves Mermoud. Olena Synhaivska performed the experiments and analyzed the results presented in this chapter.

Some peptides are naturally selective to metal ions, and using them as receptors has great potential not only for ion detection but also for understanding peptide-ion interaction. In this chapter, we systematically study the effect of multiple conditions such as composition and pH of the electrolyte solution, analyte concentration range using Glycyl-Glycyl-Histidine (GGH) peptide for the detection of Cu^{2+} ions.

4.1 Response to Cu^{2+} ions

We performed potentiometric detection of Cu^{2+} ions using SiNR based ISFETs functionalized with a LpaGGH (GGH peptide, conjugated with lipoic acid to allow direct functionalization of the gold surface). We systematically measured the Cu^{2+} response at electrolyte pH ranging from 4 to 8. We used ammonium acetate (50 mM) as an electrolyte solution at pH ranging from 5 to 8 and added $Cu(NO_3)_2$ at a concentration ranging from 0.1 fM to 0.1 µM.

4.1.1 Low Cu^{2+} concentration range

Figure 4.1a shows the change in the surface potential $\Delta\Psi$with increasing $Cu(NO_3)_2$ concentration, starting from ammonium acetate (50 mM, pH 7). The two lines (red and black) represent the Au-GGH (active) and Au (passive) surfaces, respectively. Figure 4.1b shows the extracted values of the surface potential shift (average value for each concentration after 1 min settling time) versus Cu^{2+} concentration. We observe a negative change in surface potential shift upon binding of Cu^{2+} to the immobilized ligand at pH 7 (about -15 mV/dec). Subtracting the response of the control surface (Au, -4 mV/dec) from the active SiNRs (Au-LpaGGH) results in a differential response of -11 mV/dec (blue dots). We plot the differential response to represent the GGH-Cu system without background signal from Cu^{2+} interacting with the Au surface.

At pH 8, we observe a similar trend (Figure 4.1 c, d), with a smaller differential response of -5 mV/dec. The negative differential response appears counter-intuitive as the analyte is positively charged. We would indeed a priori expect an increase in surface potential with increasing of Cu^{2+} ion concentration when the surface charge becomes more positive[56]. However, we anticipate here that the measured negative change in surface potential reveals a more subtle mechanism upon the complexation of Cu^{2+} ions by the GGH ligand, which leads to a net negative charge of the complex, as sensed by the active surface. In these experiments, we don't observe full Nernstian response. However, we don't expect that, as the binding reaction is not at the Helmholtz plane, but it takes place in the diffuse layer. This limits the response due to screening effects[99], as the charges are further away from the surface, and we measure lover change in the potential.

4.1.2 Cu^{2+}-GGH complexation

We suggest that the final complex $GGH-Cu^{2+}$ can be negatively charged due to the release of several protons from the ligand upon Cu^{2+} chelation. The GGH peptide has three amide groups that contribute to the complex formation (Figure 4.2). The nitrogen atom of pyridine in the imidazole ring acts as an anchoring binding site to initiate the Cu^{2+} chelation[101–103]. At neutral to basic pH, the Cu^{2+} chelation process sequentially deprotonates the consecutive peptide nitrogen (secondary amides). The Cu^{2+}-ligand complex can have four different charge states, depending on the pH, which influences the protonation state of the ligand:

$$\begin{gathered}
L + Cu^{2+} \leftrightarrows [Cu^{2+}L]^{+2} \\
L + Cu^{2+} \leftrightarrows [Cu^{2+}L^{-1}]^{+1} + H^{+} \\
L + Cu^{2+} \leftrightarrows [Cu^{2+}L^{-2}] + 2H^{+} \\
L + Cu^{2+} \leftrightarrows [Cu^{2+}L^{-3}]^{-1} + 3H^{+}
\end{gathered}$$

At pH 7 and higher, the ligand is neutral. Upon copper binding the ligand can release up to three protons (secondary amides) and predominantly forms the complex $[Cu^{2+}L^{3-}]^{-1}$[89,90,104,105]. In addition, Cu^{2+} comes in a variety of ionic forms[106], as the Cu^{2+} hydrolysis depends on pH (occurring at pH 5 and higher). Studies identify five hydrolysis products, with $CuOH^{+}$ and $Cu(OH)_2$ (aq.) being prevalent at pH 6 and higher[107]. Cu^{2+} hydrolysis competes with the GGH complexation reaction, affecting the amount of $[Cu^{2+}L^{3-}]^{-1}$ complexes formed and hence, the surface potential.

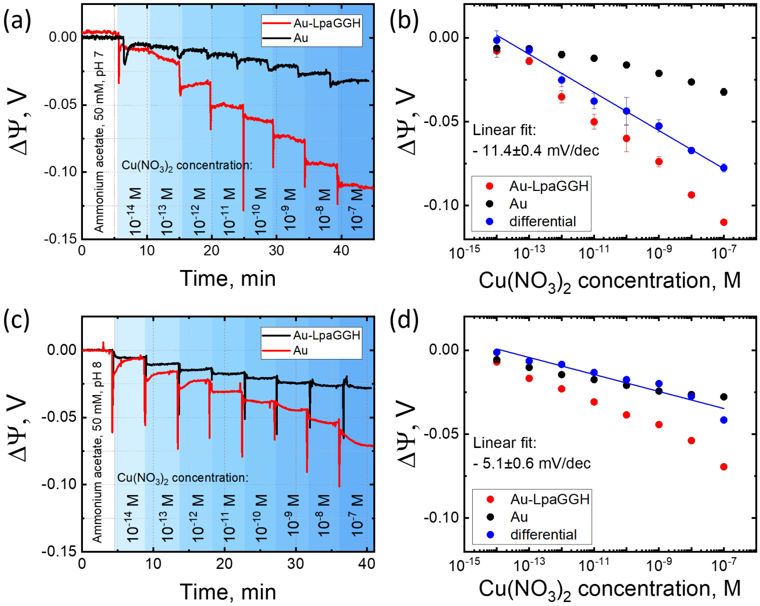

Figure 4.1 Response of the GGH ligand to $Cu(NO_3)_2$ in the concentration range 10 fM - 0.1 µM. Real-time measurements of the surface potential shift $\Delta\Psi$for increasing concentrations of $Cu(NO_3)_2$ in ammonium acetate (50 mM), pH 7 (a) and pH 8 (c). For drift correction, a baseline is subtracted from the measured data, and the measured curves are shifted to zero. (b, d) Differential response at pH 7 and 8, respectively. The reported surface potential values are extracted from "steps" after a 1 min settling time, and the baseline shifted to zero. Figure adapted from reference[100].

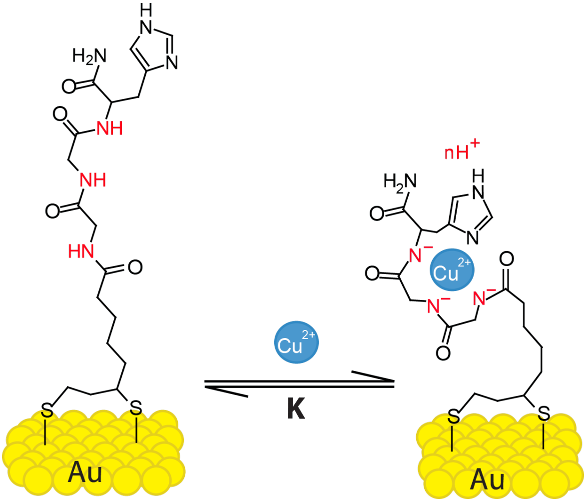

Figure 4.2 Glycine-glycine-histidine ($Gly-Gly-His, GGH$) monolayer on the gold surface and the complexation of Cu^{2+} ions. Secondary amides, carrying different charges depending on the electrolyte's pH, are indicated in red. Figure adapted from reference[100].

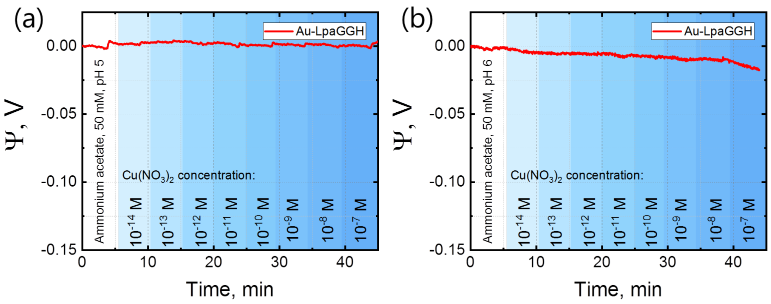

Figure 4.3 Time-dependent measurements for $Cu(NO_3)_2$ in ammonium acetate (50 mM, pH 5, 6). Concentration range: 10 fM - 0.1 µM. Figure adapted from reference[100].

Based on our results, we interpret that upon Cu^{2+} binding to the ligand, secondary amides are deprotonated, and the GGH ligand undergoes a conformational change[80,89,104], bringing an effective negative charge close to the surface (Fig. 1). At pH 7 and slightly higher, we expect the formation of -1 charged complexes $[Cu^{2+}L^{3-}]^{-1}$ resulting in a negative surface potential with increasing $Cu(NO_3)_2$ concentration [42]. In slightly basic conditions (ammonium acetate, pH 8), a secondary amine can already be deprotonated. It results in less or even no net gain in charge, and we observe a smaller response. Furthermore, a higher pH leads to more copper (II) hydroxide formation, leading to a lower concentration of free Cu^{2+} ions in solution that can also lower a response[108,109].

For the passive surface (Au), the surface potential decreases as well. As emphasized above, several copper hydrolysis products coexist at pH 7 and 8, which shows a non-specific interaction with the Au surface of hydroxyl groups on it.

At pH 6 and lower, we observe no response in the $Cu(NO_3)_2$ concentration range between 0.1 fM and 0.1 µM. The acidic environment prevents the deprotonation of the secondary amide groups of the ligand, lowering the probability of the chelation of a cation, thereby leading to a lower affinity to Cu^{2+}. At pH 5 and 6 the active Au-GGH devices in the low concentration range show negligible response (Figure 4.3).

4.1.3 High Cu^{2+} concentration range

In certain conditions, a positive response to Cu^{2+} can be observed. Instead of the expected signal saturation at high $Cu(NO_3)_2$ (from 0.05 mM to 10 mM)

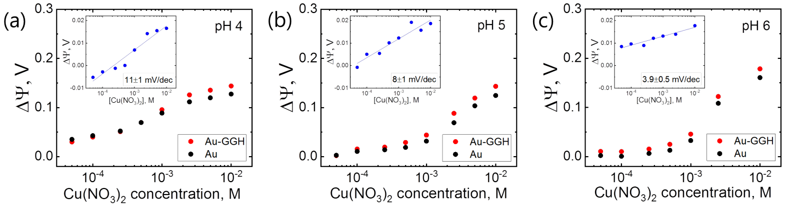

Figure 4.4 Response to Cu^{2+} ions at high concentrations (0.05 - 10 mM) in Titrisol buffer at (a) pH 4 (105 mM, HCl 0.044, NaOH 0.11, $C_6H_8O_7$ 0.056 mol/l), (b) pH 5 (148 mM, NaOH 0.2, $C_6H_8O_7$ 0.096 mol/l), (c) pH 6 (83 mM, NaOH 0.16, $C_6H_8O_7$ 0.06 mol/l), (d) pH 7, ammonium acetate (50 mM). The signal is averaged over all measured nanoribbons (12 active and 12 control). All insets show the differential response. Figure adapted from reference[100].

concentrations, we observe an increase in the surface potential on all surfaces (Au and Au-GGH) even at low pH. Figure 4.4 shows the response to $Cu(NO_3)_2$ at pH 4, 5, 6 (Titrisol buffer). The inset shows a differential response of +11 mV/dec. Figure 4.4b and c show the response at pH 5 and 6 respectively, +8 mV/dec and +3.9 mV/dec. The positive response indicates that in this case, another process is prevalent. We explain this by non-specific adsorption of Cu^{2+} ion to gold at high $Cu(NO_3)_2$ concentrations, leading to a superimposed signal which is higher than that from the specific interaction process. Also, at pH 6 and lower, the histidine can be protonated, contributing to a more positive net charge of Au-GGH compared to the bare Au surface. This process is independent, whether chelation is happening or not, as the effective charge of the $GGH - Cu^{2+}$ complex is either neutral or positively charged (+1 or +2) at low pH. This process leads to a clear increase in the surface potential for Au and Au-GGH and hence, to the positive differential response.

4.1.4 Effect of high background signal

In some cases, a positive response for both the active and the passive wires can lead to overall negative differential response. This might be interpreted as the expected response from the specific interaction between the analyte and the ligand. We however show in Figure 4.5 that this situation can also arise when the response is dominated by non-specific interactions. We observe this behavior at high $Cu(NO_3)_2$ concentrations (0.05 mM - 10 mM) in ammonium acetate, pH 7, where the differential response is indeed negative, -14 mV/dec. In this case, both surfaces, Au (passive) and Au-GGH (active) show however a positive change in surface potential, which indicates that non-specific interactions of Cu^{2+} with the surface dominate the signal from the specific ion binding to the

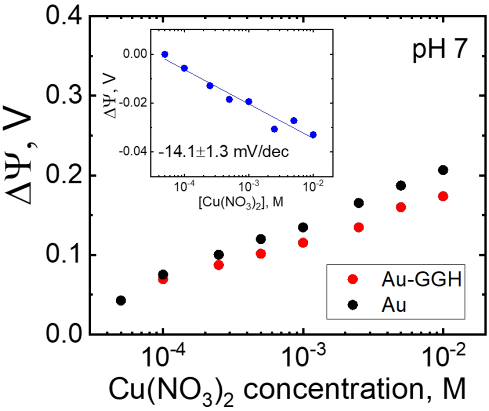

Figure 4.5 Response to Cu^{2+} ions at high concentrations (0.05 - 10 mM) in ammonium acetate (50 mM), pH 7. The signal is averaged over all measured nanoribbons (12 active and 12 control). Inset shows the differential response. Figure adapted from reference[100].

ligand. This again shows the importance of carefully considering all possible contributions to the measured signal.

4.2 Optimal conditions for Cu^{2+} detection with GGH peptide

As we can see from the results, it is essential to determine optimal conditions when working with a peptide-based sensor for metal ions. In figure 4.6 we summarize the different states of ligand and copper depending on the pH of a solution. In the first pH range (I) (figure 4.6) copper mostly exists in ionic form (Cu^{2+})[107]. The nitrogen atom in the imidazole ring of the GGH peptide is protonated, which lowers the ligand's affinity to copper ions. Therefore, not much Cu^{2+} is expected to bind to the ligand in this range. In the second range (II), around neutral pH, nitrogen is deprotonated. Copper in this pH range is not only in its ionic state but also in a hydrolyzed form. In this range, we obtain a maximal sensor response. In the third pH range of the plot (III), almost no copper is in its ionic form. We don't expect chelation in this range since hydrolyzed copper doesn't bind to ligands with the same affinity as free copper ions.

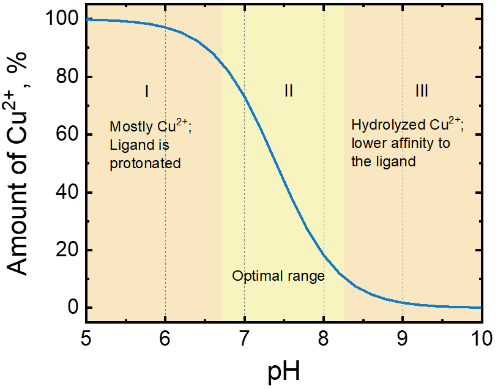

Figure 4.6 Optimal pH range for Cu^{2+} detection. Qualitative schematics of the amount of free Cu^{2+} ions in solution depending on its pH. The plot is divided into three ranges, defining the optimal conditions for Cu-GGH interaction.

4.3 Importance of buffer for detection of Cu^{2+} ions

When working with buffer solutions with metal salts, it is also important to select the correct buffer, as its components may interact with metal ions leading to additional changes in the measured signal. To illustrate this, we show the data in the figure 4.7. We measured the change in the surface potential from active (Au-LpaGGH) and passive (Au) surfaces upon adding different concentrations of $Cu(NO_3)_2$, dissolved in Tris buffer. In both cases, a positive change in the surface potential was observed. We extracted the potential value for every copper concentration (as a potential average of the last 10% of the saturation plateau) after exchanging buffer solution to buffer solution with copper (figure 4.8).

One of the reasons for such high response from the control surface, as discussed previously, is a high impact from non-specific adsorption of Cu^{2+} and copper products from the solution on the gold surface. However, in this case, one more non-specific competing interaction takes place: complexation of Tris and Cu^{2+} ions, as it has been previously reported[110]. Tris is a commonly used buffer in the pH range from 7 to 9. However, it can bind copper ions, therefore preventing them from reaching the receptor, or it can also remove the ion from the receptor.

Figure 4.8 illustrates the extracted values from the figure 4.7. A small

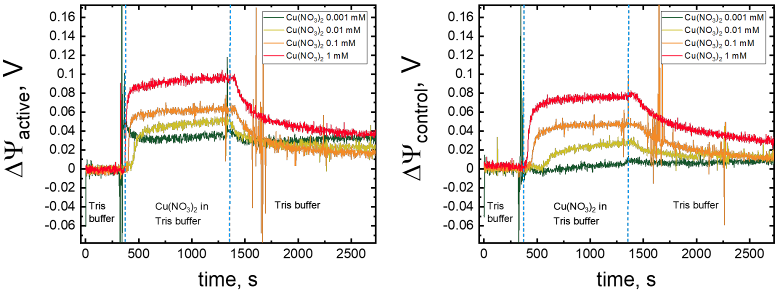

Figure 4.7 Response of the active (functionalized with GGH ligand) and passive (Au) surfaces to $Cu(NO_3)_2$ in the concentration range 0.001 - 1 mM. Time-dependent measurements of the change in the surface potential $\Delta\Psi$with increase of $Cu(NO_3)_2$ concentration in Tris buffer (150 mM), pH 7.4. Baseline shifted to zero.

value of differential response (-4 mV/dec) shows a very minor difference in the response, recorded from active and passive surfaces. It can be attributed to the high effect of non-specific adsorption, which is dominating in this case.

Even though well-buffered systems are often an advantage due to their constant pH throughout the measurement, for the detection of copper ions, it is also important to select a buffer, which does not introduce a competing reaction by forming additional complexes that can affect the device's response.

4.4 Application of site-binding model to Cu-GGH system

In the model, described in subsection 3.1.2, the ligand has one binding site, and the deprotonation, which happens in the case of Cu-GGH complexation, is included in the model. Therefore, we compare the modeled surface potential with the experimental, in the Cu concentration range from 10^{-14} M to 10^{-6} M at pH 5, 6, and 7.

The modeled surface potential is shown in figure 4.9a. Blue, red, and yellow lines highlight the potential change at pH 5, 6, and 7. Additionally, we plot the same curves separately (figure 4.9b) with the experimental data, obtained for the respective pH values. The parameters are the following: $N_{sum} = 9 \times 10^{16} m^{-2}$, $K_L = 10^{-11} M$, $K_1 K_2 K_3 = 10^{-22} M^3$. Compared to the model in subsection 3.1.2, N_{sum} was increased to adjust the change in the surface potential closer to the experimental one.

The model shows a good fit for experimental data obtained at pH 5 and 6

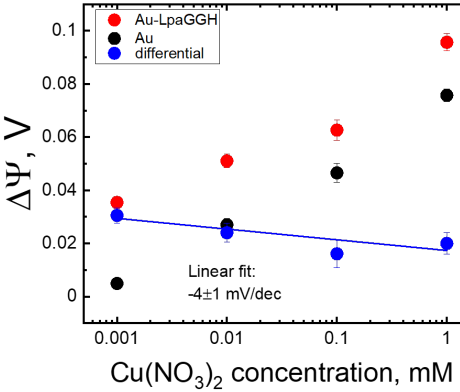

Figure 4.8 Differential response calculated from the measurements in Tris buffer. The reported surface potential values are extracted from the saturation plateau for every copper concentration (last 10% of the "step") shown in the figure 4.7.

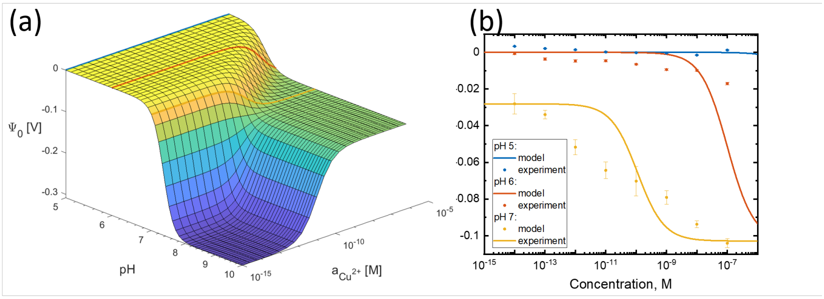

Figure 4.9 Modeled surface potential with highlighted lines at pH 5, 6 and 7 (a) and modeled and experimental data obtained at pH 5, 6 and 7 for GGH-Cu system.

(in most of the concentration range). In the case of pH 7, the overall change in the surface potential is the same, but the slope is steeper. We do not expect an exact fit, as the model was built with several approximations, and we basically model only part of the real system. The similarity however indicates that the site-binding model can be used to predict in some cases the change in the surface potential upon receptor-ion complexation.

4.5 Conclusions to the Cu^{2+} detection with GGH peptide

We have investigated a wide range of $Cu(NO_3)_2$ concentration, from 0.1 pM to 10 mM; the impact of pH and composition of the electrolyte solution on the $GGH - Cu^{2+}$ complexation and the measured results. We found that the optimal range for copper ion detection with GGH peptide is from 0.1 pM to 0.1 μM in ammonium acetate, pH 7. We have also systematically investigated the non-specific effects, which take place at the surface and interfere with a specific signal. ISFET based device has potential for the detection of analytes, however, it must be used in a well-controlled environment, and the system needs case-specific optimization.

The theoretical model, developed in Chapter 3 for receptor with one binding site, can describe the experimental data to some extent.

Having learned the importance of measurement parameters with GGH peptide, we can now extend our approach of using peptides in potentiometric sensors to more complex systems, such as neuropeptide Oxytocin.

5 Oxytocin for detection of Cu^{2+} and Zn^{2+} ions

Contributions: OT peptide was obtained from the group of Prof. Shlomo Yitzchaik, Hebrew University of Jerusalem. Dr. Mathias Wipf and Dr. Sahana Sarkar developed the extended gate-like gold electrode device. Dominik Bachmann developed the electronics. Olena Synhaivska fabricated the devices, performed experiments and analyzed the results presented in this chapter.

Sometimes the reason for developing a certain disease is not caused by the lack of excess of only one metal ion. For example, multiple sclerosis (MS), an inflammatory disease of the central nervous system, is linked to an imbalance of copper and zinc concentration in the human body. The pathophysiology of this disease is not known, but it is considered to have autoimmune nature. It has been found, however, that oxidative stress plays an important role in the pathogenesis of MS[111]. Since oxidative stress is generated by oxygen free radicals, in the formation of which copper is involved[112], monitoring of copper concentration is necessary. Zinc is also an essential element for humans. It is needed for a normal course of an oxidation-reduction reaction, and it is a component of more than 200 enzymes[23]. In addition, zinc is necessary for protection from oxygen-free radicals, synthesis of proteins, nucleic acids, and many other processes[113,114]. In particular, lower serum concentration of Zn and a higher ratio of Cu to Zn in patients with MS shows the relationship between MS and oxidative stress[23]. Therefore, concentration ratio of these metals in blood serum can be a potential biomarker for MS.

Our sensing platform can be very flexible due to the possibility to use a variety of receptor molecules that are selective to analytes of interest and has a high potential for multiple ion sensing. Previously we discussed the challenges of using different receptors for different targets. Optimization of measurements conditions is essential for the best performance of a receptor molecule. Therefore using multiple receptors on one platform in the same conditions (such as pH of electrolyte or target concentration range) is limited. In this chapter, we investigate the opportunity of assembling one receptor molecule that is selective to multiple targets. For Cu^{2+} and Zn^{2+} ion detection, we selected neuropeptide Oxytocin (OT), which binds both ions.

5.1 Response of OT to Cu^{2+} and Zn^{2+} ions

We performed time-dependent measurements to determine the response of OT-functionalized gold electrodes to Cu^{2+} and Zn^{2+} ions. 5 µl of each salt solution of concentration from 0.1 pM to 1 mM was added to the ammonium acetate of 45 µl volume in the measurement well. Figure 5.1 shows the measured response to Cu^{2+} and Zn^{2+} ions in ammonium acetate at pH 7 for active (Au-OT) and control (Au) surfaces. We observed a positive change in the surface potential for both Cu^{2+} and Zn^{2+} ions. In the lower range of metal ion concentrations, from 0.01 pM to 0.1 µM, we observe a higher increase in the surface potential from the functionalized surfaces in case of the Zn^{2+} ions, up to 15 mV, compared to the 9 mV for the Cu^{2+} ions.

From every "step", we extracted the potential value for each concentration, figure 5.1c, d. By subtracting the background response, we obtained differential potential values, shown in the figure 5.2. Linear fit gives a response value. Although the response values are lower compared to the GGH-Cu system (-1.43±0.14, -1.12±0.18, -1.4±0.18 mV/dec for Cu^{2+}; 0.64±0.03, 0.56±0.03 mV/dec for Zn^{2+}), we observe a clear trend: the negative response to Cu^{2+} ions and positive to Zn^{2+} ions. This correlates with the literature data, as the expected complex charge of $OT-Zn$ complex is positive, $[OT-Zn]^{+2}$, and the charge of $OT-Cu$ complex is negative due to the amide deprotonation, $[OT-Cu]^{-1}$[93,95].

Having measured the OT response to Cu^{2+} and Zn^{2+} ions separately, we continued studying the system further, investigating the response in the presence of both ions in the solution as described in the following section.

5.2 OT response to the mixture of Cu^{2+} and Zn^{2+} ions

Figure 5.3 shows time-dependent measurements of Au-OT surfaces to the mixture of Cu^{2+} and Zn^{2+} ions. The concentrations range from 0.1 pM to 1 mM (or from 0.2 pM to 2 mM, for a 1:2 and 2:1 ratio). We observed an increase in the surface potential for all the surfaces. In the range from 0.1 pM to 1 µM, the potential recorded on Au-OT surfaces in the case of 1:2 Cu^{2+} to Zn^{2+} ratio increases up to 40 mV. It is higher than in the case of the 1:1 and 2:1 ratio, where the observed potential increase is up to 30 mV. We attribute a higher change in the surface potential in the case 1:2 ratio to the higher number of $OT-Zn^{2+}$ complexes formed due to the larger amount of Zn^{2+} ions. Since $OT-Zn^{2+}$ complex is positively charged, a higher potential is expected. The difference in the potential change for different concentration ratios is evident from the differential plot (figure 5.3d).

To investigate whether this trend continues with an increase of the concentration of one of the ions, we measured the response to 1:3 and 3:1 concentration

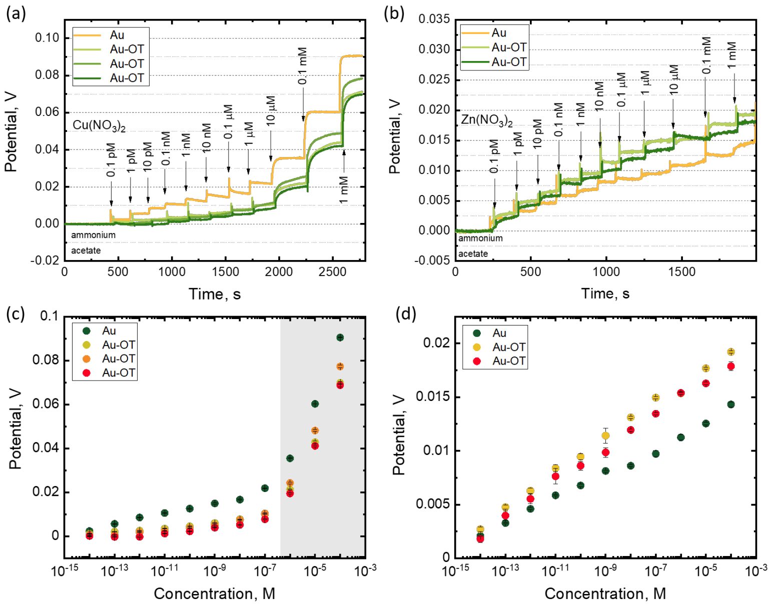

Figure 5.1 Change in the surface potential recorded upon exposure of Au and Au-OT surfaces to (a) $Cu(NO_3)_2$ and (b) $Zn(NO_3)_2$ salt solutions in ammonium acetate (pH 7). Each line represents the measured surface potential on the individual electrode. The measurement starts with ammonium acetate to obtain the baseline. Arrows indicate the addition of 5 µl of the salt solution of a concentrations specified in figure to the well containing 45 µl, therefore the actual concentration in well is one decade lower. (c), (d): extracted surface potential from the "steps" (average value of the last 50% of plateau) for Cu^{2+} and Zn^{2+} ions, respectively.

ratio (figure 5.4). Interestingly, we do not observe a further increase in the surface potential in the case of the 1:3 Cu^{2+} to Zn^{2+} ratio. As we can see in figure 5.4, the trend of background response (Au surfaces) being lower than a response from Au-OT surfaces does not continue. The differential response (figure 5.5 in this case shows a similar trend as in the figure 5.2 when the response of OT to Cu^{2+} and Zn^{2+} was measured separately. This may indicate that with the concentration ratio of 1:3 and 3:1, the effect on the surface potential from the metal ion of higher quantity is dominating the response to the other ion.

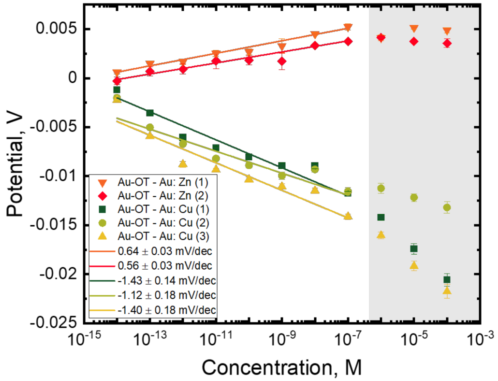

Figure 5.2 Differential response to Cu^{2+} and Zn^{2+} ions was obtained by subtracting the control response of Au surface from the functionalized ones, Au-OT. Linear fit gives the response value specified in the legend. The response to Cu^{2+} is measured in triplicates, the response to Zn^{2+} in duplicates. We fit the range from 10^{-14} to 10^{-7} M. From the concentrations higher the different regime starts, where non-specific interaction of Cu^{2+} ions with a gold surface is prevalent, as can be seen in figure 5.1c.

From the time-dependent measurements (5.4), the difference in the kinetics of the response from Au and Au-OT surfaces is clearly visible: it reaches saturation faster in the case of Au than for Au-OT surfaces. The change in the surface potential measured from Au surfaces we attribute to the non-specific interaction of Cu^{2+} and Zn^{2+} ions with gold. Since the surface is clean, the ions can reach it faster, compared to the OT functionalized surfaces. Also, the specific reactions of the ions with OT contribute to the slower change in the surface potential.

5.3 OT response to Cu^{2+}/Zn^{2+} ions in the presence of high Zn^{2+}/Cu^{2+} concentration

To evaluate the affinity of OT to Cu^{2+} and Zn^{2+} ions in the presence of high concentration of the other ions, we measured the response to $Cu(NO_3)_2$ ions in the presence of 10^{-8} M of $Zn(NO_3)_2$, and vise versa. The obtained results are shown in figure 5.6.

Interestingly, in this case, we observe a negative differential response to Zn^{2+}

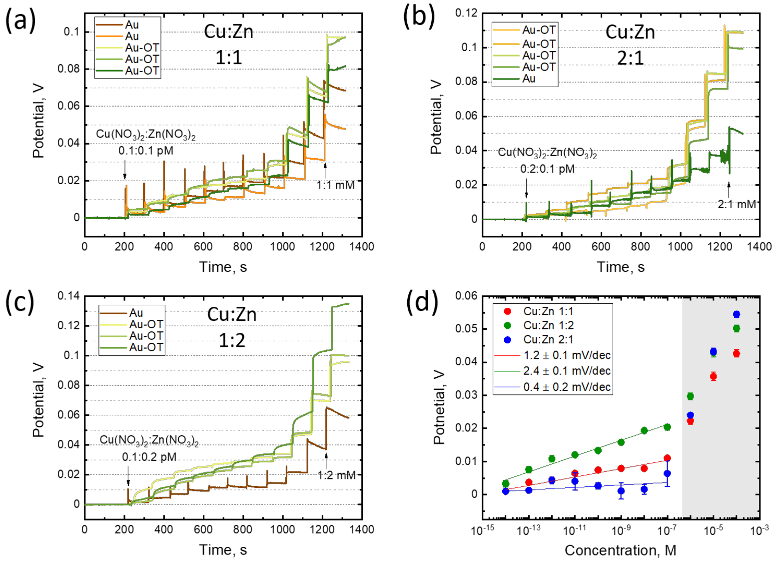

Figure 5.3 Change in the surface potential recorded upon exposure of Au and Au-OT surfaces to the mixture of $Cu(NO_3)_2$ and $Zn(NO_3)_2$ salt solutions in 1:1 ratio (a), 2:1 (b), 1:2 (c) in ammonium acetate (pH 7). Each line represents the measured surface potential on the individual electrode. The measurement starts in ammonium acetate to obtain the baseline. Each "step" indicates the addition of the metal salt solution of a higher concentration. (d) Differential response for the 1:1, 2:1, 1:2 concentration ratios.

ions and positive for Cu^{2+} ions, which was not the case when we measured the response to them separately 5.2. Now, after adding the high concentration of copper as a first step (5.6a), a certain amount of OT-Cu complexes is created. With the addition of $Zn(NO_3)_2$, starting from low concentration, 10^{-14} M, the amount of positive OT-Zn complexes is very low compared to OT-Cu. Therefore the measured potential at the surface is lower than for Zn^{2+} ions only. A similar explanation can be applied to the case in 5.6b, where the response from Au-OT surfaces is higher than from Au, causing, therefore, differential response to be positive.

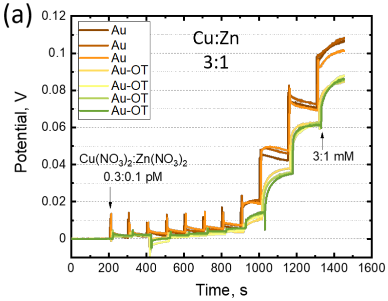

Figure 5.4 Change in the surface potential recorded upon exposure of Au and Au-OT surfaces to the mixture of $Cu(NO_3)_2$ and $Zn(NO_3)_2$ salt solutions in 3:1 (a) and 1:3 (b) ratio in ammonium acetate (pH 7). Each line represents the measured surface potential on the individual electrode. The measurement starts in the ammonium acetate to obtain the baseline. Each "step" indicates the addition of the metal salt solution of a higher concentration.

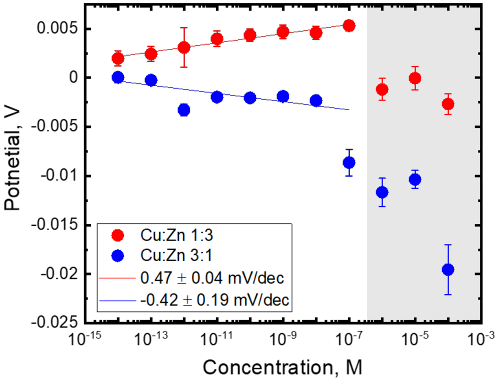

Figure 5.5 Differential surface potential obtained for OT response to Cu^{2+} and Zn^{2+} at the concentration ratio of 1:3 and 3:1.

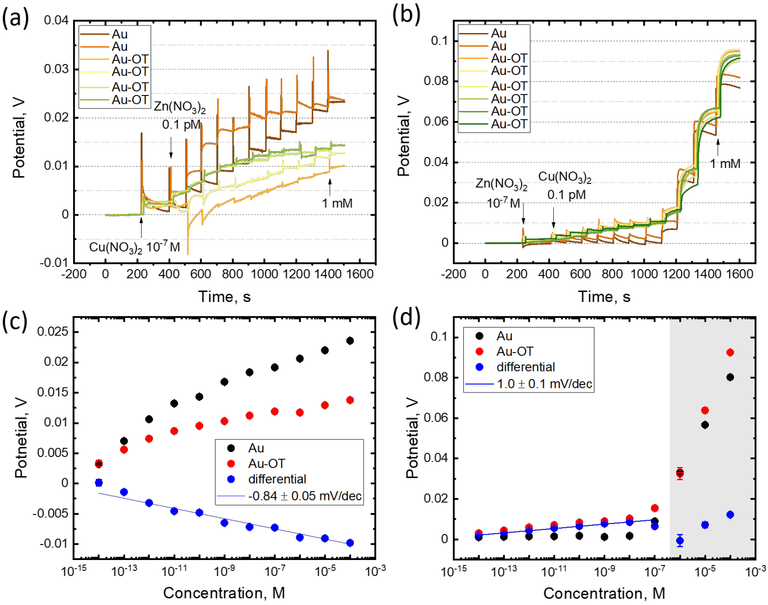

Figure 5.6 Change in the surface potential recorded from Au and Au-OT surfaces: (a) after adding high concentration (10^{-7} M) of $Cu(NO_3)_2$ followed by titration of $Zn(NO_3)_2$; (b) addition of 10^{-7} M of $Zn(NO_3)_2$ followed by titration of $Cu(NO_3)_2$. The measurement starts in the ammonium acetate first to obtain the baseline. Arrows indicate the addition of the initial high concentration of metal salt and the first and the last addition of the other salt. To keep the concentration of the first added salt constant throughout the measurement, every solution with the second salt contained also the first one, to compensate for the amount extracted from well. (b), (d) Extracted potential values from each "step" and calculated differential response to $Zn(NO_3)_2$ and $Cu(NO_3)_2$, respectively.

5.4 Application of site-binding model to $OT - Cu^{2+}/Zn^{2+}$ system

Theoretical model, developed in section 3.3.2, describes receptor, that can bind two ions, and the complexes formed are 1- and 2+ charged. The model includes also deprotonation of the receptor's binding groups. We can therefore assume that this model could describe our OT-Cu/Zn system. We plot the modeled surface potential (5.7a), highlighting the case of Ψ_0 change with an increase of Zn^{2+} concentration when Cu^{2+} is at 10^{-8} M, and vice versa.

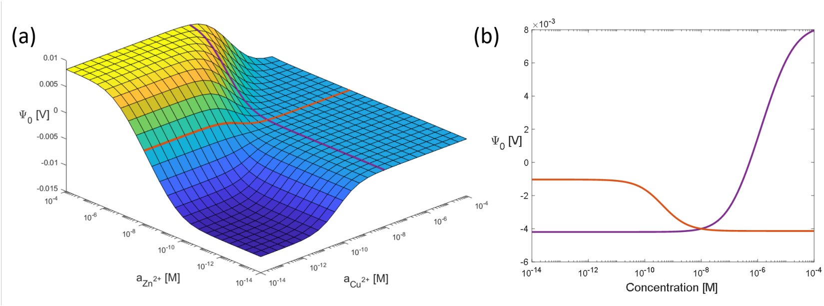

Figure 5.7 Modeled surface potential in the case of receptor, selective to two ions, Cu^{2+} and Zn^{2+}. (a) Surface potential plotted versus Cu^{2+} and Zn^{2+} concentration. Red and purple lines on the surface highlight the experimental conditions, the response to one ion measured in the presence of constant concentration of the other ion (10^{-8} M). (b) Surface potential versus concentration of Cu^{2+}/Zn^{2+}, extracted from the 3D plot for clarity.

In this case the modeled response does not correspond exactly to the obtained data (figure 5.6). In the model differential response shows the opposite trend: positive for OT-Cu complexation and negative for OT-Zn. Considering the sign of the response, the modeled one is more similar to the data obtained for Cu^{2+} and Zn^{2+} detection only (figure 5.2).

Also, in the model we assume that all the ions at certain concentration bind to OT on the surface. In reality, however, the effective concentration is lower, which could also explain the difference in the modeled and experimental data.

5.5 Surface passivation with thiols

Metal ions interact with a gold surface, contributing to the measured signal (due to additional contribution to the net surface charge) and therefore interfering with the specific analyte response. We investigated the possibility of surface passivation of the gate surfaces, to minimize nonspecific adsorption. For this purpose we selected octane- and dodecanethiol ($C_8H_{18}S$ and $C_{12}H_{26}S$, respectively), which form densely packed monolayers on gold surfaces[115], as shown in figure 5.8.

Figure 5.9 shows the measured response from Au and Au-thiol surfaces to $Cu(NO_3)_2$ salt solutions in the concentration range from 0.1 pM to 10 µM. For the two highest concentrations, we observe a significant increase in the

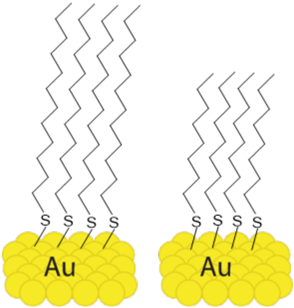

Figure 5.8 Schematic of the gold surfaces, passivated with the monolayers of dodecane- and octanethiol.

surface potential for Au electrodes, whereas for the electrodes, functionalized with octane- and dodecanethiols, the measured signal returns to the baseline, indicating effective surface passivation.

As a next step, we functionalized the surface with OT and thiols in a two-step procedure: first, the OT solution in Milli-Q water was deposited on the gold surface for a minimum of 12 hours; then the OT solution was removed, followed by the Milli-Q water rinse, and thiol solution was applied. The surfaces are schematically shown in figures 5.10a,b.

The change in the surface potential for one Au-OT-octanethiol surface occurred upon adding 0.1 mM Cu^{2+} concentration and for one Au-OT-dodecanethiol surface (10 μM and 0.1 mM). This change, however, as is was observed at high concentrations, could also be due to "breakthrough" cases of Cu^{2+} ions reaching the surface, with a typically observed increase in the surface potential. In addition, the potential change after adding these Cu^{2+} concentrations is relatively high (in the range of 100-200 mV), which is usually observed for the non-specific adsorption of metal ions on Au surfaces. Therefore, the data in figures 5.10c,d suggest that despite surface passivation was achieved for most of the surfaces, we can not conclude that the specific response was observed.

The reason for not observing the specific OT-Cu/Zn response can be due to the hydrophobic effect of the thiols used. Since metal ions in the solution are surrounded by water molecules, it is possible they cannot approach OT close enough for binding. Therefore shorter hydrophilic molecules, such as 6-mercapto-1-hexanol, could be more suitable for passivation with further ion sensing application (figure 5.11).

In addition, the surface passivation procedure can be improved. Since thiol molecules have a stronger affinity to gold than OT, it is likely that OT, assembled in a first step, was removed from the surface by thiols, deposited in

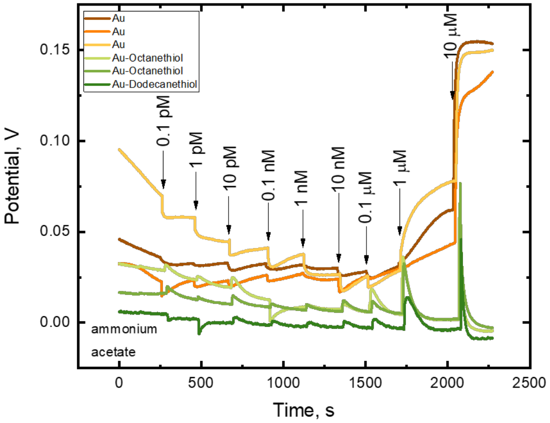

Figure 5.9 Change in the surface potential upon addition of $Cu(NO_3)_2$ salt solutions in ammonium acetate (50 mM, pH 7) measured on the electrodes, gold (Au) and functionalized with octane- and dodecanethiols. Each line shows the measured surface potential on the individual electrodes. The measurement starts in the ammonium acetate first to obtain the baseline. Arrows indicate the time of adding the $Cu(NO_3)_2$ solutions of higher concentration.

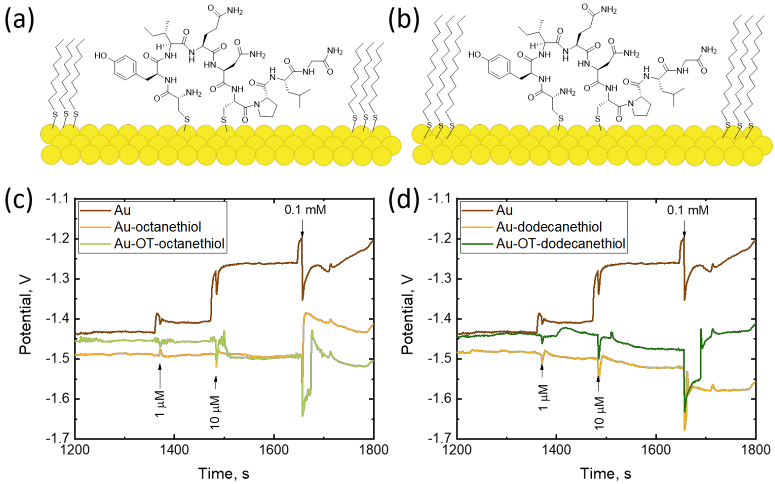

Figure 5.10 Surface potential recorded from the Au, Au-thiol and Au-OT-thiol surfaces. We show the data in the concentration range from 0.1 μM to 0.1 mM, where the change in the surface potential was observed.

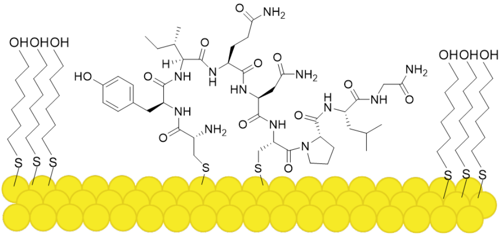

Figure 5.11 Schematic of the gold surface, functionalized with mercaptohexanol and OT.

a second step. Therefore, preparing the solution of equal concentration of OT and thiols and depositing this mixture at once could be a promising approach.

5.6 Conclusions to the Cu^{2+} and Zn^{2+} detection with Oxytocin

We have investigated the response of OT in the range of $Cu(NO_3)_2$ and $Zn(NO_3)_2$ concentrations from 0.01 fM to 0.1 mM. We can differentiate between the response of our OT-functionalized device to the solutions with Cu^{2+} and Zn^{2+} ions with concentration ratio 1:1, 2:1, and 1:2, as in the latter case, there are enough positively charged OT-Zn complexes formed to compensate contribution from the negative change of OT-Cu complexes. When we increased ratio further, to 1:3 and 3:1, we found that the sensor's response is more similar to the case when we studied the OT response to Cu^{2+} and Zn^{2+} ions separately, suggesting the dominating effect of ion at higher concentration.

Since in all the experiments we observe a background signal, we investigated the opportunity of passivating the surface to suppress the background response. We assembled octane- and dodecanethiols on the surface, and as a result, non-specific Cu^{2+} ion adsorption was prevented. Specific OT-Cu response was, however, not confirmed. We describe possible reasons and suggest using another molecule, 6-mercapto-1-hexanol, and modifying the passivation procedure. Implementing such an approach could potentially solve the issue of non-specific adsorption in potentiometric sensors.

6 Physiochemical profile of the aggregation pathway of Parkinson's alpha-synuclein protein

Contributions: αSyn samples were prepared by Olena Synhaivska from the αSyn in lyophilized state, synthesized by Dr. Silvia Campioni. AFM measurements and analysis were conducted by Dr. Peter Nirmalraj. MD simulations were done by Dr. Shayon Bhattacharya and Prof. Damien Thompson from University of Limerick, Ireland. Olena Synhaivska conducted Raman spectroscopy measurements and data analysis, and integrated all the results together for an overview analysis of αSyn aggregation pathway presented in this chapter.

6.1 Introduction

Neurodegenerative diseases, such as Parkinson's (PD) and Alzheimer's (AD) affects millions of people worldwide and is a serious global health crisis. The incidence of PD cases is the fastest to increase[116]. Currently, it is estimated that 50 million people live with AD and 10 million people with PD[117], and with the aging of the population, these numbers are predicted to rise[116?], creating new challenges for future generations.

Although massive efforts are currently underway to decode the genetic and environmental triggers that could lead to AD and PD, underlying molecular level pathogenesis remains to be fully understood[118,119]. However, there is a definite consensus that the processes of misfolding and aggregation of proteins, alpha-synuclein (αSyn) and amyloid-beta, occur in the case of PD and AD, respectively[2,3]. Aggregation of tau proteins causes another entire group of disorders, called tauopathies[4] and tau peptides have also been implicated in the pathology of AD.

Early-stage diagnosis of the above-mentioned pathologies is challenging, as the symptoms are mild and can also occur during normal aging[118]. Currently, the clinical diagnosis possible at stages when symptoms become visible, which is already an indication of later stages of the disease. Therefore, understanding the exact reasons for their development at the molecular level will shed light

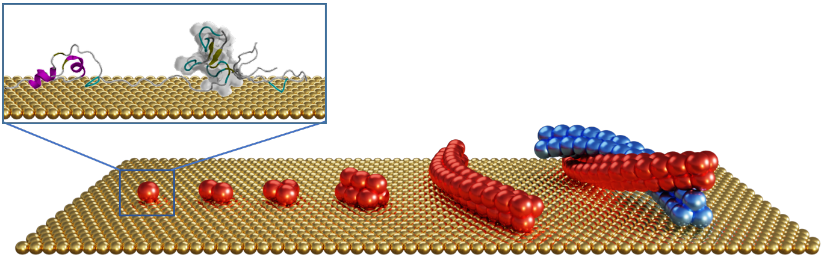

Figure 6.1 Schematic of the aggregation of aSyn from monomer, oligomers, protofibrils, to mature and elongated fibrils.

on the pathogenesis of these diseases and will also help with early diagnosis, prevention, and treatment[120].

Over the last twenty years of research on Parkinson's disease, it is now widely accepted that protein αSyn is the main regulator of PD pathology[121,122]. It is a natively disordered protein, consisting of 140 amino acids[123] and has three domains: N-terminal (lipid-binding α-helix), amyloid-binding central domain (NAC), and C-terminal (acidic tail)[5]. This protein has a tendency to gradually aggregate, leading to the formation of fibrillar aggregates, as schematically shown in figure 6.1. One of the pathological hallmarks of PD is the presence of intraneuronal αSyn aggregates in Lewy bodies[124]. Understanding the reasons that cause αSyn to aggregate will allow to shed a light on the pathogenesis of PD and ultimately to find a cure. Therefore, studying its aggregation is necessary.

αSyn aggregation can be reproduced in laboratory conditions, by incubating the protein solution with mechanical agitation at higher temperatures. Samples can be prepared at different time points for the analysis and monitoring of an aggregation process. Various techniques have been used for the characterization of αSyn aggregates. The most commonly used methods are infrared spectroscopy, optical fluorescent microscopy[125], electrospray-ionisation mass spectrometry[2,122], Raman spectroscopy[4], nuclear magnetic resonance (NMR) and electron paramagnetic resonance (EPR) spectroscopy[126]. In addition to experimental studies, theoretical modeling is also an active research field. Molecular dynamics (MD) is yet another powerful method for understanding protein aggregation in experimentally inaccessible timescales and to gain a deeper insight into the dynamics and energetics of the folding and aggregation process[127].

In this study, we combine AFM and Raman spectroscopy to clarify the size, shape, morphology, and spectrochemical signature of the aggregates formed along the αSyn assembly pathway on a clean gold surface. To gain a deeper understanding of the αSyn interactions on gold we rely on molecular dynamics simulations in collaboration with simulation experts at the University of Limerick, Ireland. The combination of these methods allows complex characterization of protein aggregates under both standard laboratory conditions at experimentally inaccessible time scales (10-100 ns). AFM allows visualizing proteins with a high resolution in their different aggregation stages in the air as well as at the solid-liquid interface. Raman spectroscopy provides information on the protein chemical structure, and the information on its aggregation state can also be extracted, as it is reflected in the amide I (1640-1690 cm^{-1}) and amide III region (1230-1300 cm^{-1}) due to the higher content of the β-sheet in the aggregated state[128,129].

Therefore, combining these techniques allows fully characterize the αSyn aggregates by correlating their morphology and chemical structure. Importantly, these methods are label-free.

Effect of metal ions

Genetic reason for the development of PD is attributed to 20% cases. The other causes of the onset of PD are aging and environmental factors, such as exposure to heavy metal ions and pesticides, as well as brain injuries[130,131]. For example, studies have shown that people exposed to high doses of heavy metals from the environment for a long time, such as miners[132], are more likely to develop PD.

Therefore, a substantial amount of research has been done on the investigation of how these metal ions can impact protein aggregation[5,122]. Copper, calcium, and manganese ions are considered to be the most cytotoxic[133], and can cause early onset of aggregation and affect its rate. A recent study has confirmed the presence of copper and iron in the human brain tissue[9]. With high-resolution (20 nm) synchrotron-based scanning transmission x-ray microscopy (STXM) presence and spatial distribution of copper and iron were determined in human amyloid plaques. In addition, magnetic properties of different regions of the sample were correlated to their chemical structure via x-ray magnetic circular dichroism (XMCD) effect. The combination of these techniques allowed the detection of elemental metallic copper and iron. Cu^{2+} has been also detected at elevated concentrations in cerebrospinal fluid (CSF) from patients with PD[134].

In addition to the ongoing efforts, it would also be beneficial to address the issue of metal ion interactions with αSyn at a single particle level under *in vitro* conditions, as this could also advance our current understanding of the metal ion-αSyn interactions.

In this project, we aim to study the aggregation pathway of αSyn with AFM, Raman spectroscopy, and MD simulations. As copper is one of the key ions that interact with αSyn[7], we investigate its aggregation pathway with and without the presence of copper ions.

6.2 αSyn sample preparation and measurement techniques

In this section, we provide the details on the preparation of αSyn samples and the measurement techniques, AFM and Raman spectroscopy.

6.2.1 αSyn sample preparation

αSyn solutions were prepared by dissolving lyophilized protein (30 mg/ml when dissolved in 2 mL) in PBS buffer at pH 7.4. This led to the decrease of pH, which was then adjusted to 7.4 by adding sodium hydroxide (NaOH) of 1 M concentration (25-30 µl). After the filter membrane of Amicon Ultra-4 Centrifugal Filter Unit (NMWL 100 kDa) was hydrated by running centrifuge three times with 4 ml of PBS buffer (3200 g, 5 minutes), αSyn solution was centrifuged for 30 minutes to filter out large αSyn chunks that were not dissolved. Then 200 µl volume (or 10% of solution volume) of PBS was added to the filter and mixed using a pipette to extract remaining aSyn from the bottom part of the filter, followed by centrifugation for 5 minutes.

Afterwards the final concentration of αSyn (ϵ_{280}=5960 $M^{-1}cm^{-1}$) was measured with spectrophotometer Implen Nanophotometer NP80 UV/Vis. Afterward, the solution was diluted with PBS buffer to 300 µM aSyn concentration. V-shaped 1.5 ml Protein LoBind tubes were filled with 500 µl αSyn solution and incubated in Eppendorf ThermoMixer C at 37 °C for 7 days. To investigate the effect of Cu^{2+} ions on the αSyn aggregation rate, its solution was added to the aliquot with αSyn before the incubation. For each experiment, three aliquots of 300 µM αSyn concentration were prepared for comparison: not incubated, incubated without, and with Cu^{2+} ions. For AFM and Raman spectroscopy measurements samples were prepared by drop-casting 50 µl of aSyn solution on different substrates (gold/mica, mica, Silicon). Samples were dried in ambient conditions.

Preparation of Cu^{2+} ion solutions

Cu^{2+} ion solution of concentration 10 µM was prepared by dissolving copper(II) chloride in PBS buffer, pH 7.4 (Merck Millipore). Then 50 µl volume of prepared copper chloride solution was added to the aliquot with 500 µl of αSyn, leading to the final Cu^{2+} ion concentration of 1 µM.

6.2.2 AFM

Liquid-based atomic force microscopy was performed using a Multimode 8 AFM (Bruker) equipped with a flow cell. For the AFM probe, a SCOUT 70 HAR silicon AFM tip with a high aspect ratio was used in tapping mode (gold reflective backside coating, force constant 2 N/m, resonant frequency: 70 kHz, cone angle of <15°over the final 1 µm of the tip apex, NuNano). Before

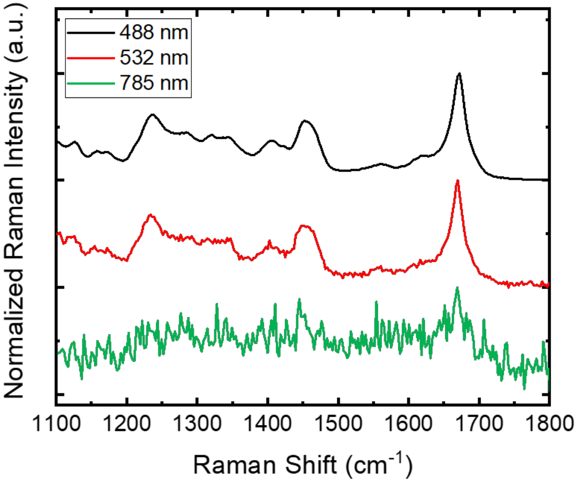

Figure 6.2 Raman signal obtained on αSyn samples with three laser wavelengths: 488 nm, 532 nm and 785 nm.

inserting the AFM probe in the holder, the AFM tip was cleaned by rinsing in acetone for 30 s followed by rinsing in isopropanol for ∼1 min followed by blow-drying with compressed air. After mounting the AFM probe in the tip holder, 5 µL volume of alpha-synuclein solution was injected through the inlet port in the liquid-cell holder on atomically flat Au(111). Before deposition of the αSyn solution, the Au(111) on mica (commercially obtained from Phasis, Inc) samples were thoroughly cleaned (acetone rinsing followed isopropyl alcohol rinsing and blow-drying with N_2) and the surface quality was checked using an AFM. After ∼2 min the liquid cell was gently flushed with pure water and the AFM was immersed and tuned in the pure water medium to generate the AFM images shown in the main manuscript.

6.2.3 Raman spectroscopy

Raman spectra were obtained using WITec Alpha 300 R confocal Raman microscope. After acquiring spectra with three different lasers (wavelength 488 nm, 532 nm, 785 nm) as shown in the figure 6.2, we concluded that 532 nm laser gives the highest resolution and therefore is the most suitable for our application. For all the measurements we used the spectrometer grating of 600 g/mm and Zeiss 100× objective, NA = 0.9. Raman maps were acquired on typically 15 µm by 15 µm surface, with 1 µm steps, 1 s integration time, (225

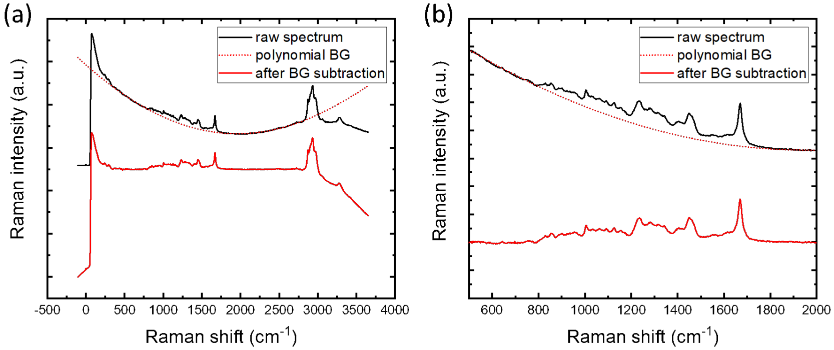

Figure 6.3 Background (BG) subtraction from raw aSyn spectra obtained on the Au/mica substrate. a) Full spectrum (averaged over the surface area of 15 by 15 µm, 225 spectra in total) and b) close-up to the region of interest before and after polynomial subtraction. We used a third-order polynomial.

spectra in total). Time series were acquired on the same spot (normally 60 spectra, 1 s integration time).

Laser power was adjusted for different substrates: 40 mW for mica, 20 mW for silicon, 10 mW for gold/mica. For every area scan, one average spectrum was obtained. To obtain representative spectra of the measured sample, average spectra of multiple areas were normalized and then averaged. For the spectra obtained on Au/mica surface, we did a background (BG) subtraction, as shown in figure 6.3.

6.3 Results and Discussion

In this section, we present and discuss AFM and Raman spectroscopy data, obtained on αSyn samples, prepared with different incubation times, from 1 to 10 days. Such an approach allows studying the different phases of αSyn aggregation, from embryonic (monomers and small oligomers) to lag (large oligomers and short fibrils), elongation (isolated long fibrils), and saturation (densely packed layered fibrils).

6.3.1 AFM based analysis of αSyn aggregation pathway at gold water interface

Figure 6.4 shows AFM data on the early stages of αSyn aggregation, with incubation for 1, 2, 3, and 4 days.

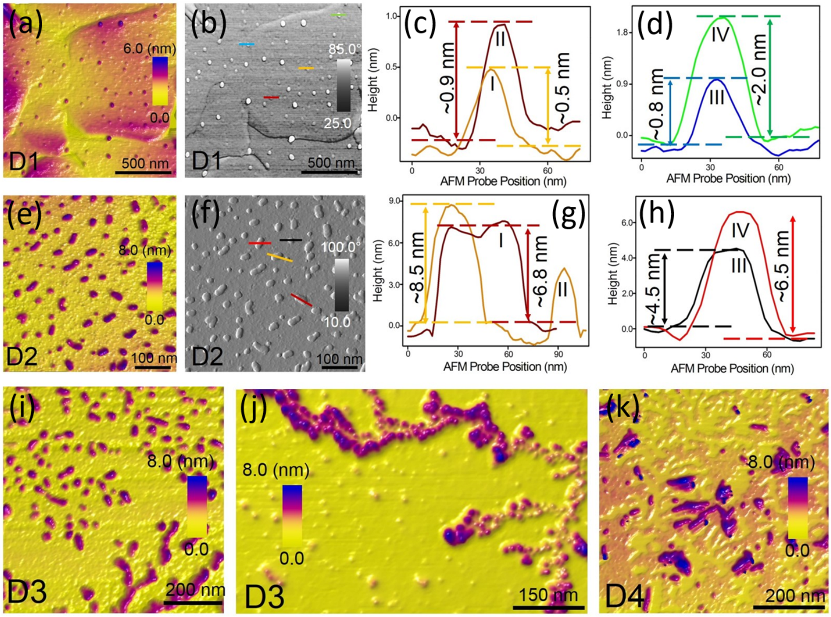

Figure 6.4 Embryonic and lag phase of αSyn aggregates resolved on gold. Large-area AFM topographic (a) and phase-contrast image (b) of αSyn peptides in the form of monomers and small oligomers adsorbed on the terraces of ultra-flat gold (surface roughness of bare gold regions: 0.2 nm). The AFM data shown in panels a, f, k, m were recorded after incubating the αSyn solution for 1, 2, 3, and 4 days at 37° C under mechanical agitation, respectively, as labeled D1-D4. (c-d) Individual cross-sectional profiles were measured across the particles visible from the AFM topography (panel a) and indicated by the respective colored lines in panel b. (e) and (f) AFM height and phase-contrast image of major αSyn oligomer populations on Au (111). (g) and (h) Cross-sectional profiles measured along the color-coded lines across the oligomeric aggregates as marked in panel f. (i-k) High-resolution AFM height maps of oligomeric and dendritic αSyn structures observed on Au (111) after three days of incubation.

We can see an increase in the length of different aggregated structures formed with longer incubation time, from monomers to oligomers and protofibrils. Figures 6.4c-h show the extracted cross-sectional profiles from the obtained topography images. After one day of incubation, only monomers and small oligomers are observed on the surface. After two days, there are mostly larger oligomers. The particle height increases from ∼1 nm to ∼6.5 nm. After three days of incubation, large oligomers and dendritic structures are present on the surface. After four days of incubation (6.4k), we observe a formation of small protofibrils, on top of the layer of αSyn oligomeric dendritic structure.

After 5 days of incubation, fibrils of length in the submicromolar range (from 260 nm to 850 nm) were observed, as shown in figure 6.5a, b, d. Measurements on the αSyn fibrils deposited on the gold surface were conducted in three different conditions: when αSyn was in the dry state (trial 1), in clean grade water (trial 2), and in PBS buffer (trial 3). Trial 1 was performed when αSyn in buffer solution was drop casted on gold and then gently rinsed with clean water and air-dried for imaging. Trial 2 was performed in separately prepared αSyn solution of identical concentration as trial 1 and then deposited on gold, rinsed, and retained in clean water. Trial 3 was performed in a separate study with identical αSyn solution concentration as trial 1 and trial 2, but in the PBS buffer.

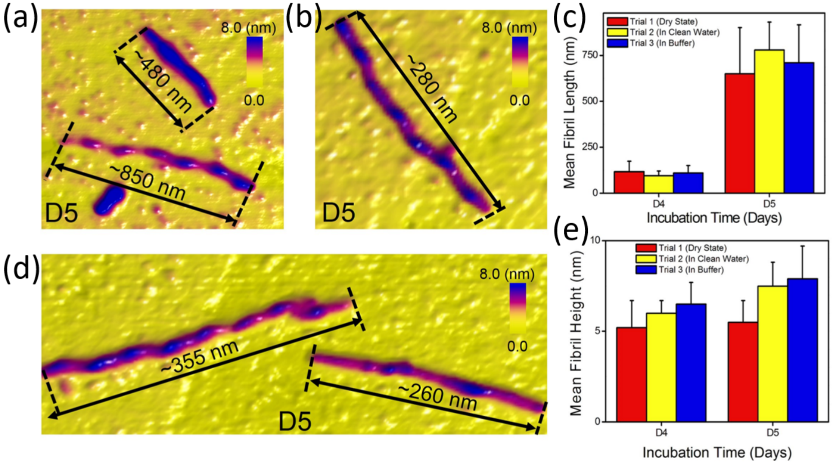

Figure 6.5 Quantifying the elongation phase of αSyn from AFM topography images. (a-c) High-resolution AFM height images of mainly protofibrillar aggregates with typical nodular morphology were observed on Au(111). (d) Statistical analysis of the mean length of fibrils resolved on day 4 (D4) and day 5 (D5) of αSyn solution incubation. A significant increase in fibril length was detected between day 4 and day 5 of αSyn solution incubation for all three trials. (e) Statistical analysis of mean fibril height calculated from the AFM images acquired on day 4 and day 5 of αSyn solution incubation based on three separate trials.

Histograms (figure 6.5c, e) show the mean length and the mean height of the observed fibrils in all three experimental trials after four and five days of incubation. The length increases from ~125 nm to ~750 nm. In the fibril height, however, only minor change was detected on day 5 compared to fibril height measured on day 4 of αSyn solution incubation.

From day 6 to day 10 we observe evolution in the spatial organization of fibrils from sparse to dense network (6.6). After 10 days of incubation, phase-contrast images show the close-packed and layered arrangement of αSyn mature fibrils.

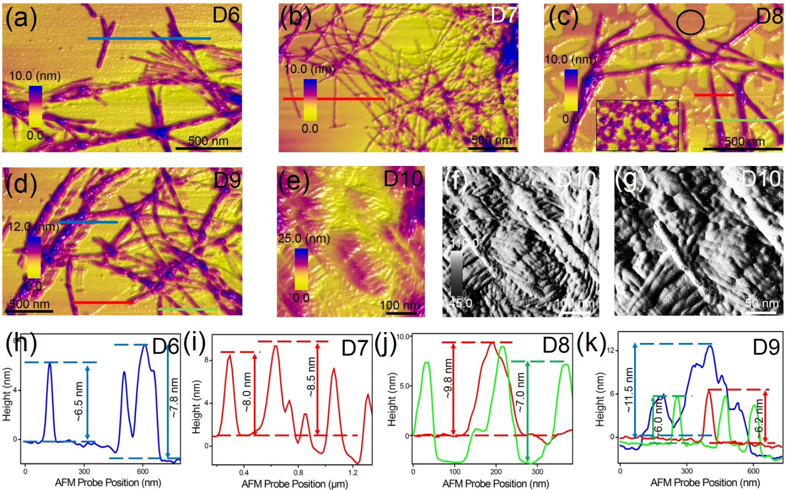

Figure 6.6 Stepwise mapping of densification in the saturation phase of α-synuclein. High-resolution AFM topographs revealing the evolution in the spatial organization of fibrils from a sparse to dense network on gold after αSyn solution was incubated for 6 (a), 7(b), 8(c), 9(d), and 10(e) days. The AFM data shown in panel a-g were recorded in a clean water environment. The phase-contrast images (f-g) reveal the close-packed and layered arrangement of αSyn mature fibrils on gold recorded on day 10 of the aggregation pathway of αSyn. (h-k) Height profiles extracted along the respective color-coded lines indicated in panels a, b, c, and d showing the differences in fibril height with respect to the underlying gold surface.

Despite rinsing the buffer solution with clean water and imaging in a water medium, a residual buffer salt layer is present in certain regions of the gold surface (bottom inset image in figure 6.6c) on which the fibrillar network is adsorbed. The height profiles of fibrils after 6, 7, 8, and 9 days of incubation

(6.6h-k) are calculated by measuring the difference in height between the maximum peak position and underlying gold rather than calculating the difference in height between the buffer salt layer and fibril maximum height. The height profiles are in the range from ∼6.5 to ∼11.5 nm, however, the fibrils of ∼7 nm height are the most common.

6.3.2 Molecular dynamics simulations to decipher monomer, oligomers of αSyn at the gold water interface

Molecular dynamics simulations were performed by Prof. Damien Thompson and Dr. Shayon Bhattacharya from the University of Limerick, Ireland. Figure 6.7a-d shows simulated αSyn structures adsorbed on gold: monomer, dimer, trimer, hexamer.

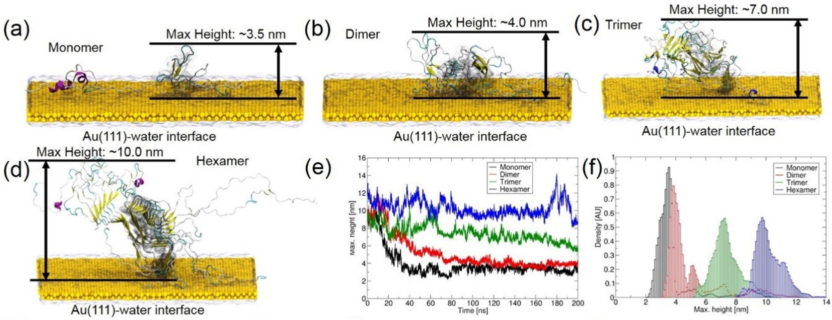

Figure 6.7 Heights, structural deviation, size, and shape of αSyn assemblies on Au(111)-water interface from molecular dynamics (MD) simulations. (a–d) Representative structures of monomer, dimer, trimer, and hexamer showing their average maximum height on Au(111) surface during 200 ns dynamics. (e) Monomer and oligomers maximum heights as a function of simulation time and (f) their density of distribution on the surface of Au(111).

On the gold surface, the monomer from an initial protofibrillar conformation collapses within the first 20 ns, as shown in figure 6.7e, the height profile as a function of time. αSyn dimer also collapses, but to a lesser extent than monomer. The height of the trimer and hexamer does not change upon contact with a surface. From the MD simulations, the obtained height distribution is shown in figure 6.7f. The peak values are ∼3.5 nm, ∼4.0 nm, ∼7.0 nm, ∼10.0 nm for monomer, dimer, trimer, and hexamer, respectively. The cross-sections, shown in figure 6.4 and histograms in figure 6.5 suggest the aggregate height of 6-7 nm to be the most frequently appearing. The aggregate of such height resembles a trimer, predicted by the simulations.

Figure 6.8 shows the height values, extracted from AFM measurements on the αSyn samples in a dry state, in clean water, and in buffer over a span of 10 days. Protofibrillar aggregates were first detected on the third day during all the trials (marked by the black dashed box in figure 6.8). Onset of mature fibrillar aggregates was observed only on the fifth day of αSyn solution incubation during trial 1 and 2 (indicated by the blue dashed box in panel b) and was detected on the sixth day during trial 3 (indicated by the red dashed box in panel b), which was conducted in buffer solution environment.

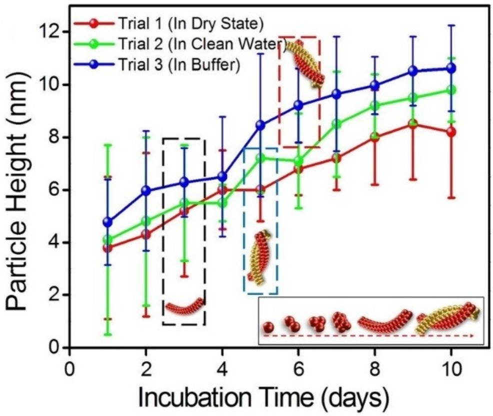

Figure 6.8 The increase in height values of the full spectrum of particles from monomers to fibrils versus αSyn solution incubation time over a span of 10 days. The red, green, and blue plots correspond to particle heights measured separately in three different trials in a dry state, clean water, and in buffer medium, respectively, with mean and error bars obtained from 150 measurements recorded each day of each trial.

6.3.3 Raman spectroscopy based chemical analysis of αSyn aggregates

Raman spectroscopy is a powerful tool for identifying the αSyn aggregation state[128,129,135]. Analysis of Amide I and Amide III bands provides information on changes in aSyn secondary structure upon its aggregation[128,129] Amide II band is composed of C-N stretching and N-H bending, is considered a weak vibration, and cannot be observed without resonant excitation[136,137].

Figure 6.9 shows Raman spectra of αSyn in different aggregations states, from the embryonic phase to lag phase, elongation phase, and saturation phase.

We first normalize the obtained spectra to Phe band (1003 cm^{-1}). This band is not sensitive to the conformational changes and therefore is not affected by the aggregation of aSyn[128]. The intensity of the Amide I band, with a peak maximum at 1670 cm^{-1}, increases with aggregation from embryonic to elongation phase, indicating an increase in β-sheet content.

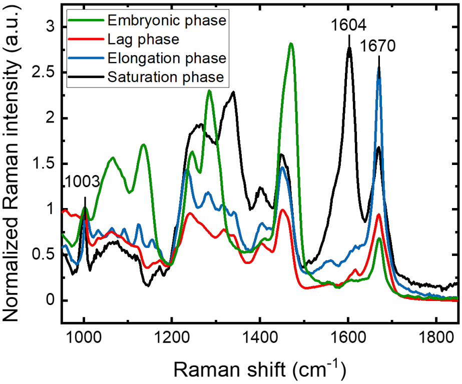

Figure 6.9 Averaged spectral signature of aggregates adsorbed on gold recorded during the embryonic phase (green plot), lag phase (red plot), elongation phase (blue plot) and saturation phase (black plot) occurring along the aggregation pathway of α-Syn, normalized to Phe band at 1003 cm^{-1}.

To visualize better the peak positions, we scaled all the spectra from 0 to 1, as shown in figure 6.10. In the Amide III region (resulting from $C-N$ stretch and $N-H$ bend) (figure 6.10b) we observe a shift to the left of a peak maximum that corresponds to the β-sheet content, in the region from 1220 cm^{-1} to 1248 cm^{-1}[138]. Peak maximum in the embryonic phase is at 1244 cm^{-1}, in the lag phase 1241 cm^{-1}, and in the elongation phase 1239 cm^{-1}. The shift of this peak was also observed by Flynn et. al.[128] upon aggregation of α-Syn. Interestingly, we also observe a shift of a peak from 1285 cm^{-1} to 1282 cm^{-1} from lag to elongation phase, which indicates a decrease of α-helical content. Along with the increase of β-sheet content, this shift indicates aggregation[129].

Bands at 1405 cm^{-1} and 1450 cm^{-1} (figure 6.10c) appear due to the side-chain vibrations, such as CO_2^- (1405 cm^{-1}, symmetric stretch) and CH_2, CH_3 deformations (1450 cm^{-1})[128,139]. These bands are present in the observed spectra throughout the aggregation process. For the lag and elongation phases, we observe a low-intensity peak around 1550 cm^{-1}, which is in the expected

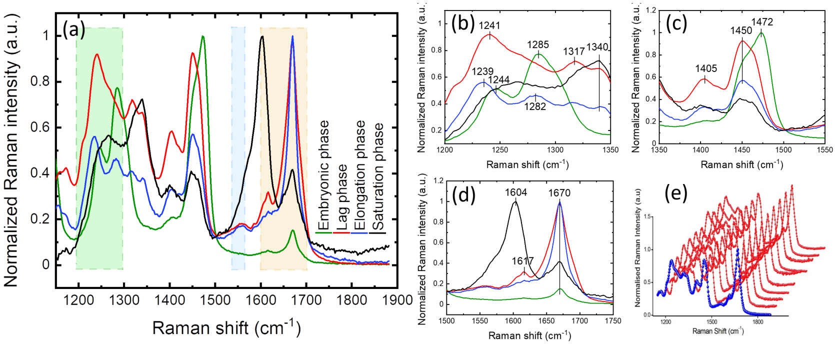

Figure 6.10 Evolution in the chemical structure of αSyn aggregate resolved using Raman spectroscopy. (a) Averaged spectral signature of aggregates adsorbed on gold recorded during the embryonic phase (green plot), lag phase (red plot), elongation phase (blue plot), and saturation phase (black plot), occurring along the aggregation pathway of αSyn. (b) Amide III spectral region (1200-1300 cm^{-1}) indicated by the green shaded region in panel a. (c) Close up to the central region (1350-1550 cm^{-1}), including Amide II spectral region indicated by the blue shaded area in panel a. (d) Amide I spectral region (1600-1700 cm^{-1}) indicated by the orange shaded region in panel a. (e) Individual spectroscopic traces (shown in red plot) and the averaged spectral plot (shown in blue plot) acquired during the elongation phase of αSyn aggregation.

region of the amide II band.

In the Amide I region (mostly due to $C = O$ stretching), shown in figure 6.10d, we observe an increase in the intensity of the peak at 1670 cm^{-1}, compared to the intensities of the peaks in the amide III region, with aggregation from embryonic to elongation phase. This peak corresponds to β-sheet content[138]. For the spectra in figure 6.10a referred to as a saturation phase (black line), a peak with a maximum at 1670 cm^{-1} is less prominent. In this phase, we observe a strong peak with a maximum at 1604 cm^{-1}, which was not present in the previous aggregation states. This peak could be attributed to Phenylalanine (Phe)[118,139], but it is usually weak[129]. Therefore, a more likely assignment of 1004 cm^{-1} peak is a shift of Amide I band upon aggregation, and although it was not observed in the previous phases, it could be coming from the complexity of the αSyn film structure on the surface. Such difference in the spectra, in comparison to the previous phases, indicates that major changes occur in the structure of αSyn aggregates from oligomers to mature fibrils. Indeed, the corresponding to this spectra AFM image (figure 6.6e), shows densely packed fibrillar structures, that were not observed during the previous nine days of the experiment. In addition, we prepare samples for Raman measurements by drop-casting the αSyn solution and letting it dry. Therefore, it is likely that αSyn aggregates in different aggregation stages are present on the same sample, since, in the solution, not all the protein aggregates will be in the same phase, contributing to the variations in the obtained Raman spectra. This is also illustrated in figure 6.10e, which shows Raman spectra acquired during the elongation phase (in red) in the different areas on the sample, and the averaged spectra (in blue). We observe minor changes in the spectra within the same sample that can be due to the presence of aggregates that are in different phases on one sample. Obtained spectra provide structural insights into the chemical structure of aSyn aggregates, complementary to the AFM data.

6.3.4 Impact of Cu^{2+} on the aggregation of αSyn

Copper is involved in many physiological processes and is essential for human health[7]. Therefore alterations in copper homeostasis can lead to various diseases, including neurodegenerative disorders such as PD. The interaction of copper ions with αSyn has been shown to trigger its aggregation[5,121], as binding of Cu^{2+} leads to protein misfolding, which facilitates the aggregation process[121].

Several copper binding sites, consisting of amino acids in N- and C-terminal of αSyn, are known: amino acids Met1, Asp2, and Met5 and Met1, Asp2, in the N-terminal (high affinity binding site), His50 (N-terminal), and Asp119, Asp21, Asn122, and Glu123 in C-terminal (low affinity). Copper ions can bind to αSyn monomer as well as to fibrils, however, the amino acids involved are different.

Figure 6.11 shows simulations of αSyn trimer with Cu^{2+} ion, bound to each αSyn in two ways: via amino acids Met1, Asp2, and a water molecule (2N2O) and Met1, Asp2, and His50 (3N1O).

In αSyn monomeric form, His50 can be involved in binding. However Cu^{2+} does not bind to His50 in fibrils[140], as the end of N-terminal with Met1 and Asp2 amino acids is not coming close enough to His50. In addition, copper that has already bound to His50 in αSyn monomer can abolish this binding site upon αSyn aggregation. As we can see from the simulations, in order to bind Cu^{2+} ion in 3N10 configuration, a significant conformational change of αSyn is required. Therefore, the end of the N-terminal with a binding site consisting of Met1 and Asp2 is much more flexible and favorable when αSyn fibrils are formed.

To investigate how the aggregation pathway of αSyn is affected by Cu^{2+} ions, we incubated the protein with Cu^{2+} of 1 μM concentration. In our experiments, αSyn was exposed to Cu^{2+} starting from its monomeric state, when it can bind to multiple sites. Later, however, throughout the aggregation process, as fibrils start to form, different binding mechanisms take place. The αSyn

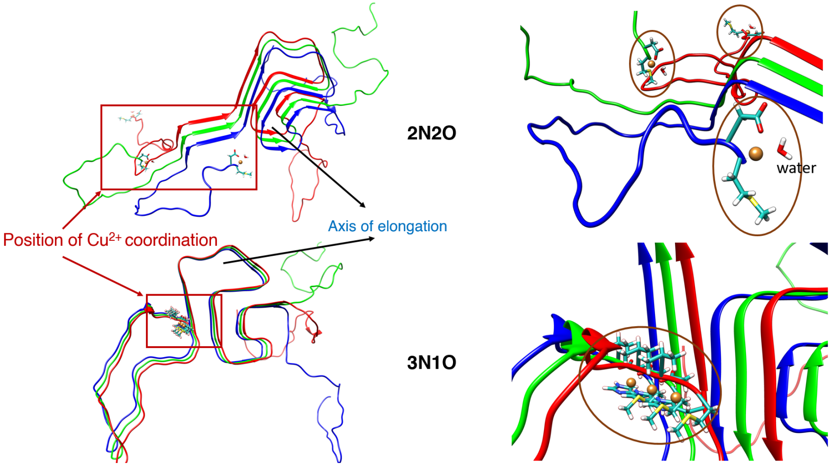

Figure 6.11 Cu^{2+} coordination in αSyn trimer in Greek-key fold via amino acids Met1, Asp2 (a) and via Met1, Asp2 and His50 (c). (b), (d) Close-up to the Cu^{2+} binding sites.

solution was deposited on the Au surface every day from day 1 to day 10 to monitor the aggregation process.

Figure 6.12 shows an AFM image of the αSyn aggregates after one day of aggregation. The majority of structures observed are annular oligomers, which are considered to be the most cytotoxic due to membrane permeabilization[141]. Previously the formation of annular oligomers was observed only as an effect of Ca^{2+} ions[142].

To investigate the chemical structure of the aggregates, we also conducted Raman spectroscopy measurements on the samples incubated with Cu^{2+} over a span of 10 days. The obtained Raman spectra are shown in figure 6.13. From the spectra, we can see that starting from the first day, the spectral signature is similar to the previously observed spectra of αSyn in the elongation phase (6.10a), suggesting an advanced stage of aggregation after such a short time.

We also observe different Amide I band intensities, an increase of which would indicate the advancement of aggregation. However, an increase of intensity with an increase of incubation time is not observed in all the samples. It can happen due to the αSyn aggregates being in different aggregation stages that are present on the same sample, as we have discussed in the previous section.

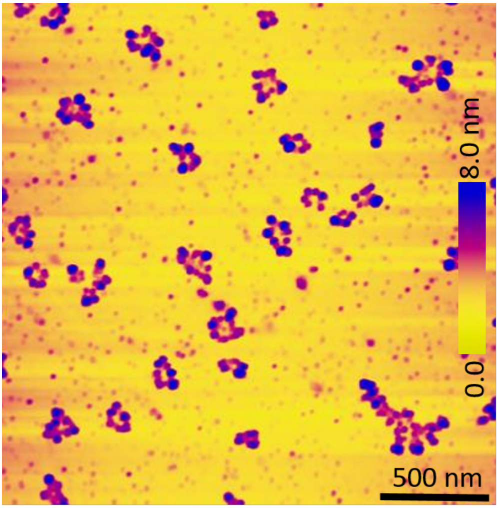

Figure 6.12 AFM image of annular shaped oligomeric αSyn aggregates resolved at the gold water interface after incubating the αSyn solution with copper for 1 day. In addition to the annular oligomers, spherical particles with varying sizes and dendritic structure are also visible from the AFM topograph.

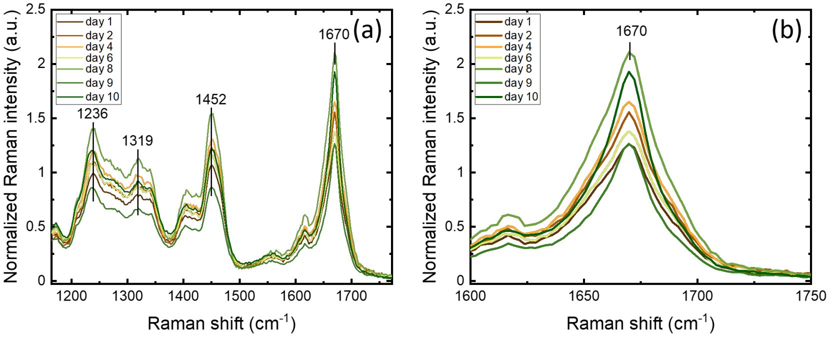

Figure 6.13 Evolution in αSyn aggregate chemical structure resolved by Raman spectroscopy over 10-day experiment. Protein solution was incubated for 10 days, and samples were prepared from day 1 to day 10 to monitor the aggregation process. (a) Spectra obtained throughout the 10 day experiment. (b) Close-up to the Amide I region.

6.4 Conclusions

Early diagnosis and treatment of PD remain a challenge. Understanding the cause of this disease is essential for early detection, which is key for delaying and disabling disease progression.

The hallmark of the disease, protein αSyn, is an intrinsically disordered protein that tends to form aggregates in the brain, therefore these processes are extensively studied. It has been found that some metal ions, such as copper, zinc, calcium, iron, manganese facilitate the aggregation process. Therefore, understanding the reasons for αSyn aggregation and how it is affected by metal ions could be a promising path in search of pre-clinical biomarkers for early treatment of PD.

We combined AFM, Raman spectroscopy, and MD simulations to resolve the aggregation pathway of αSyn at the molecular level. Our measurements were conducted with the purest form of protein in buffer conditions, which can help to understand the aggregation processes happening in the brain in the future by correlating the results with clinical data from patients.

7 Conclusions & Outlook

Metal ions play an important role in vital biochemical processes in the human body, interacting with peptides and proteins. It is known that too low as well as too high concentrations of metal ions can cause various health problems, damaging kidneys, bones, and/or the liver. The imbalance of metal ions is also linked to the development of neurodegenerative diseases, such as Alzheimer's and Parkinson's. Therefore, monitoring the concentration of metal ions and understanding their complexation mechanisms with peptides and proteins opens up possibilities for early diagnosis and for developments of a cure.

In this work, we first systematically investigated the application of peptides GGH and OT for specific detection of Cu^{2+} and Zn^{2+} ions, integrated as receptors in potentiometric sensors.

Direct functionalization, achieved by conjugation of GGH peptide with lipoic acid prior assembly and by utilizing double sulfur bond present in the structure of OT is definitely an advantage to use in sensors. It makes them more convenient in use, simplifying the functionalization procedure as well as saving time for preparation.

The challenges that arise when working with such sensors are due to the complex nature of a solid-liquid interface. Interpreting the measured signal, besides conditions such as kind and pH of electrolyte solution, the concentration range of a target analyte, all the reactions which take place at the surface must be taken into account. Target species interact with an electrode material, resulting in an additional change in the potential at the surface, therefore interfering with the specific signal.

Addressing the issue of the non-specific contributions to the detected signal is necessary, and we took steps towards preventing the interaction of metal ions with the surface by passivating it with a dense layer of thiol molecules and we suggest that surface passivation with a carefully selected molecule could solve this issue.

Our results highlight that great care must be taken when using potentiometric sensors in combination with peptides for affinity sensing, as the electrolyte's properties need to be known. Having multiple surfaces for multiplexed sensing can address this problem, by measuring other parameters in the analyte solution to complete the picture and achieve accurate results.

In the final project, we combine AFM, Raman spectroscopy, and MD simulations to characterize the aggregation pathway of αSyn, a protein that plays a key role in the pathogenesis of Parkinson's disease. AFM allows visualizing αSyn aggregates, resolving them at the molecular level. Raman spectroscopy provides information on their chemical structure, and MD simulations help to understand better how exactly αSyn forms aggregates. The combination of these methods allows distinguishing between different aggregation phases.

Systematically obtained data on pure αSyn are of great importance. Clinical samples, such as CSF or blood obtained from patients, are more complex. Results on pure αSyn aggregation can be then correlated with the clinical data, facilitating the understanding of the diagnosis.

Ultimately, the sensing device for identification of the αSyn aggregates and distinguishing between their stages would be the goal. Taking the best from the field of potentiometric sensors (CMOS compatible fabrication process, small size, flexibility in the design, multiplexed sensing) and the extreme relevance of research on PD for the society due to rapid increase in its incidence over past decades, will be definitely an advantage as a supporting diagnostics method.

Bibliography

[1] Fabrizio Chiti and Christopher M. Dobson. Protein Misfolding, Amyloid Formation, and Human Disease: A Summary of Progress Over the Last Decade. *Annual Review of Biochemistry*, 86(1):27–68, June 2017. ISSN 0066-4154. doi: 10.1146/annurev-biochem-061516-045115.

[2] Guilherme A. P. de Oliveira and Jerson L. Silva. Alpha-synuclein stepwise aggregation reveals features of an early onset mutation in Parkinson's disease. *Communications Biology*, 2:1–13, October 2019. doi: 10.1038/s42003-019-0598-9.

[3] Benedetta Mannini, Johnny Habchi, Sean Chia, Francesco Simone Ruggeri, Michele Perni, Tuomas P. J. Knowles, Christopher M. Dobson, and Michele Vendruscolo. Stabilization and Characterization of Cytotoxic Aβ40 Oligomers Isolated from an Aggregation Reaction in the Presence of Zinc Ions | ACS Chemical Neuroscience. *ACS Chemical Neuroscience*, 9(12):2959–2971, July 2018.

[4] George Devitt, Anna Crisford, William Rice, Hilary A. Weismiller, Zhanyun Fan, Caitlin Commins, Bradley T. Hyman, Martin Margittai, Sumeet Mahajan, and Amrit Mudher. Conformational fingerprinting of tau variants and strains by Raman spectroscopy. *RSC Advances*, 11(15):8899–8915, February 2021. doi: 10.1039/D1RA00870F.

[5] Benjamin Gabriel Poulson, Kacper Szczepski, Joanna Izabela Lachowicz, Lukasz Jaremko, Abdul-Hamid Emwas, and Mariusz Jaremko. Aggregation of biologically important peptides and proteins: Inhibition or acceleration depending on protein and metal ion concentrations. *RSC Advances*, 10(1):215–227, December 2019. ISSN 2046-2069. doi: 10.1039/C9RA09350H.

[6] Lu Wang, Ya-Ling Yin, Xin-Zi Liu, Peng Shen, Yan-Ge Zheng, Xin-Rui Lan, Cheng-Biao Lu, and Jian-Zhi Wang. Current understanding of metal ions in the pathogenesis of Alzheimer's disease. *Translational Neurodegeneration*, 9(1), April 2020. ISSN 2047-9158. doi: 10.1186/s40035-020-00189-z.

[7] Marco Bisaglia and Luigi Bubacco. Copper Ions and Parkinson's Disease: Why Is Homeostasis So Relevant? *Biomolecules*, 10(2), January 2020. doi: 10.3390/biom10020195.

[8] Allison W. Willis, Bradley A. Evanoff, Min Lian, Aiden Galarza, Andrew Wegrzyn, Mario Schootman, and Brad A. Racette. Metal Emissions and Urban Incident Parkinson Disease: A Community Health Study of Medicare Beneficiaries by Using Geographic Information Systems. *American Journal of Epidemiology*, 172(12): 1357–1363, December 2010. ISSN 0002-9262. doi: 10.1093/aje/kwq303.

[9] James Everett, Frederik Lermyte, Jake Brooks, Vindy Tjendana-Tjhin, Germán Plascencia-Villa, Ian Hands-Portman, Jane M. Donnelly, Kharmen Billimoria,

George Perry, Xiongwei Zhu, Peter J. Sadler, Peter B. O'Connor, Joanna F. Collingwood, and Neil D. Telling. Biogenic metallic elements in the human brain? *Science Advances*, 7(24), June 2021. ISSN 2375-2548. doi: 10.1126/sciadv.abf6707.

[10] John Emsley. *Nature's Building Blocks: An A-Z Guide to the Elements*. Oxford University Press, 2001. ISBN 978-0-19-850341-5.

[11] Gemma Aragay, Josefina Pons, and Arben Merkoçi. Recent Trends in Macro-, Micro-, and Nanomaterial-Based Tools and Strategies for Heavy-Metal Detection. *Chemical Reviews*, 111(5):3433–3458, May 2011. ISSN 0009-2665. doi: 10.1021/cr100383r.

[12] Paul B. Tchounwou, Clement G. Yedjou, Anita K. Patlolla, and Dwayne J. Sutton. Heavy Metals Toxicity and the Environment. *EXS*, 101:133–164, 2012. ISSN 1023-294X. doi: 10.1007/978-3-7643-8340-4_6.

[13] Koe Wei Wong, Chee Kong Yap, Rosimah Nulit, Mohd Suhaimi Hamzah, Soo Kien Chen, Wan Hee Cheng, Ali Karami, and Salman Abdo Al-Shami. Effects of anthropogenic activities on the heavy metal levels in the clams and sediments in a tropical river. *Environmental Science and Pollution Research*, 24(1):116–134, January 2017. ISSN 1614-7499. doi: 10.1007/s11356-016-7951-z.

[14] Ahmed A. El-Kady and Mosaad A. Abdel-Wahhab. Occurrence of trace metals in foodstuffs and their health impact. *Trends in Food Science & Technology*, 75: 36–45, May 2018. ISSN 0924-2244. doi: 10.1016/j.tifs.2018.03.001.

[15] Kristiina Väänänen, Matti T. Leppänen, XuePing Chen, and Jarkko Akkanen. Metal bioavailability in ecological risk assessment of freshwater ecosystems: From science to environmental management. *Ecotoxicology and Environmental Safety*, 147:430–446, January 2018. ISSN 0147-6513. doi: 10.1016/j.ecoenv.2017.08.064.

[16] Wai-Yee Chan and Owen M. Rennert. The Role of Copper in Iron Metabolism. *Annals of clinical and laboratory science*, 10(4):338–344, 1980.

[17] Ganna Vashchenko and Ross T. A. MacGillivray. Multi-Copper Oxidases and Human Iron Metabolism. *Nutrients*, 5(7):2289–2313, July 2013. doi: 10.3390/nu5072289.

[18] Peter Hedera, John K. Fink, Paula L. Bockenstedt, and George J. Brewer. Myelopolyneuropathy and Pancytopenia Due to Copper Deficiency and High Zinc Levels of Unknown Origin: Further Support for Existence of a New Zinc Overload Syndrome. *Archives of Neurology*, 60(9):1303–1306, September 2003. ISSN 0003-9942. doi: 10.1001/archneur.60.9.1303.

[19] M. Angelova, S. Asenova, V. Nedkova, and R Koleva-Kolarova. Copper in the human organism. *Trakia Journal of Sciences*, 9(1):88–98, 2011.

[20] George J. Brewer. Alzheimer's disease causation by copper toxicity and treatment with zinc. *Frontiers in Aging Neuroscience*, 6, May 2014. ISSN 1663-4365. doi: 10.3389/fnagi.2014.00092.

[21] H. H. Sandstead. Understanding zinc: Recent observations and interpretations. *The Journal of Laboratory and Clinical Medicine*, 124(3):322–327, September 1994. ISSN 0022-2143.

[22] Chapter 1: Overview of Zinc Nutrition. In *Food and Nutrition Bulletin*, volume 25, pages S99–S129. The United Nations University, January 2004.

[23] Katarzyna Socha, Elżbieta Karpińska, Jan Kochanowicz, Jolanta Soroczyńska, Marta Jakoniuk, Marianna Wilkiel, Zenon D. Mariak, and Maria H. Borawska. Dietary habits; concentration of copper, zinc, and Cu-to-Zn ratio in serum and ability status of patients with relapsing-remitting multiple sclerosis. *Nutrition*, 39–40:76–81, July 2017. ISSN 0899-9007. doi: 10.1016/j.nut.2017.03.009.

[24] Alex S. N. Trindade, Alailson F. Dantas, Daniel C. Lima, Sérgio L. C. Ferreira, and Leonardo S. G. Teixeira. Multivariate optimization of ultrasound-assisted extraction for determination of Cu, Fe, Ni and Zn in vegetable oils by high-resolution continuum source atomic absorption spectrometry. *Food Chemistry*, 185:145–150, October 2015. ISSN 0308-8146. doi: 10.1016/j.foodchem.2015.03.118.

[25] María A. Álvarez and Génesis Carrillo. Simultaneous determination of arsenic, cadmium, copper, chromium, nickel, lead and thallium in total digested sediment samples and available fractions by electrothermal atomization atomic absorption spectroscopy (ET AAS). *Talanta*, 97:505–512, August 2012. ISSN 0039-9140. doi: 10.1016/j.talanta.2012.05.006.

[26] J. Kaiser, M. Galiová, K. Novotný, R. Červenka, L. Reale, J. Novotný, M. Liška, O. Samek, V. Kanický, A. Hrdlička, K. Stejskal, V. Adam, and R. Kizek. Mapping of lead, magnesium and copper accumulation in plant tissues by laser-induced breakdown spectroscopy and laser-ablation inductively coupled plasma mass spectrometry. *Spectrochimica Acta Part B: Atomic Spectroscopy*, 64(1):67–73, January 2009. ISSN 05848547. doi: 10.1016/j.sab.2008.10.040.

[27] Yurui Xue, Xun Li, Hongbin Li, and Wenke Zhang. Quantifying thiol–gold interactions towards the efficient strength control. *Nature Communications*, 5(1): 4348, July 2014. ISSN 2041-1723. doi: 10.1038/ncomms5348.

[28] ISFET pH Sensor. Wellinq vascular innovations. www.wellinq.com/fabrication/isfet-ph-sensor, .

[29] ISFET pH Stainless Steel General Purpose Probe. Hach USA. www.hach.com/isfet-ph-stainless-steel-general-purpose-probe-round-tip-and-waterproof-connector/product-details?id=7640516431, .

[30] Jangsun Hwang, Mintai P. Hwang, Moonhyun Choi, Youngmin Seo, Yeonho Jo, Jaewoo Son, Jinkee Hong, and Jonghoon Choi. Sensitive detection of copper ions via ion-responsive fluorescence quenching of engineered porous silicon nanoparticles. *Scientific Reports*, 6:35565, October 2016. ISSN 2045-2322. doi: 10.1038/srep35565.

[31] Wei Song, Lei Zhang, Lei Shi, Da-Wei Li, Yang Li, and Yi-Tao Long. Simultaneous determination of cadmium(II), lead(II) and copper(II) by using a screen-printed electrode modified with mercury nano-droplets. *Microchimica Acta*, 169(3):321–326, June 2010. ISSN 1436-5073. doi: 10.1007/s00604-010-0354-9.

[32] Caixia Yu, Zhichao Shao, Leilei Liu, and Hongwei Hou. Efficient and Selective Removal of Copper(II) from Aqueous Solution by a Highly Stable Hydrogen-Bonded Metal–Organic Framework. *Crystal Growth & Design*, 18(5):3082–3088, May 2018. ISSN 1528-7483. doi: 10.1021/acs.cgd.8b00224.

[33] Meng Gao, Shuhua Han, Yongfeng Hu, and Lijuan Zhang. Enhanced Fluorescence in Tetraylnitrilomethylidyne–Hexaphenyl Derivative-Functionalized Periodic Mesoporous Organosilicas for Sensitive Detection of Copper(II). *The Journal of Physical Chemistry C*, 120(17):9299–9307, May 2016. ISSN 1932-7447. doi: 10.1021/acs.jpcc.6b01837.

[34] Bin-Cheng Yin, Bang-Ce Ye, Weihong Tan, Hui Wang, and Cong-Cong Xie. An Allosteric Dual-DNAzyme Unimolecular Probe for Colorimetric Detection of Copper(II). *Journal of the American Chemical Society*, 131(41):14624–14625, October 2009. ISSN 0002-7863. doi: 10.1021/ja9062426.

[35] Irena Vopálenská, Libuše Váchová, and Zdena Palková. New biosensor for detection of copper ions in water based on immobilized genetically modified yeast cells. *Biosensors and Bioelectronics*, 72:160–167, October 2015. ISSN 0956-5663. doi: 10.1016/j.bios.2015.05.006.

[36] César Agra-Gutiérrez, Joanna L. Hardcastle, Jon C. Ball, and Richard G. Compton. Anodic stripping voltammetry of copper at insonated glassy carbon-based electrodes: Application to the determination of copper in beer. *Analyst*, 124(7): 1053–1057, January 1999. ISSN 1364-5528. doi: 10.1039/A902974E.

[37] Salamatu Aliyu Tukur, Nor Azah Yusof, and Reza Hajian. Gold Nanoparticles-Modified Screen-Printed Electrode for Determination of Pb(II) Ion Using Linear Sweep Anodic Stripping Voltammetry. *IEEE Sensors Journal*, 15(5):2780–2784, May 2015. ISSN 1558-1748. doi: 10.1109/JSEN.2014.2379283.

[38] Constant M. G. van den Berg and John R. Donat. Determination and data evaluation of copper complexation by organic ligands in sea water using cathodic stripping voltammetry at varying detection windows. *Analytica Chimica Acta*, 257 (2):281–291, February 1992. ISSN 0003-2670. doi: 10.1016/0003-2670(92)85181-5.

[39] Yuanyuan Yang, Ahmad A. Ibrahim, Parastoo Hashemi, and Jennifer L. Stockdill. Real-Time, Selective Detection of Copper(II) Using Ionophore-Grafted Carbon-Fiber Microelectrodes. *Analytical Chemistry*, 88(14):6962–6966, July 2016. ISSN 0003-2700. doi: 10.1021/acs.analchem.6b00825.

[40] Won Seok Han, Hye Young Lee, Sung Ho Jung, Soo Jin Lee, and Jong Hwa Jung. Silica-based chromogenic and fluorogenic hybrid chemosensor materials. *Chemical Society Reviews*, 38(7):1904–1915, June 2009. ISSN 1460-4744. doi: 10.1039/B818893A.

[41] Ran Wang, Wei Wang, Hao Ren, and Junseok Chae. Detection of copper ions in drinking water using the competitive adsorption of proteins. *Biosensors and Bioelectronics*, 57:179–185, July 2014. ISSN 09565663. doi: 10.1016/j.bios.2014.01.056.

[42] J. Gonzalo Wangüemert-Pérez, Abdelfettah Hadij-ElHouati, Alejandro Sánchez-Postigo, Jonas Leuermann, Dan-Xia Xu, Pavel Cheben, Alejandro Ortega-Moñux, Robert Halir, and Íñigo Molina-Fernández. Subwavelength structures for silicon photonics biosensing. *Optics & Laser Technology*, 109:437–448, January 2019. ISSN 0030-3992. doi: 10.1016/j.optlastec.2018.07.071.

[43] Jefferson Chan, Sheel C. Dodani, and Christopher J. Chang. Reaction-based small-molecule fluorescent probes for chemoselective bioimaging. *Nature Chemistry*, 4 (12):973–984, December 2012. ISSN 1755-4349. doi: 10.1038/nchem.1500.

[44] Wentao Xu, Jingjing Tian, Yunbo Luo, Longjiao Zhu, and Kunlun Huang. A rapid and visual turn-off sensor for detecting copper (II) ion based on DNAzyme coupled with HCR-based HRP concatemers. *Scientific Reports*, 7:43362, March 2017. ISSN 2045-2322. doi: 10.1038/srep43362.

[45] Witold Nawrot, Kamila Drzozga, Sylwia Baluta, Joanna Cabaj, and Karol Malecha. A Fluorescent Biosensors for Detection Vital Body Fluids' Agents. *Sensors*, 18(8): 2357, August 2018. doi: 10.3390/s18082357.

[46] Hoang Hiep Nguyen and and Moonil Kim. An Overview of Techniques in Enzyme Immobilization. *Applied Science and Convergence Technology*, 26(6):157–163, November 2017. doi: 10.5757/ASCT.2017.26.6.157.

[47] Sevinc Kurbanoglu, Bengi Uslu, and Sibel A. Ozkan. Chapter 8 - Nanobiodevices for electrochemical biosensing of pharmaceuticals. In Alexandru Mihai Grumezescu, editor, *Nanostructures for the Engineering of Cells, Tissues and Organs*, pages 291–330. William Andrew Publishing, January 2018. ISBN 978-0-12-813665-2. doi: 10.1016/B978-0-12-813665-2.00008-9.

[48] Friedrich Oehme. Liquid Electrolyte Sensors: Potentiometry, Amperometry, and Conductometry. In W. Göpel, J. Hesse, and J. N. Zemel, editors, *Sensors: Chemical and Biochemical Sensors - Part I, Volume 2*. October 1991.

[49] S. B. Adeloju. Amperometry. In Paul Worsfold, Alan Townshend, and Colin Poole, editors, *Encyclopedia of Analytical Science (Second Edition)*, pages 70–79. Elsevier, Oxford, January 2005. ISBN 978-0-12-369397-6. doi: 10.1016/B0-12-369397-7/00012-1.

[50] K. Warriner and A. Namvar. 4.60 - Biosensors for Foodborne Pathogen Detection. In Murray Moo-Young, editor, *Comprehensive Biotechnology (Third Edition)*, pages 715–730. Pergamon, Oxford, January 2011. ISBN 978-0-444-64047-5. doi: 10.1016/B978-0-444-64046-8.00250-0.

[51] P. Bergveld. Development of an Ion-Sensitive Solid-State Device for Neurophysiological Measurements. *IEEE Transactions on Biomedical Engineering*, BME-17 (1):70–71, January 1970. ISSN 0018-9294. doi: 10.1109/TBME.1970.4502688.

[52] Deniz Sadighbayan, Mohammad Hasanzadeh, and Ebrahim Ghafar-Zadeh. Biosensing based on field-effect transistors (FET): Recent progress and challenges. *Trends in Analytical Chemistry*, 133:116067, December 2020. ISSN 0165-9936. doi: 10.1016/j.trac.2020.116067.

[53] M. Simić, L. Manjakkal, K. Zaraska, G. M. Stojanović, and R. Dahiya. TiO2-Based Thick Film pH Sensor. *IEEE Sensors Journal*, 17(2):248–255, January 2017. ISSN 1558-1748. doi: 10.1109/JSEN.2016.2628765.

[54] P. Salvo, B. Melai, N. Calisi, C. Paoletti, F. Bellagambi, A. Kirchhain, M. G. Trivella, R. Fuoco, and F. Di Francesco. Graphene-based devices for measuring pH. *Sensors and Actuators B: Chemical*, 256:976–991, March 2018. ISSN 0925-4005. doi: 10.1016/j.snb.2017.10.037.

[55] Xiaoli Zhao, Bin Cai, Qingxin Tang, Yanhong Tong, and Yichun Liu. One-Dimensional Nanostructure Field-Effect Sensors for Gas Detection. *Sensors (Basel, Switzerland)*, 14(8):13999–14020, July 2014. ISSN 1424-8220. doi: 10.3390/s140813999.

[56] Ralph L. Stoop, Mathias Wipf, Steffen Müller, Kristine Bedner, Iain A. Wright, Colin J. Martin, Edwin C. Constable, Axel Fanget, Christian Schönenberger, and Michel Calame. Implementing Silicon Nanoribbon Field-Effect Transistors as Arrays for Multiple Ion Detection. *Biosensors*, 6(2):21, May 2016. doi: 10.3390/bios6020021.

[57] Mathias Wipf, Ralph L. Stoop, Giulio Navarra, Said Rabbani, Beat Ernst, Kristine Bedner, Christian Schönenberger, and Michel Calame. Label-Free FimH Protein Interaction Analysis Using Silicon Nanoribbon BioFETs. *ACS Sensors*, 1(6):781–788, June 2016. doi: 10.1021/acssensors.6b00089.

[58] Jonathan M. Rothberg, Wolfgang Hinz, Todd M. Rearick, Jonathan Schultz, William Mileski, Mel Davey, John H. Leamon, Kim Johnson, Mark J. Milgrew, Matthew Edwards, Jeremy Hoon, Jan F. Simons, David Marran, Jason W. Myers, John F. Davidson, Annika Branting, John R. Nobile, Bernard P. Puc, David Light, Travis A. Clark, Martin Huber, Jeffrey T. Branciforte, Isaac B. Stoner, Simon E. Cawley, Michael Lyons, Yutao Fu, Nils Homer, Marina Sedova, Xin Miao, Brian Reed, Jeffrey Sabina, Erika Feierstein, Michelle Schorn, Mohammad Alanjary, Eileen Dimalanta, Devin Dressman, Rachel Kasinskas, Tanya Sokolsky, Jacqueline A. Fidanza, Eugeni Namsaraev, Kevin J. McKernan, Alan Williams, G. Thomas Roth, and James Bustillo. An integrated semiconductor device enabling non-optical genome sequencing. *Nature*, 475(7356):348–352, July 2011. ISSN 1476-4687. doi: 10.1038/nature10242.

[59] Giwan Seo, Geonhee Lee, Mi Jeong Kim, Seung-Hwa Baek, Minsuk Choi, Keun Bon Ku, Chang-Seop Lee, Sangmi Jun, Daeui Park, Hong Gi Kim, Seong-Jun Kim, Jeong-O Lee, Bum Tae Kim, Edmond Changkyun Park, and Seung Il Kim. Rapid Detection of COVID-19 Causative Virus (SARS-CoV-2) in Human Nasopharyngeal Swab Specimens Using Field-Effect Transistor-Based Biosensor. *ACS Nano*, 14(4):5135–5142, April 2020. ISSN 1936-0851. doi: 10.1021/acsnano.0c02823.

[60] Tatsuro Goda and Yuji Miyahara. Label-free and reagent-less protein biosensing using aptamer-modified extended-gate field-effect transistors. *Biosensors and Bioelectronics*, 45:89–94, July 2013. ISSN 0956-5663. doi: 10.1016/j.bios.2013.01.053.

[61] Cao-An Vu and Wen-Yih Chen. Field-Effect Transistor Biosensors for Biomedical Applications: Recent Advances and Future Prospects. *Sensors*, 19(19):4214, January 2019. doi: 10.3390/s19194214.

[62] L. Keeble, N. Moser, J. Rodriguez-Manzano, and P. Georgiou. ISFET-Based Sensing and Electric Field Actuation of DNA for On-Chip Detection: A Review. *IEEE Sensors Journal*, 20(19):11044–11065, October 2020. ISSN 1558-1748. doi: 10.1109/JSEN.2020.2998168.

[63] N. Miscourides, L. Yu, J. Rodriguez-Manzano, and P. Georgiou. A 12.8 k Current-Mode Velocity-Saturation ISFET Array for On-Chip Real-Time DNA Detection. *IEEE Transactions on Biomedical Circuits and Systems*, 12(5):1202–1214, October 2018. ISSN 1940-9990. doi: 10.1109/TBCAS.2018.2851448.

[64] J. van der Spiegel, I. Lauks, P. Chan, and D. Babic. The extended gate chemically sensitive field effect transistor as multi-species microprobe. *Sensors and Actuators*, 4:291–298, January 1983. ISSN 0250-6874. doi: 10.1016/0250-6874(83)85035-5.

[65] Salvatore Andrea Pullano, Costantino Davide Critello, Ifana Mahbub, Nishat Tarannum Tasneem, Samira Shamsir, Syed Kamrul Islam, Marta Greco, and Antonino S. Fiorillo. EGFET-Based Sensors for Bioanalytical Applications: A Review. *Sensors*, 18(11):4042, November 2018. doi: 10.3390/s18114042.

[66] Alwan M. Alwan, Mehdi Q. Zayer, Allaa A. Jabbar, and Amer B. Dheyab. Optimizing the performance of extended-gate field-effect transistor (EGFET) pH sensor by regulating the structural properties of the nanostructured porous silicon layer. *Journal of Theoretical and Applied Physics*, 14(1):61–70, December 2020. ISSN 2251-7235. doi: 10.1007/s40094-020-00403-3.

[67] R. E. G. van Hal, J. C. T. Eijkel, and P. Bergveld. A novel description of ISFET sensitivity with the buffer capacity and double-layer capacitance as key parameters. *Sensors and Actuators B: Chemical*, 24(1):201–205, March 1995. ISSN 0925-4005. doi: 10.1016/0925-4005(95)85043-0.

[68] pH and Water. https://www.usgs.gov/special-topic/water-science-school/science/ph-and-water?qt-science_center_objects=0#qt-science_center_objects.

[69] M. Waleed Shinwari, M. Jamal Deen, and Dolf Landheer. Study of the electrolyte-insulator-semiconductor field-effect transistor (EISFET) with applications in biosensor design. *Microelectronics Reliability*, 47(12):2025–2057, December 2007. ISSN 0026-2714. doi: 10.1016/j.microrel.2006.10.003.

[70] L. Bousse, N.F. De Rooij, and P. Bergveld. Operation of chemically sensitive field-effect sensors as a function of the insulator-electrolyte interface. *IEEE Transactions on Electron Devices*, 30(10):1263–1270, October 1983. ISSN 1557-9646. doi: 10.1109/T-ED.1983.21284.

[71] R. E. G. van Hal, J. C. T. Eijkel, and P. Bergveld. A general model to describe the electrostatic potential at electrolyte oxide interfaces. *Advances in colloid and interface science*, 69(1-3):31–62, 1996. ISSN 0001-8686. doi: 10.1016/S0001-8686(96)00307-7.

[72] David E. Yates, Samuel Levine, and Thomas W. Healy. Site-binding Model of the Electrical Double Layer at the Oxide/Water Interface. *Journal of the Chemical Society, Faraday Transactions 1: Physical Chemistry in Condensed Phases*, 1(70): 1807–1818, 1974.

[73] Libu Manjakkal, Dorota Szwagierczak, and Ravinder Dahiya. Metal oxides based electrochemical pH sensors: Current progress and future perspectives. *Progress in Materials Science*, 109:100635, April 2020. ISSN 0079-6425. doi: 10.1016/j.pmatsci.2019.100635.

[74] J.W. McPherson, Jinyoung Kim, A. Shanware, H. Mogul, and J. Rodriguez. Trends in the ultimate breakdown strength of high dielectric-constant materials. *IEEE Transactions on Electron Devices*, 50(8):1771–1778, August 2003. ISSN 1557-9646. doi: 10.1109/TED.2003.815141.

[75] Piet Bergveld. Thirty years of ISFETOLOGY What happened in the past 30 years and what may happen in the next 30 years. *Sensors and Actuators B*, 88: 1–20, 2003.

[76] A. Tarasov, M. Wipf, K. Bedner, J. Kurz, W. Fu, V. A. Guzenko, O. Knopfmacher, R. L. Stoop, M. Calame, and C. Schönenberger. True Reference Nanosensor Realized with Silicon Nanowires. *Langmuir*, 28(25):9899–9905, June 2012. ISSN 0743-7463. doi: 10.1021/la301555r.

[77] Kristine Bedner. *Fabrication and Characterization of Ion-Sensitive Field Effect Transistors Using Silicon-on-Insulator Technology*. PhD thesis, University of Basel, 2013.

[78] Mathias Wipf, Ralph L. Stoop, Alexey Tarasov, Kristine Bedner, Wangyang Fu, Iain A. Wright, Colin J. Martin, Edwin C. Constable, Michel Calame, and Christian Schönenberger. Selective Sodium Sensing with Gold-Coated Silicon Nanowire Field-Effect Transistors in a Differential Setup. *ACS Nano*, 7(7):5978–5983, July 2013. ISSN 1936-0851. doi: 10.1021/nn401678u.

[79] O. Knopfmacher, A. Tarasov, Wangyang Fu, M. Wipf, B. Niesen, M. Calame, and C. Schönenberger. Nernst Limit in Dual-Gated Si-Nanowire FET Sensors. *Nano Letters*, 10(6):2268–2274, June 2010. ISSN 1530-6984. doi: 10.1021/nl100892y.

[80] Evgeniy Mervinetsky, Israel Alshanski, Yonatan Hamo, Leonardo Medrano Sandonas, Arezoo Dianat, Jörg Buchwald, Rafael Gutierrez, Gianaurelio Cuniberti, Mattan Hurevich, and Shlomo Yitzchaik. Copper Induced Conformational Changes of Tripeptide Monolayer Based Impedimetric Biosensor. *Scientific Reports*, 7(1): 9498, August 2017. ISSN 2045-2322. doi: 10.1038/s41598-017-10288-z.

[81] Kosh P. Neupane, Amanda R. Aldous, and Joshua A. Kritzer. Metal-Binding and Redox Properties of Substituted Linear and Cyclic ATCUN Motifs. *Journal of inorganic biochemistry*, 0:65–76, October 2014. ISSN 0162-0134. doi: 10.1016/j.jinorgbio.2014.06.004.

[82] Soma Papp, Gyula Jágerszki, and Róbert E. Gyurcsányi. Ion-Selective Electrodes Based on Hydrophilic Ionophore-Modified Nanopores. *Angewandte Chemie*, 130 (17):4842–4845, 2018. ISSN 1521-3757. doi: 10.1002/ange.201800954.

[83] Silvia Pavan and Federico Berti. Short peptides as biosensor transducers. *Analytical and Bioanalytical Chemistry*, 402(10):3055–3070, April 2012. ISSN 1618-2650. doi: 10.1007/s00216-011-5589-8.

[84] Xiaoyu Hu, Qian Zhang, Wei Wang, Zhi Yuan, Xushan Zhu, Bing Chen, and Xingyu Chen. Tripeptide GGH as the Inhibitor of Copper-Amyloid-β-Mediated Redox Reaction and Toxicity. *ACS Chemical Neuroscience*, 7(9):1255–1263, September 2016. doi: 10.1021/acschemneuro.6b00145.

[85] Kanokwan Kulprachakarn, Yu-Lin Chen, Xiaole Kong, Maria C. Arno, Robert C. Hider, Somdet Srichairatanakool, and Sukhvinder S. Bansal. Copper(II) binding properties of hepcidin. *Journal of Biological Inorganic Chemistry*, 21:329–338, 2016. ISSN 0949-8257. doi: 10.1007/s00775-016-1342-2.

[86] M. Lin, M.S. Cho, W.S. Choe, and Y. Lee. Electrochemical analysis of copper ion using a Gly–Gly–His tripeptide modified poly(3-thiopheneacetic acid) biosensor. *Biosensors and Bioelectronics*, 25(1):28–33, September 2009. ISSN 09565663. doi: 10.1016/j.bios.2009.05.035.

[87] Wenrong Yang, Edith Chow, Gary D. Willett, D. Brynn Hibbert, and J. Justin Gooding. Exploring the use of the tripeptide Gly–Gly–His as a selective recognition element for the fabrication of electrochemical copper sensors. *Analyst*, 128(6): 712–718, January 2003. ISSN 1364-5528. doi: 10.1039/B212881K.

[88] Mária Raics, Daniele Sanna, Imre Sóvágó, and Csilla Kállay. Copper(II), nickel(II) and zinc(II) complexes of hexapeptides containing separate aspartyl and histidyl residues. *Inorganica Chimica Acta*, 426:99–106, February 2015. ISSN 0020-1693. doi: 10.1016/j.ica.2014.11.012.

[89] Wenrong Yang, David Jaramillo, J. Justin Gooding, D. Brynn Hibbert, Rui Zhang, Gary D. Willett, and Keith J. Fisher. Sub-ppt detection limits for copper ions with Gly-Gly-His modified electrodes. *Chemical Communications*, (19):1982–1983, 2001. ISSN 13597345, 1364548X. doi: 10.1039/b106730n.

[90] Ying-Ming Xu, Hong-Qing Pan, San-Hua Wu, and Bai-Lin Zhang. Interaction Between Tripeptide Gly-Gly-His and Cu2+ Probed by Microcantilevers. *Chinese Journal of Analytical Chemistry*, 37(6):783–787, June 2009. ISSN 1872-2040. doi: 10.1016/S1872-2040(08)60106-1.

[91] Thomas Wyttenbach, Dengfeng Liu, and Michael T. Bowers. Interactions of the Hormone Oxytocin with Divalent Metal Ions. *Journal of the American Chemical Society*, 130(18):5993–6000, May 2008. ISSN 0002-7863. doi: 10.1021/ja8002342.

[92] Kiran Kumar Tadi, Israel Alshanski, Evgeniy Mervinetsky, Gerard Marx, Panayiota Petrou, Karussis M. Dimitrios, Chaim Gilon, Mattan Hurevich, and Shlomo Yitzchaik. Oxytocin-Monolayer-Based Impedimetric Biosensor for Zinc and Copper Ions. *ACS Omega*, 2(12):8770–8778, December 2017. ISSN 2470-1343. doi: 10.1021/acsomega.7b01404.

[93] Evgeniy Mervinetsky, Israel Alshanski, Jörg Buchwald, Arezoo Dianat, Ivor Lončarić, Predrag Lazić, Željko Crljen, Rafael Gutierrez, Gianaurelio Cuniberti, Mattan Hurevich, and Shlomo Yitzchaik. Direct Assembly and Metal-Ion Binding Properties of Oxytocin Monolayer on Gold Surfaces. *Langmuir*, 35(34):11114–11122, August 2019. ISSN 0743-7463. doi: 10.1021/acs.langmuir.9b01830.

[94] Michael J. Stevenson, Kylie S. Uyeda, Nathaniel H. O. Harder, and Marie C. Heffern. Metal-dependent hormone function: The emerging interdisciplinary field of metalloendocrinology. *Metallomics*, 11(1):85–110, January 2019. ISSN 1756-591X. doi: 10.1039/C8MT00221E.

[95] Dengfeng Liu, Alexandra B. Seuthe, Oli T. Ehrler, Xiaohua Zhang, Thomas Wyttenbach, Jeffrey F. Hsu, and Michael T. Bowers. Oxytocin-Receptor Binding: Why Divalent Metals Are Essential. *Journal of the American Chemical Society*, 127(7):2024–2025, February 2005. ISSN 0002-7863. doi: 10.1021/ja046042v.

[96] Xuee Xu, Wenbo Yu, Zhijian Huang, and Zijing Lin. Comprehensive Density Functional Theory Study on the Mechanism of Activation of the Nonapeptide Hormone Oxytocin by Metal Ions. *The Journal of Physical Chemistry B*, 114(3): 1417–1423, January 2010. ISSN 1520-6106. doi: 10.1021/jp907436p.

[97] Israel Alshanski, Deborah E. Shalev, Shlomo Yitzchaik, and Mattan Hurevich. Determining the structure and binding mechanism of oxytocin-Cu2+ complex using paramagnetic relaxation enhancement NMR analysis. *JBIC Journal of Biological Inorganic Chemistry*, August 2021. ISSN 1432-1327. doi: 10.1007/s00775-021-01897-1.

[98] A. Frances Pearlmutter and Melvyn S. Soloff. Characterization of the Metal ion Requirement for Oxytocin-Reseptor Interaction in Rat Mammary Gland Membranes. *The Journal of Biological Chmisrty*, 254(10):3899–3906, 1979.

[99] Aleksandar Vacic, Jason M. Criscione, Nitin K. Rajan, Eric Stern, Tarek M. Fahmy, and Mark A. Reed. Determination of Molecular Configuration by Debye Length Modulation. *Journal of the American Chemical Society*, 133(35):13886–13889, September 2011. ISSN 0002-7863. doi: 10.1021/ja205684a.

[100] Olena Synhaivska, Yves Mermoud, Masoud Baghernejad, Israel Alshanski, Mattan Hurevich, Shlomo Yitzchaik, Mathias Wipf, and Michel Calame. Detection of Cu2+ Ions with GGH Peptide Realized with Si-Nanoribbon ISFET. *Sensors*, 19 (18):4022, January 2019. doi: 10.3390/s19184022.

[101] Xinyan Bi and Kun-Lin Yang. Complexation of Copper Ions with Histidine-Containing Tripeptides Immobilized on Solid Surfaces. *Langmuir*, 23(22):11067–11073, October 2007. ISSN 0743-7463. doi: 10.1021/la7016243.

[102] Catherine Harford and Bibudhendra Sarkar. Amino Terminal Cu(II)- and Ni(II)-Binding (ATCUN) Motif of Proteins and Peptides: Metal Binding, DNA Cleavage, and Other Properties †. *Accounts of Chemical Research*, 30(3):123–130, March 1997. ISSN 0001-4842, 1520-4898. doi: 10.1021/ar9501535.

[103] W. Bal, M. Dyba, and H. Kozłowski. The impact of the amino-acid sequence on the specificity of copper(II) interactions with peptides having nonco-ordinating side-chains. *Acta Biochimica Polonica*, 44(3):467–476, 1997. ISSN 0001-527X.

[104] Urszula E. Wawrzyniak, Patrycja Ciosek, Michał Zaborowski, Guozhen Liu, and J. Justin Gooding. Gly-Gly-His Immobilized On Monolayer Modified Back-Side Contact Miniaturized Sensors for Complexation of Copper Ions. *Electroanalysis*, 25(6):1461–1471, June 2013. ISSN 1521-4109. doi: 10.1002/elan.201200667.

[105] T. T. K. Nguyen, H. V. Tran, T. T. Vu, S. Reisberg, V. Noël, G. Mattana, M. C. Pham, and B. Piro. Peptide-modified electrolyte-gated organic field effect transistor. Application to Cu2+ detection. *Biosensors and Bioelectronics*, 127: 118–125, February 2019. ISSN 0956-5663. doi: 10.1016/j.bios.2018.12.005.

[106] Robert W. Hay, Mansour M. Hassan, and Chen You-Quan. Kinetic and thermodynamic studies of the copper(II) and nickel(II) complexes of glycylglycyl-L-histidine. *Journal of Inorganic Biochemistry*, 52(1):17–25, October 1993. ISSN 0162-0134. doi: 10.1016/0162-0134(93)85619-J.

[107] Jasenka Vuceta and James J. Morgan. Hydrolysis of Cu(II)1. *Limnology and Oceanography*, 22(4):742–746, July 1977. ISSN 00243590. doi: 10.4319/lo.1977.22.4.0742.

[108] A.Z.M. Badruddoza, A.S.H. Tay, P.Y. Tan, K. Hidajat, and M.S. Uddin. Carboxymethyl-β-cyclodextrin conjugated magnetic nanoparticles as nanoadsorbents for removal of copper ions: Synthesis and adsorption studies. *Journal of Hazardous Materials*, 185(2-3):1177–1186, January 2011. ISSN 03043894. doi: 10.1016/j.jhazmat.2010.10.029.

[109] G. Licheri, A. Musinu, G. Paschina, G. Piccaluga, G. Pinna, and A. F. Sedda. Coordination of Cu(II) in Cu(NO $_3$) $_2$ aqueous solutions. *The Journal of Chemical Physics*, 80(10):5308–5311, May 1984. ISSN 0021-9606, 1089-7690. doi: 10.1063/1.446559.

[110] D. B. McPhail and B. A. Goodman. Tris buffer–a case for caution in its use in copper-containing systems. *Biochemical Journal*, 221(2):559–560, July 1984. ISSN 0264-6021.

[111] Ana Paula Kallaur, Sayonara Rangel Oliveira, Andréa Name Colado Simão, Daniela Frizon Alfieri, Tamires Flauzino, Josiane Lopes, Wildea Lice de Carvalho Jennings Pereira, Caio de Meleck Proença, Sueli Donizete Borelli, Damacio Ramón Kaimen-Maciel, Michael Maes, and Edna Maria Vissoci Reiche. Cytokine Profile in Patients with Progressive Multiple Sclerosis and Its Association with Disease Progression and Disability. *Molecular Neurobiology*, 54(4):2950–2960, May 2017. ISSN 1559-1182. doi: 10.1007/s12035-016-9846-x.

[112] H. Tapiero, D. M. Townsend, and K. D. Tew. Trace elements in human physiology and pathology. Copper. *Biomedicine & Pharmacotherapy*, 57(9):386–398, November 2003. ISSN 0753-3322. doi: 10.1016/S0753-3322(03)00012-X.

[113] Patricia I. Oteiza. Zinc and the modulation of redox homeostasis. *Free Radical Biology and Medicine*, 53(9):1748–1759, November 2012. ISSN 0891-5849. doi: 10.1016/j.freeradbiomed.2012.08.568.

[114] S. Sri Krishna, Indraneel Majumdar, and Nick V. Grishin. Structural classification of zinc fingers. *Nucleic Acids Research*, 31(2):532–550, January 2003. ISSN 0305-1048. doi: 10.1093/nar/gkg161.

[115] T. Meier, F. Menges, P. Nirmalraj, H. Hölscher, H. Riel, and B. Gotsmann. Length-Dependent Thermal Transport along Molecular Chains. *Physical Review Letters*, 113(6):060801, August 2014. doi: 10.1103/PhysRevLett.113.060801.

[116] E. Ray Dorsey, Alexis Elbaz, Emma Nichols, Foad Abd-Allah, Ahmed Abdelalim, Jose C. Adsuar, Mustafa Geleto Ansha, Carol Brayne, Jee-Young J. Choi, Daniel Collado-Mateo, Nabila Dahodwala, Huyen Phuc Do, Dumessa Edessa, Matthias Endres, Seyed-Mohammad Fereshtehnejad, Kyle J. Foreman, Fortune Gbetoho Gankpe, Rahul Gupta, Graeme J. Hankey, Simon I. Hay, Mohamed I. Hegazy, Desalegn T. Hibstu, Amir Kasaeian, Yousef Khader, Ibrahim Khalil, Young-Ho Khang, Yun Jin Kim, Yoshihiro Kokubo, Giancarlo Logroscino, João Massano, Norlinah Mohamed Ibrahim, Mohammed A. Mohammed, Alireza Mohammadi, Maziar Moradi-Lakeh, Mohsen Naghavi, Binh Thanh Nguyen, Yirga Legesse Nirayo, Felix Akpojene Ogbo, Mayowa Ojo Owolabi, David M. Pereira, Maarten J. Postma,

Mostafa Qorbani, Muhammad Aziz Rahman, Kedir T. Roba, Hosein Safari, Saeid Safiri, Maheswar Satpathy, Monika Sawhney, Azadeh Shafieesabet, Mekonnen Sisay Shiferaw, Mari Smith, Cassandra E. I. Szoeke, Rafael Tabarés-Seisdedos, Nu Thi Truong, Kingsley Nnanna Ukwaja, Narayanaswamy Venketasubramanian, Santos Villafaina, Kidu gidey Weldegwergs, Ronny Westerman, Tissa Wijeratne, Andrea S. Winkler, Bach Tran Xuan, Naohiro Yonemoto, Valery L. Feigin, Theo Vos, and Christopher J. L. Murray. Global, regional, and national burden of Parkinson's disease, 1990–2016: A systematic analysis for the Global Burden of Disease Study 2016. *The Lancet Neurology*, 17(11):939–953, November 2018. ISSN 1474-4422, 1474-4465. doi: 10.1016/S1474-4422(18)30295-3.

[117] C. Marras, J. C. Beck, J. H. Bower, E. Roberts, B. Ritz, G. W. Ross, R. D. Abbott, R. Savica, S. K. Van Den Eeden, A. W. Willis, and C. M. Tanner. Prevalence of Parkinson's disease across North America. *NPJ Parkinson's disease*, 4:1–21, 2018. ISSN 2373-8057. doi: 10.1038/s41531-018-0058-0.

[118] Panchanan Maiti, Jayeeta Manna, and Gary L. Dunbar. Current understanding of the molecular mechanisms in Parkinson's disease: Targets for potential treatments. *Translational Neurodegeneration*, 6(1):28, October 2017. ISSN 2047-9158. doi: 10.1186/s40035-017-0099-z.

[119] David T. Dexter and Peter Jenner. Parkinson disease: From pathology to molecular disease mechanisms. *Free Radical Biology and Medicine*, 62:132–144, September 2013. ISSN 0891-5849. doi: 10.1016/j.freeradbiomed.2013.01.018.

[120] Andreas Nabers, Julian Ollesch, Jonas Schartner, Carsten Kötting, Just Genius, Henning Hafermann, Hans Klafki, Klaus Gerwert, and Jens Wiltfang. Amyloid-β-Secondary Structure Distribution in Cerebrospinal Fluid and Blood Measured by an Immuno-Infrared-Sensor: A Biomarker Candidate for Alzheimer's Disease. *Analytical Chemistry*, 88(5):2755–2762, March 2016. ISSN 1520-6882. doi: 10.1021/acs.analchem.5b04286.

[121] Eleonora Carboni and Paul Lingor. Insights on the interaction of alpha-synuclein and metals in the pathophysiology of Parkinson's disease. *Metallomics: Integrated Biometal Science*, 7(3):395–404, March 2015. ISSN 1756-591X. doi: 10.1039/c4mt00339j.

[122] Rani Moons, Albert Konijnenberg, Carl Mensch, Roos Van Elzen, Christian Johannessen, Stuart Maudsley, Anne-Marie Lambeir, and Frank Sobott. Metal ions shape α-synuclein. *Scientific Reports*, 10(1):16293, October 2020. ISSN 2045-2322. doi: 10.1038/s41598-020-73207-9.

[123] Francesco Simone Ruggeri, Patrick Flagmeier, Janet R. Kumita, Georg Meisl, Dimitri Y. Chirgadze, Marie N. Bongiovanni, Tuomas P. J. Knowles, and Christopher M. Dobson. The Influence of Pathogenic Mutations in α-Synuclein on Biophysical and Structural Characteristics of Amyloid Fibrils. *ACS Nano*, 14(5):5213–5222, May 2020. ISSN 1936-0851. doi: 10.1021/acsnano.9b09676.

[124] Amberley D. Stephens, Maria Zacharopoulou, and Gabriele S. Kaminski Schierle. The Cellular Environment Affects Monomeric α-Synuclein Structure. *Trends in Biochemical Sciences*, 44(5):453–466, May 2019. ISSN 0968-0004. doi: 10.1016/j.tibs.2018.11.005.

[125] M. Julia Roberti, Jonas Fölling, M. Soledad Celej, Mariano Bossi, Thomas M. Jovin, and Elizabeth A. Jares-Erijman. Imaging Nanometer-Sized α-Synuclein Aggregates by Superresolution Fluorescence Localization Microscopy. *Biophysical Journal*, 102(7):1598–1607, April 2012. ISSN 0006-3495. doi: 10.1016/j.bpj.2012.03.010.

[126] Pratibha Kumari, Dhiman Ghosh, Agathe Vanas, Yanick Fleischmann, Thomas Wiegand, Gunnar Jeschke, Roland Riek, and Cédric Eichmann. Structural insights into α-synuclein monomer–fibril interactions. *Proceedings of the National Academy of Sciences*, 118(10), March 2021. ISSN 0027-8424, 1091-6490. doi: 10.1073/pnas.2012171118.

[127] Shayon Bhattacharya, Liang Xu, and Damien Thompson. Long-range Regulation of Partially Folded Amyloidogenic Peptides. *Scientific Reports*, 10(1):7597, May 2020. ISSN 2045-2322. doi: 10.1038/s41598-020-64303-x.

[128] Jessica D. Flynn, Ryan P. McGlinchey, Robert L. Walker, and Jennifer C. Lee. Structural features of α-synuclein amyloid fibrils revealed by Raman spectroscopy. *Journal of Biological Chemistry*, 293(3):767–776, January 2018. ISSN 0021-9258. doi: 10.1074/jbc.M117.812388.

[129] Mihaela M. Apetri, Nakul C. Maiti, Michael G. Zagorski, Paul R. Carey, and Vernon E. Anderson. Secondary Structure of α-Synuclein Oligomers: Characterization by Raman and Atomic Force Microscopy. *Journal of Molecular Biology*, 355(1):63–71, January 2006. ISSN 0022-2836. doi: 10.1016/j.jmb.2005.10.071.

[130] Shirley Yin-Yu Pang, Philip Wing-Lok Ho, Hui-Fang Liu, Chi-Ting Leung, Lingfei Li, Eunice Eun Seo Chang, David Boyer Ramsden, and Shu-Leong Ho. The interplay of aging, genetics and environmental factors in the pathogenesis of Parkinson's disease. *Translational Neurodegeneration*, 8(1):23, August 2019. ISSN 2047-9158. doi: 10.1186/s40035-019-0165-9.

[131] Alberto Ascherio and Michael A Schwarzschild. The epidemiology of Parkinson's disease: Risk factors and prevention. *The Lancet Neurology*, 15(12):1257–1272, November 2016. ISSN 1474-4422. doi: 10.1016/S1474-4422(16)30230-7.

[132] What's Hot in PD? Environmental Risks for PD: Manganese, Welding, Mining, and Parkinsonism. https://www.parkinson.org/blog/whats-hot/manganese-welding-mining-parkinsonism.

[133] Dilshan S. Harischandra, Dharmin Rokad, Matthew L. Neal, Shivani Ghaisas, Sireesha Manne, Souvarish Sarkar, Nikhil Panicker, Gary Zenitsky, Huajun Jin, Mechelle Lewis, Xuemei Huang, Vellareddy Anantharam, Arthi Kanthasamy, and Anumantha G. Kanthasamy. Manganese promotes the aggregation and prion-like cell-to-cell exosomal transmission of α-synuclein. *Science Signaling*, 12(572), March 2019. ISSN 1945-0877, 1937-9145. doi: 10.1126/scisignal.aau4543.

[134] H. S. Pall, D. R. Blake, J. M. Gutteridge, A. C. Williams, J. Lunec, M. Hall, and A. Taylor. RAISED CEREBROSPINAL-FLUID COPPER CONCENTRATION IN PARKINSON'S DISEASE. *The Lancet*, 330(8553):238–241, August 1987. ISSN 0140-6736. doi: 10.1016/S0140-6736(87)90827-0.

[135] Nakul C. Maiti, Mihaela M. Apetri, Michael G. Zagorski, Paul R. Carey, and Vernon E. Anderson. Raman Spectroscopic Characterization of Secondary Structure in Natively Unfolded Proteins: α-Synuclein. *Journal of the American Chemical Society*, 126(8):2399–2408, March 2004. ISSN 0002-7863. doi: 10.1021/ja0356176.

[136] Nikki Kuhar, Sanchita Sil, and Siva Umapathy. Potential of Raman spectroscopic techniques to study proteins. *Spectrochimica Acta Part A: Molecular and Biomolecular Spectroscopy*, 258:119712, September 2021. ISSN 1386-1425. doi: 10.1016/j.saa.2021.119712.

[137] Dmitry Kurouski, Richard P. Van Duyne, and Igor K. Lednev. Exploring the structure and formation mechanism of amyloid fibrils by Raman spectroscopy: A review. *Analyst*, 140(15):4967–4980, July 2015. ISSN 1364-5528. doi: 10.1039/C5AN00342C.

[138] George Devitt, Kelly Howard, Amrit Mudher, and Sumeet Mahajan. Raman Spectroscopy: An Emerging Tool in Neurodegenerative Disease Research and Diagnosis. *ACS Chemical Neuroscience*, 9(3):404–420, March 2018. ISSN 1948-7193, 1948-7193. doi: 10.1021/acschemneuro.7b00413.

[139] Sara Signorelli, Salvatore Cannistraro, and Anna Rita Bizzarri. Raman Evidence of p53-DBD Disorder Decrease upon Interaction with the Anticancer Protein Azurin. *International Journal of Molecular Sciences*, 20(12):3078, January 2019. doi: 10.3390/ijms20123078.

[140] Daniel N. Bloch, Paulina Kolkowska, Isabella Tessari, Maria Camilla Barrato, Adalgisa Sinicropi, Luigi Bubacco, Stefano Mangani, Cecilia Pozzi, Daniela Valensin, and Yifat Miller. Fibrils of α-Synuclein Abolish the Affinity of Cu2+-Binding Site to His50 and Induce Hopping of Cu2+ Ions in the Termini. *Inorganic Chemistry*, 58(16):10920–10927, August 2019.

[141] Dean L. Pountney, Nicolas H. Voelcker, and Wei Ping Gai. Annular alpha-synuclein oligomers are potentially toxic agents in alpha-synucleinopathy. Hypothesis. *Neurotoxicity Research*, 7(1-2):59–67, 2005. ISSN 1029-8428. doi: 10.1007/BF03033776.

[142] Rachel Lowe, Dean L. Pountney, Poul Henning Jensen, Wei Ping Gai, and Nicolas H. Voelcker. Calcium(II) selectively induces α-synuclein annular oligomers via interaction with the C-terminal domain. *Protein Science : A Publication of the Protein Society*, 13(12):3245–3252, December 2004. ISSN 0961-8368. doi: 10.1110/ps.04879704.

Appendix A. Fabrication protocols

Fabrication protocol for extended gate-like gold electrode device

Substrate cleaning:

- Place substrate in Piranha solution (H_2SO_4:H_2O_2, 2:1, 100 ml and 50 ml) for 2 hours or overnight
- Ultrasonic bath in Aceton (5 mins); Isopropanol (5 mins); DI water (5 mins)

Resist spinning

- Dehydration bake 200°C, 5 mins
- Hexamethyldisilazane (HMDS) treatment: place substrate for 5 mins in the prepared Petri dish with previously added few drops of HMDS for ∼20 mins to create HMDS atmosphere
- Resist AZ5214E, 5000 rpm/5 s/30 s; ∼70% substrate coverage
- Soft bake 100°C, 60 s

Photolithogtraphy

- UV exposure (30 mJ/cm^2 at 405 nm)
- Post exposure bake: 120°C, 45 s
- Flood exposure: 250 mJ/cm^2

Development

- Developer MIF726, 17 s, water rinse

Gold deposition

- Deposit 5 nm Ti (adhesion layer), 50 nm Au
- Lift-off in dimethyl sulfoxide (DMSO), 80°C, 1-2 hours
- Ultrasonic bath: Aceton 5 mins, Isopropanol 5 mins, water 5 mins

PDMS

- 5 gram of PDMS (Polydimethylsiloxane) mixture per sample (SYLGARD 184 Silicone Elastomer kit, 10:1 component ratio)
- Degas for 20 mins

- Bake at least 2 h at 60°C
- Cut out PDMS from mold, punch holes

Glass-PDMS bonding

- Clean PDMS with scotch tape
- Clean glass samples and PDMS in Isopropanol, 10 mins; dry with N_2
- Put glass samples and PDMS in UVO plasma cleaner for 10 mins, with sides that will be bonded facing upwards
- Align PDMS on glass, making sure that gold electrodes are not covered with PDMS and that no air bubbles appeared between the glass sample and PDMS
- Bake on a hot plate at 80°C for 10 mins

Reference electrode

- Prepare KCL-agarose solution: 50 ml DI water, 1% agarose (0.5 g), 1M KCl (3.7 g)
- Stir and heat the solution to 80°C
- Cover gold electrode in reference well with Ag/AgCl paste
- Heat samples to 140°C, then cool down to 60°C
- Add 50 µL of KCl-agarose solution to the reference well, push through the microchannels; wait 10 mins to let it jellify
- Add more KCl-agarose solution to the reference well; wait 10 mins
- Add KCl solution (1 M) to all wells for storage, 50 µl per well

Fabrication of SU-8 mold for microfluidic channels

Substrate cleaning:

- Place beaker with substrate (4 inch Si wafer) in Aceton in ultrasonic bath (5 mins); Isopropanol (5 mins); DI water (5 mins)

Resist spinning

- Dehydration bake: 200°C, 5 mins
- Pour 2 ml of SU-8 3050 resist (drop will be ∼2 cm in diameter) for 50 µm thick layer
- Soft bake: 35°C, 15 min; 65°C, 5 min; 95°C 45 min

Photolithogtraphy

- UV exposure (200 $mJ/cm^2 \times 1.5$) with 360 nm filter (to eliminate UV radiation below 360 nm); split in 10 cycles
- Post exposure bake: 65°C, 1 min; 95°C, 4 min

Development

- Developer: MicroChem SU-8 developer, 7 min
- Rinse with IPA and dry; if white residues are observed, dip in developer for longer (∼10 s); repeat the procedure until no white residues remain
- Hard bake: 200°C, at least 5 min; better to keep for 1-2 h.

Appendix B. Molecular assembly on the surface

In addition to the data on molecular assembly characterization by Mervinetsky et al.[80], we also performed AFM and XPS measurements to verify the presence of peptides on the gold surface.

Verification of surface functionalization with AFM

To investigate how the morphology of the receptor layer on the surface changes after exposure to metal salts, we performed AFM measurements. The surface roughness is expected to decrease after the assembly[80]. We characterized surface morphology before and after the deposition of the GGH and OT peptide solutions and after the exposure of the surfaces to the $Cu(NO_3)_2$and $Zn(NO_3)_2$ salt solutions. After assembly (for a minimum of 12 hours), the substrates were rinsed with Milli-Q water and dried with N_2.

AFM measurements were performed on a gold-coated surface (50 nm), thermally evaporated on a glass substrate with titanium as an adhesion layer (5 nm). AFM scans 500 by 500 nm show clean Au surface (figure B.1a) and Au surface, functionalized with LpaGGH ligand (figure B.1b). To compare the surfaces, we used the root mean square (RMS) roughness parameter. Surface roughness is 1.05 nm for a clean gold surface and 0.67 nm for the surface, functionalized with LpaGGH ligand, respectively. After functionalization with ligand, surface roughness decreased, indicating the surface coverage.

Verification of surface functionalization with XPS

X-ray photoelectron spectroscopy (XPS) analysis was conducted at Empa (figure B.2) with Roland Hauert. The LpaGGH peptide was deposited on a gold surface in the same way as for AFM measurements. Gold electrodes, functionalized with GGH peptide, show a peak at 162 eV, which corresponds to the Au-S bond. The same result was obtained in[80].

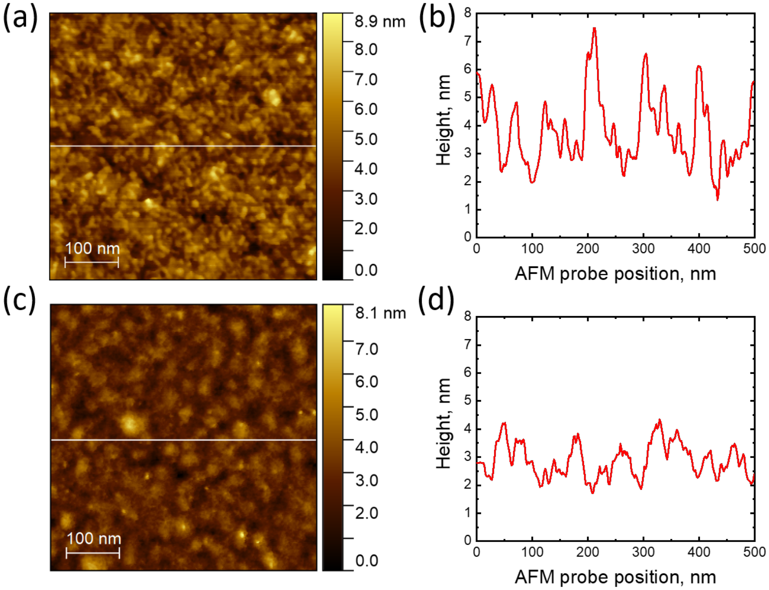

Figure B.1 Surface topography measurements: (a) clean Au surface, RMS = 1.05 nm; (b) Au surface, functionalized with LpaGGH ligand, RMS = 0.67 nm.

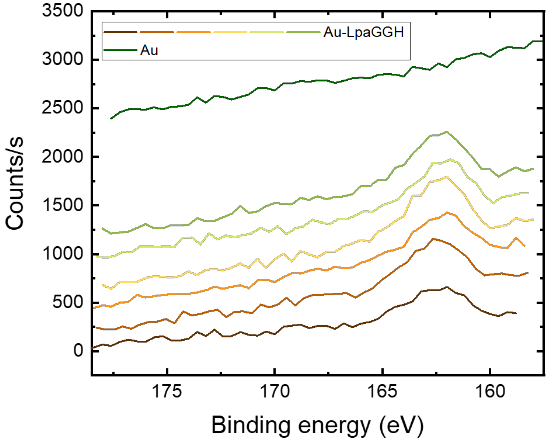

Figure B.2 XPS measurements on Au and Au-GGH surfaces.

About the Author

Olena Synhaivska, born on January 6th, 1994.

Education

08/2016 - 11/2021	**Doctor of Philosophy (PhD) in Physics** University of Basel, Switzerland *Sensing metal ions-peptide and protein interfacial interactions* Dr. Peter Nirmalraj Prof. Dr. Michel Calame
09/2014 - 06/2016	**Master of Science (MSc) in High Technologies** Institute of High Technologies National Taras Shevchenko University Kyiv, Ukraine
09/2010 - 06/2014	**Bachelor of Science (BSc) in Applied Physics** Faculty of Radiophysics, Electronics, and Computer Systems National Taras Shevchenko University Kyiv, Ukraine

Work Experience

08/2017 - 10/2021	**Research assistant** Empa - Swiss Federal Laboratories for Materials Science and Technology Transport at Nanoscale Interfaces Laboratory Duebendorf, Switzerland
03/2014 - 07/2016	**Engineer** Institute of Semiconductor Physics National Academy of Sciences of Ukraine Kyiv, Ukraine
03-06/2016 09-12/2015	**Research assistant** Institute of Complex Systems Forschungszentrum Jülich Juelich, Germany

Publications

- **Olena Synhaivska**, Shayon Bhattacharya, Silvia Campioni, Damien Thompson and Peter Niraj Nirmalraj. Single-Particle Resolution of Copper-Associated Annular α-Synuclein Oligomers Reveals Potential Therapeutic Targets of Neurodegeneration, *ACS Chem. Neurosci.* 2022, 13, 9, 1410–1421, doi:10.1021/acschemneuro.2c00021
- **Olena Synhaivska**, Yves Mermoud, Masoud Baghernejad, Israel Alshanski, Mattan Hurevich, Shlomo Yitzchaik, Mathias Wipf, Michel Calame. Detection of Cu^{2+} Ions with GGH Peptide Realized with Si-Nanoribbon ISFET. *Sensors* 2019, 19, 4022, doi:10.3390/s19184022

Talks

- *"Peptides as receptors for metal ions in potentiometric chemical sensors"*
  Single-Molecule Sensors and NanoSystems International Conference – S3IC 2020, online
- *"Differentiating complexation with GGH peptide and non-specific adsorption of copper ions on gold with Si-nanoribbon ISFET biosensors"*
  NMDC 2019, Stockholm, Sweden

Poster contributions

- *"Copper ion detection realized with Si-nanowire based ISFET sensor"*
  Swiss Nano Convention 2019, Lausanne, Switzerland
- *"Cu^{2+} sensing realized with gold-coated silicon nanowire ion-sensitive field effect transistor based biosensor"*
  Empa PhD symposium 2018 (poster prize award), Dübendorf, Switzerland
- *"Cu^{2+} sensing realized with gold-coated silicon nanowire ion-sensitive field effect transistor based biosensor"*
  Eurosensors 2018 (poster prize award), Graz, Austria
- *"Cu^{2+} detection realized with silicon nanowire ion-sensitive field effect transistor based biosensor"*
  7th Euro Biosensors & Bioelectronics Congress, 2017, Berlin, Germany

- *Cu^{2+} detection realized with silicon nanowire ion-sensitive field effect transistor based biosensor"*
  Swiss Nanoconvention 2017, Fribourg, Switzerland

Acknowledgements

First of all, I would like to express my deep gratitude to my PhD advisor, Prof. Dr. Michel Calame for giving me the opportunity to work in his group. Thank you, Michel, for your continuous support throughout this challenging but rewarding journey, and the numerous inspiring and motivating discussions. Starting from our first meeting in the Swiss Alps during the group excursion and introduction to via ferrata to the final thesis discussion with a wonderful view from Fronalpstock, conversations with you have always been a great source of inspiration.

I would like to thank Dr. Peter Nirmalraj for his immense support and for introducing me to the challenging field of neurodegenerative diseases. Thank you very much for being an excellent mentor, and for your guidance and inspiring discussions throughout my time at Empa.

Thanks to Dr. Mathias Wipf, for the supervision of my project, for always finding time to discuss and help, and for showing the way to look at the challenges from a different perspective.

I would like to thank Prof. Dr. Christian Schönenberger, for being my second supervisor, for your curiosity, and insightful conversations we had. I want to thank Prof. Dr. Jan Linnros, for being part of the examination committee, for the interesting questions, and for reviewing my thesis.

I would also like to thank the participants of the RecordIT project, in particular Prof. Shlomo Yitzchaik, Dr. Israel Alshanski, Dr. Rafael Gutierrez for the helpful discussions and support over these years.

Thanks to Prof. Damien Thompson and Dr. Shayon Bhattacharya for a great collaboration, for supporting my research with MD simulations, for the various discussions we had, and for your positive attitude, and Dr. Silvia Campioni, for providing us with alpha-synuclein and guidance on protein sample preparation. It was a pleasure to work with a such great team on this project!

I had a unique opportunity to work with many supportive and inspiring colleagues at the University of Basel and Empa, and I am grateful for it. Thanks to the entire Transport at Nanoscale Interfaces Lab, for support, the amazing working atmosphere, and also for lots of fun during the lab excursions.

In particular, I would like to thank Dr. Yves Mermoud, for the help with measurement setups and valuable insights; Dominik Bachmann, for support with electronics; Lars Lüder, for introducing me to Blender and for your help with creating images; Talia Bergaglio, for being always supportive and friendly; Dr. Jan Overbeck and Dr. Oliver Braun, for always being ready to help and advice on Raman spectroscopy; Dr. Christina Pecnik, for introducing me to nanofabrication techniques and being such great colleague; Dr. Ivan Shorubalko, for being optimistic, with original view on things and for being always ready to help; Dr. Masoud Baghernejad, Dr. Axel Fanget, Dr. Maria El Abbassi, Dr. Anton Vladyka, Dr. Kishan Thodkar - for your support from the time I joined "roomies"; Michael Stiefel, for always being around for a discussion, for being optimistic and helpful; Roman Furrer, Gökhan Kara, Jacopo Oswald - for being kind and supportive colleagues. My PhD journey would not be so enjoyable if I had not met all the great people - thanks a lot for all the fun moments we had, from playing cards in the office to traveling to the mountains for hiking and skiing!

Furthermore, I would also like to thank the great operational teams at ETH FIRST Lab and BRNC, in particular Sandro Loosli, Tobias Häusler, Dr. Diana Davila, and administrative staff at the University of Basel and Empa, Barbara Kameramann, Beatrice Spörri.

I would also like to thank Empa and the EU Horizon 2020 program for their financial support through the RecordIT project, and for providing an interdisciplinary and stimulating research environment.

I would also like to thank Jiggar, who always supported and believed in me; to my friends, and family for all their unconditional love and support throughout these years.

Olena Synhaivska
Dübendorf,
December 10th, 2021